THERMOREFLECTANCE MEASUREMENTS OF NON-DIFFUSIVE TRANSPORT IN BULK AND NANOSCALE MATERIALS

MOHAMMADREZA SHAHZADEH

A DISSERTATION SUBMITTED TO
THE FACULTY OF GRADUATE STUDIES
IN PARTIAL FULFILLMENT OF THE REQUIREMENTS
FOR THE DEGREE OF
DOCTOR OF PHILOSOPHY

GRADUATE PROGRAM IN ELECTRICAL ENGINEERING
AND COMPUTER SCIENCE
YORK UNIVERSITY
TORONTO, ONTARIO

March 2021

ABSTRACT

Following the trend in miniaturization of devices to the sub-micron scale, thermal management has become increasingly important to device operation. Thermal management becomes even more concerning in nanoscale electronic devices, where there are several interfaces for heat to pass across before reaching a bulk-like heat sink. To mitigate these issues, existing devices are constantly being re-engineered and new materials are being sought to take advantage of their improved performance. Importantly, at small scales or during fast transients, heat transport deviates from the classic diffusive regime and its physics is still being understood. To examine the thermal performance of these structures and materials at different length scales and in different heating dynamics, suitable metrology techniques are needed. In this dissertation, heat transport within bulk and nanoscale materials as well as across interfaces is studied. To achieve this goal, a frequency domain thermoreflectance (FDTR) setup is established and three different extensions to this setup are presented that improve the metrology in nanoscale materials or non-diffusive transport. Having different variations of the FDTR setup enables us to selectively utilize these techniques depending on the sample structure and the questions one is investigating. By measuring different structures, we show that our setups are capable of examining thermophysical properties of different materials ranging from two dimensional to three dimensional materials, from dielectrics to metals, and from thermally isotropic to anisotropic.

We, then, turn our attention to non-diffusive heat transport in two different structures: metallic Platinum-Cobalt multilayers, and Tungsten disulfide (WS_2) crystal. In the case of metallic Platinum-Cobalt multilayers, we show that as the interface density increases and the layer thickness becomes comparable with the electron mean free path in these metals, a deviation from the diffusive theories governing heat transport in electron-mediated multilayers is observed for the

first time. Finally, we show that strong non-diffusive heat transport in WS_2 can be observed at room temperature as a function of heat spot size. This not only highlights unique transport features in this material, but also points to the susceptibility to misinterpret experimental data if non-diffusive transport is not considered.

DEDICATION

To my parents…

ACKNOWLEDGEMENTS

First of all, I would like to express my deepest appreciation to my supervisor, Professor Simone Pisana, who guided and supported me every step of this long way. When I joined The HEATD Lab as his first graduate student, he tirelessly helped me set up the FDTR setup. He was always available for discussions and for helping me in the lab, and whenever I needed any help, I knew I could count on him as my supervisor and my friend. I truly feel proud and privileged to be his student. Simone, you are my role model.

I am thankful for the assistance of my supervisory committee members, Professor Sebastian Magierowski and Professor Sunny Leung, as well as my defense committee members, Professor Gerd Grau, Professor Regina Lee, and Professor Alexandre Champagne, for their time and effort reviewing this dissertation and for their valuable comments.

I would like to thank members of The HEATED Lab Shany Mary Oommen and Olga Andriyevska for their friendship. I want to thank Olga for fabricating samples. I owe special thanks to Mizanur Rahman from The HEATED Lab for his valuable scientific contributions and assistance. I am thankful to members of Professor Olav Hellwig's group and Professor Stephen Hofmann's group for providing us with interesting samples.

I want to thank all my previous teachers and mentors for helping me reach where I am today. I am thankful to my friends especially Azi who helped me during difficult times.

Finally, I am forever thankful to my parents for their unconditional love and support. I simply would not be where I am today if it wasn't for their sacrifices. My brother, Mohammad, my sister, Mahshid, my sister-in-law, Azadeh, and my nephew, Mehrad, I love you and I am grateful for having you in my life.

TABLE OF CONTENTS

LIST OF FIGURES

LIST OF SYMBOLS AND ABBREVIATIONS

S: Seebeck coefficient

σ: Electrical conductivity

k: Thermal conductivity

k_e: Electronic thermal conductivity

k_p: Lattice thermal conductivity

k_r: In-plane thermal conductivity

k_z: Out-of-plane thermal conductivity

k_{accum}: Thermal conductivity accumulation function

e: Electron charge

Λ: Mean free path

R: Thermal resistance

g: Electron-phonon coupling coefficient

q: Heat flux

T: Temperature

C: Volumetric heat capacity

v: Velocity

k_B: Boltzmann's constant

L_0 : Lorentz number

L_c : Characteristic length scale

L_P: Thermal penetration depth

D: Thermal diffusivity

D_z: Out-of-plane diffusivity

G: Thermal boundary conductance

TBC: Thermal boundary conductance

f: Frequency

ω: Angular frequency

ζ: statistical factor

α: Transmission probability

Z: Impedance

ρ: Mass density

v_{fermi}: Fermi velocity

γ: Sommerfeld parameter

β: Coefficient of thermoreflectance

$\Re$: Reflectivity

λ: Wavelength

I: Intensity

A_0: Beam power

ω_0: $1/e^2$ pump beam radius

ω_1: $1/e^2$ probe beam radius

h: Hankel transform variable

$P(h)$: Hankel transform of the intensity profile of pump beam

$S(h)$: Hankel transform of the intensity profile of probe beam

$G(f,h)$: Hankel transform of the Green's function solution

t: Thickness

A_P: Absorbed intensity of pump laser

A_S: Absorbed intensity of probe laser

θ_{Thermal}: Thermal phase

θ_{Ref}: Reference phase

MFP: Mean free path

DOS: Density of states

AMM: Acoustic mismatch model

DMM: Diffuse mismatch model

EDMM: Electronic diffuse mismatch model

MTL: Maximum transmission limit

vdW: van der Waals

ML: Multilayer

HT: Heterostructure

CPP: Current-perpendicular-to-plane

FDTR: Frequency domain thermoreflectance

TDTR: Time domain thermoreflectance

BB-FDTR: Broad band frequency domain thermoreflectance

MOKE: Magneto-optical Kerr effect

FD-MOKE: Frequency domain magneto-optical Kerr effect

SNR: Signal to noise ratio

DTP: Differential thermal phase

EOM: Electro-optic modulator

PBS: Polarizing beam splitter

BS: Non-polarizing beam splitter

No subject has more extensive relations with the progress of industry and the natural sciences; for the action of heat is always present, it penetrates all bodies and spaces, it influences the processes of the arts, and occurs in all the phenomena of the universe. – Joseph Fourier, 1822 [1].

Chapter 1: Introduction

1.1 Motivation

With the rise of nanotechnology and device sizes shrinking [2], studying heat transport in nano-structures became a must. By the early 1970s, the size dependence of thermal conductivity was observed in different materials [3-7]. A size dependent thermal conductivity has both undesirable and favorable consequences. For instance, a low thermal conductivity is useful for thermo-electric materials where their performance expressed by the figure of merit $S^2\sigma/k$ (where S is the Seebeck coefficient, σ is electrical conductivity and k is thermal conductivity) is inversely proportional to thermal conductivity [8]. On the other hand, high thermal conductivity is useful when heat needs to be dissipated as effectively as possible. This is, for instance, the case for semiconductor lasers whose output is sensitive to their operating temperature [8]. Another example that illustrates the desire for high thermal conductivity materials is in integrated circuits (ICs), whose power densities and speed have been increasing [8]. Moore, co-founder of Intel, observed in the 1960s that the number of transistors per unit of area in an IC had been and will be doubling approximately every two years. This trend not only affected the number of transistors, but also the performance of the electronic chips as well. However, as the device size decreased and the number of transistors per unit area increased, heat management became more and more challenging [9]. At the moment, the

length scale of electronic devices is approaching 10 nm and below. Furthermore, as a consequence of dissipated powers reaching levels of ~ 100 W/cm^2 [10], the increasing trend of CPU clock frequency has stopped [9] and designs have instead favored multiple parallel core architectures instead.

Thermal conductivity, in the classical description of kinetic theory, arises from scattering events between heat carriers or with boundaries [11]. In this "diffusive" description of heat conduction, the size of the system is far greater than the average distance between the collision events of the energy carriers (i.e. the mean free path, MFP or Λ) and thus, the heat carriers undergo many scattering events before reaching the physical boundary of the system. By reducing the size of the system until it becomes comparable with the MFP of the heat carriers, the heat transfer is not fully diffusive anymore and ballistic transport takes place.

The physical size of a material, however, is not the only relevant length scale to affect the thermal conductivity. Different characteristic length scales can be compared with the MFP of the heat carriers to study the transition of diffusive to ballistic heat transport. Besides the physical dimensions of the system [12], the heater size [13] and the penetration depth of the thermal waves in the material [14] are other examples of these characteristic length scales. Studying the contribution of heat carriers with different MFP to the bulk thermal conductivity and constructing the so-called thermal conductivity accumulation function provides valuable information to optimally engineer materials for different applications.

Besides the thermal conductivity of individual materials, another quantity often contributes to the effective thermal conduction in a system of materials. This is especially the case in layered materials where there are several interfaces between the heat source and heat sink. Here, the thermal resistance at the interfaces becomes important. In the simplest case, assume a system

consists of two materials, A and B, with an interface (Figure 1-1a). The total thermal resistance of the system can be expressed as $R_{total} = R_A + R_B + R_{Interface}$. However, as the number of interfaces increase (assuming R_A and R_B remain the same), the relative contribution from the resistance at the interfaces increase, Figure 1-1c. As will be discussed later in this dissertation, the contribution of the resistance at the interfaces (or its inverse, the thermal boundary conductance, TBC) depends on several factors such as materials forming the interface and interfacial properties [15]. It should be noted that adding resistances linearly (as depicted in Figure 1-1c) is only possible for diffusive transport. As the layer size becomes comparable to the MFP, the trend of increasing resistance with the number of interfaces may become nonlinear.

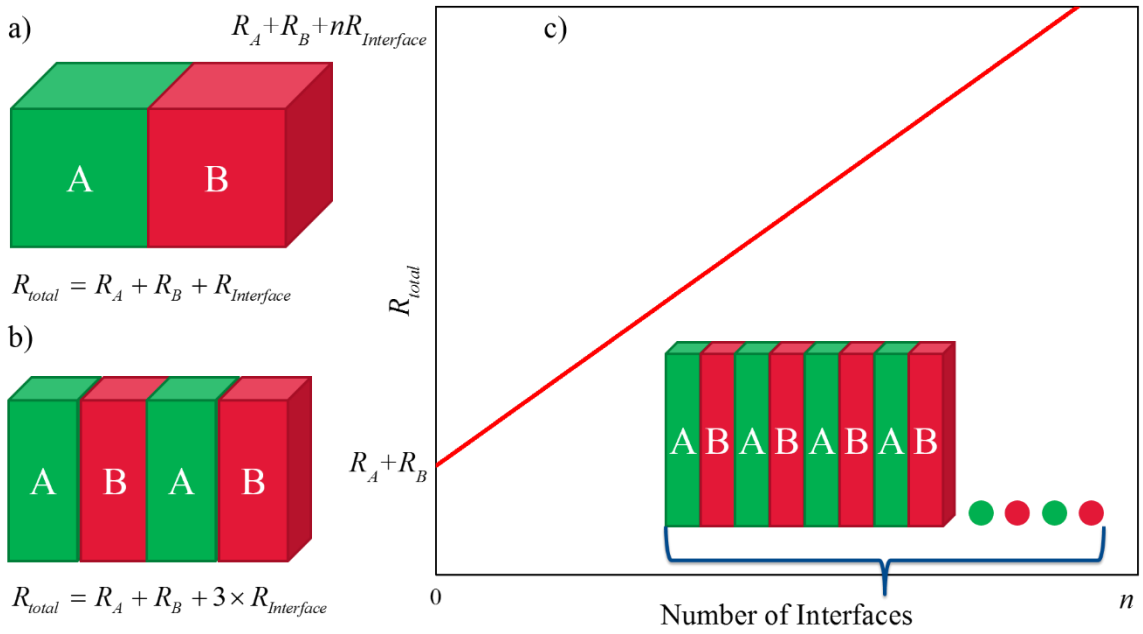

Figure 1-1. The thermal resistance of a system consisting materials A and B with (a) one interface and (b) three interfaces. (c) The thermal resistance as a function of number of interfaces. As the number of interfaces increases, the contribution from interfacial resistance to the thermal resistance increases.

To gain insight into the physics of energy transport, appropriate metrology systems are needed. The performance of optical pump and probe metrology systems has improved significantly in the last two decades. These systems have provided the opportunity to study thermal properties of different bulk and nano-scale systems and enriched our fundamental understanding of heat transport mechanisms. The development of techniques such as frequency domain thermoreflectance (FDTR) and time domain thermoreflectance (TDTR) has helped formulate a more complete picture of heat transport. These techniques allow for measurements of thermal conductivity, MFP spectroscopy, and thermal boundary conductance for different materials. Improving the optical pump and probe metrology systems allows studying these structures as well as newly discovered materials such as two-dimensional graphene, to eventually improve and engineer their performance toward commercialization. Furthermore, by increasing the sensitivity of these characterization techniques to anisotropic heat transport, the thermal conductivity of highly anisotropic materials can be investigated.

1.2 Outline of this dissertation and contribution to the literature

The purpose of this dissertation is to develop and improve thermal characterization techniques based on the principle of thermoreflectance: the change in optical reflectivity as a function of temperature. These techniques are then used to investigate thermal properties of a variety of systems of materials to investigate non-diffusive transport phenomena. The outline of this dissertation is as follows:

- A short motivation is provided in chapter 1.
- In chapter 2, the basic principles of heat conduction in solids and across interfaces are reviewed. This lays the foundation of heat conduction physics used throughout this

dissertation, and outlines the effects that take place when non-ballistic transport ensues. This chapter also describes the basic principles of thermoreflectance methods, how quantitative data is obtained from these measurements and ancillary characterization techniques.

- The specific implementations of FDTR, beam offset FDTR, frequency domain magneto-optical Kerr effect (FD-MOKE), and differential broadband FDTR (DBB-FDTR) are presented in chapter 3. These are the experimental characterization techniques that have been implemented or developed for this work. These methods are then used to measure thermophysical properties of a different range of materials.

  In chapter 3, a typical implementation of FDTR setup is introduced and methods to extend the frequency range of the measurement will be discussed. By introducing beam offset FDTR and FD-MOKE, sensitivity to anisotropic thermal conductivity will be increased which allows for measuring a wide range of thermally anisotropic materials. The techniques are then used to measure thermal conductivity of different samples such as graphite and Graphene. Then, by introducing DBB-FDTR concept, we provide an alternative implementation of the broad-band FDTR setup introduced by Regner *et al* [16].

- Anisotropic heat transport in Pt/Co multilayers is investigated in chapter 4. The fundamental question investigated in this chapter is the physics of electronic heat transport across metallic multilayers when the layer thickness is comparable with the electron MFP.

  It will be shown that by increasing the interface density of Pt/Co interfaces and decreasing the multilayer period thickness below the MFP of electrons in Pt and Co, a deviation from the predictions of the diffusive theories governing heat transport across metallic interfaces is observed. We attribute this deviation to the non-diffusive nature of heat transport when

thickness of the layers is well below MFP of electrons. The observation of non-diffusive transport across metallic multilayers and deviation of the thermal boundary conductance across metallic interfaces from non-diffusive theories has not been reported in the literature before, to the best of our knowledge. The results presented here are useful in describing heat transport in metallic high interface density structures such as in magnetic memory devices and in spintronic applications.

- Chapter 5 will be dedicated to the observation of strong non-diffusive heat transport in Tungsten disulfide. The findings of this chapter provide an insight into non-diffusive heat transport at micrometer scale and at room temperature; a condition that is often neglected.

  Here, we experimentally demonstrate reductions ~60% and ~35% in in-plane and out-of-plane components of thermal conductivity of bulk Tungsten disulfide, when heater size is reduced from ~14 to ~1.5 μm. This reduction of thermal conductivity is then attributed to non-diffusive transport in Tungsten disulfide. The results of this work show the importance of correctly interpreting thermal conductivity measurements when heater size is small.

- The dissertation closes with a conclusion in chapter 6.

1.3 Statement of author contributions

The author implemented typical FDTR and DBB-FDTR concepts and contributed in implementing beam offset FDTR and FD-MOKE setups [1]. The author performed measurements and post-measurement analysis on samples presented in chapter 3. FD-MOKE measurement performed on

[1] Some parts of this dissertation was performed in collaboration with Mizanur Rahman, who was a master's student in the HEATED lab.

Graphene in chapter 3 was performed by Mizanur Rahman. The metallic multilayers samples presented in chapter 4 were fabricated by Olga Andriyevska. Deposition of the WS_2 substrate presented in chapter 5 was performed by Mizanur Rahman, and the measurements and post-measurement analyses were performed by the author and Mizanur Rahman.

Chapter 2: Theory of Heat Transport and Characterization Techniques

Chapter 2 has been partially adapted, with permission, from:

M. Shahzadeh, M. Rahman, O. Hellwig, and S. Pisana, "High-frequency measurements of thermophysical properties of thin films using a modified broad-band frequency domain thermoreflectance approach," *Review of Scientific Instruments*, vol. 89, no. 8, p. 084905, 2018. Copyright 2018 American Institute of Physics.

2.1 Heat Conduction in Solids

When metals absorb photons (for instance from a laser source), the energy from the photons is transferred to its electrons. Considering the MFP for electrons in common metals (~ 50 to 100 nm), and traversing with velocities near Fermi velocity ($\sim 10^6\ m/s$), electrons can travel 100 nm in 100 fs. Their energies reach an equilibrium Fermi-Dirac distribution due to electron-electron scattering in less than a picosecond [17]. The hot electrons then interact with the cold phonons of the crystal and exchange heat. The parameter which describes how effectively electrons and phonons exchange energy is called the electron-phonon coupling coefficient. The smallest electron-phonon coupling coefficient in metals belongs to Gold with $g_{Au} = 2.2\times10^{16}$ W/m^{3}K [18]. In comparison, the electron-phonon coupling coefficients of Aluminum and Tantalum are $g_{Al} = 2.45\times10^{17}$ W/m^{3}K and $g_{Ta} = 3.1\times10^{18}$ W/m^{3}K, respectively [18, 19]. The difference between electron-phonon coupling coefficient of Al and Au indicates that the electrons and phonons in Al reach a

thermal equilibrium more quickly compared to Au [18]. It has been shown that, using simplified arguments, electrons and phonons in metals will thermalize within 100 ps [17].

In a layered structure, the heat carriers of the top layer can travel across an interface and (depending on the materials) interact with the electrons or phonons of the layer underneath. For instance, in a metal/nonmetal system, energy transfer from the hot electrons in the top layer to the heat carriers (phonons) of the bottom layer can take place through two main channels: 1) interactions between the electrons and the phonons of the metal mediated by the electron-phonon coupling and subsequent phonon transport across the interface, and 2) the direct interfacial interaction between the electrons of the metal and the phonons of the nonmetal [20].

2.1.1 Fourier's Law of Heat Conduction

Heat transport is usually expressed by the Fourier's law of heat conduction. Based on Fourier's law, the heat flux (q) is proportional to the local temperature gradient (∇T) with a proportionality constant of k, (in units of W/mK), where k is the coefficient of thermal conductivity:

$$q = -k\nabla T \tag{2.1}$$

In most solids, thermal conductivity (k) is comprised of two main portions: $k = k_e + k_P$, where k_e and k_P are the contributions of electrons and phonons to the thermal conductivity, respectively [21]. Simple kinetic theory describes thermal conductivity as $k = \frac{1}{3}Cv\Lambda$ in which C is the volumetric heat capacity, v is the group velocity and Λ is MFP of the heat carrier [22]. The volumetric heat capacity of electrons is smaller than phonons. However, the Fermi velocity of

electrons $\left(\sim 10^6\ m/s\right)$ is much larger than the group velocity of phonons $\left(\sim 10^3\ m/s\right)$ [23]. Therefore, in metals the product of *Cv* is much larger for electrons than phonons. As a result, electrons are the major heat conduction carriers in metals $\left(k_e \gg k_P\right)$, while phonons have a more pronounced impact in non-metals $\left(k_e \ll k_P\right)$ [20]. A typical method to measure the electronic portion of the thermal conductivity of materials $\left(k_e\right)$ is by using the four-point probe measurement. In the four-point probe technique (which will be described later), the electrical conductivity $\left(\sigma\right)$ of the material is measured and then it is converted into its electronic thermal conductivity $\left(k_e\right)$ using the Wiedemann-Franz law.

2.1.2 Wiedemann-Franz Law

As electrons are the major electrical and heat carriers in metals, one might expect to see a relation between electrical conductivity and thermal conductivity. The Wiedemann-Franz law relates the electrical conductivity of a metal to its thermal conductivity at a given temperature [24]:

$$L_0 = \frac{k_e}{\sigma T} = \frac{\pi^2 k_B^2}{3e^2} \tag{2.2}$$

Where $L_0 = 2.4453 \times 10^{-8}\ \mathrm{W\Omega/K^2}$ is the Sommerfeld value of the Lorentz number (the Lorentz number changes among metals with non-spherical Fermi surfaces and is also affected by disorder), k_e is the electronic thermal conductivity, T is the absolute temperature, σ is the electrical conductivity, e is the electron charge and k_B is Boltzmann's constant. According to Eq. (2.2) the ratio of electronic thermal conductivity to electrical conductivity at a given absolute temperature

is constant. The Sommerfeld value of the Lorentz number can be used reliably in the Wiedemann-Franz law at low- and high- temperatures as long as the metal is not very pure and defect-free [24], since disorder tends to collapse the large variations of Lorentz numbers in pure elemental metals to a universal value. It also provides an opportunity to have a fairly acceptable estimate of the electronic thermal conductivity of metals from their electrical conductivity, which can readily be measured.

As mentioned above, Wiedemann-Franz law combined with the four-point probe technique measures the electronic thermal conductivity. However, the classic bench-top tools used for measuring phonon thermal conductivity are not appropriate for thin-films and nanostructures, unlike Wiedemann-Franz law which typically can be used at different size scales [25]. An example of methods to measure phonon thermal conductivity of bulk materials is the so-called absolute technique, in which the sample of interest is placed between a heat source and a heat sink and the temperature drop in a given the length of the sample is recorded [26]. Another method to measure the phonon thermal conductivity of bulk materials is the laser flash method, in which an optical source heats the front of a sample while a detector measures the temperature transient on the back of the sample [26].

2.1.3 From Diffusive to Ballistic Heat Conduction

Here, let us consider a simple case where the thermal conductivity of a material is studied as a function of physical size of the sample. When studying heat carriers (e.g. electrons and phonons) propagating across a bulk material, it is assumed that the energy distribution in any part of the sample is very close to the thermal equilibrium condition in the whole sample (a local thermal

equilibrium condition) [27]. In this case, the physical size of the sample is an important characteristic length scale (L_c) to compare with the MFP of the heat carriers and the relation $\Lambda << L_c$ holds. The thermal equilibrium condition is satisfied in a bulk system, as there are enough scattering events for the heat carriers to equilibrate [21] within the typical size of macroscopic samples, i.e. $\Lambda << 1$ mm.

Heat transfer in this case is called *diffusive*, which can be described by Fourier's law of heat conduction and the heat diffusion equation. The Fourier's law of heat transfer is based on a macroscopic average behavior of the heat carriers undergoing many scattering events. Thus, as the scattering events are studied in an appropriately large sample and over a long period of time, the MFPs of the heat carriers is correlated to the intrinsic properties of the materials [28].

However, as the size of the sample shrinks down, the MFPs of the heat carriers become comparable or larger than the sample size ($\Lambda > L_c$) and consequently the heat carriers can travel in the volume of the sample without reaching equilibrium or by scattering only at the boundaries of the sample [27, 28]. In this case, since there are few or no scattering events between the sample boundaries, no thermodynamic equilibrium exists within the volume of interest and the Fourier's law of heat conduction (Eq.(2.1)) is not valid anymore. Note that here we have assumed for simplicity that boundary scattering is elastic and does not contribute to reaching a thermodynamic equilibrium. Heat condition in this condition is called *ballistic* (or more generally, *non-diffusive*). The thermal conductivity measured in this case might not be the same as the bulk value.

In general, in order to determine if heat transfer is diffusive or not, the MFP of the heat carriers is compared with L_c . In the example above, the MFP of heat carriers was compared to the sample's physical size. However, there are other important dimensional parameters, beside sample's size,

that can be compared with the MFP of heat carriers. Here, some of important characteristic length scales will be mentioned.

An important example of the experimental characteristic length scale mentioned above (L_c), is the distance that thermal waves such as those created by modulating the heat flux travel into the sample. For a semi-infinite isotropic medium, the thermal penetration depth (L_P) is a measure of the depth at which the temperature amplitude is e^{-1} of the surface temperature [29]. The thermal penetration depth for a heat source with intensity modulation frequency of f is $L_P = \sqrt{D/(\pi f)}$, where D is the thermal diffusivity, defined as the ratio of thermal conductivity to volumetric heat capacity, $D = k/C$ [30].

Another example of the characteristic length scale is the heater size [13]. When the heater size is larger than the MFPs of phonons, the hot phonons undergo enough scattering events to thermalize and reach a local equilibrium (diffusive regime). However when the heater size is smaller than the MFPs of phonons, a smaller number of scattering opportunities are available to phonons to reach a local thermal equilibrium, and phonons can travel non-diffusively over distances comparable to the heater size [13]. This results in the departure from the assumption of a local thermal equilibrium, and the Fourier law does not apply. This concept has been depicted in Figure 2-1.

It should be noted that heat transport can alternatively be described by the relationship between mean free time and the characteristic time scales, instead of comparing mean free path and characteristic length scales [31]. In the alternative picture, heating events much faster than the phonon relaxation times cannot be cooled diffusively.

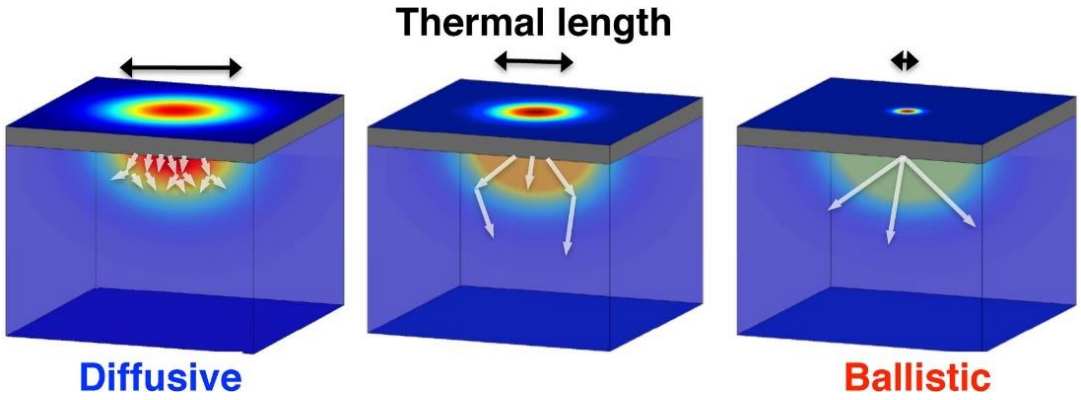

Figure 2-1. From diffusive to ballistic heat transport with decreasing heater size (from left to right) [32]. The white arrows represent phonons travelling ballistically, with changes of directions indicating a scattering event. Reprinted with permission from J. Phys.: Condens. Matter, 27, 053202 (2015). Copyright 2015 Institute of Physics.

2.1.4 Thermal Conductivity Accumulation Function

Phonons of a material do not have all the same MFP. Instead, a MFP spectrum exist. As it was mentioned earlier, phonons with MFP larger than L_c are considered to travel non-diffusively through the volume of interest, while those with MFPs smaller than L_c travel diffusively [33]. Based on observing this non-diffusive behavior of phonons, Koh and Cahill hypothesized that phonons with MFPs greater than the thermal penetration depth (as L_c) do not contribute to the thermal conductivity, as they escape the volume that was samples by their measurement [33]. As a result, not all of the phonons contribute to the effective thermal conductivity. This idea has opened an avenue to probe the distribution of the phonon MFPs by varying L_c systematically.

The L_c-dependent behavior of thermal conductivity has been correlated with the so-called thermal conductivity accumulation function $\left(k_{accum}\right)$. The thermal conductivity accumulation function describes how different energy carriers with different MFPs contribute cumulatively to the thermal

conductivity [16]. The thermal conductivity accumulation function can be described as follows [14]:

$$k_{accum}\left(\Lambda^{*}\right)=\sum_{Polarization}\int_{0}^{\Lambda^{*}}\frac{1}{3}C\left(\Lambda\right)v\left(\Lambda\right)\Lambda d\Lambda \tag{2.3}$$

where C is the volumetric heat capacity, v is the phonon group velocity and Λ is the MFP of phonons. Each quantity in the integral may be phonon polarization dependent (i.e. transverse and longitudinal modes), and all contributions are summed together. The thermal conductivity expressed in Eq. (2.3) is due to phonons with MFPs less than Λ^{*} [14]. By reducing Λ^{*} to nano-scale, k_{accum} described by Eq. (2.3) tends to zero (depending on the material). On the other hand, by increasing Λ^{*}, the thermal conductivity accumulation function tends to the bulk thermal conductivity of the material. Studies on Si have shown that a wide phonon spectrum contribute to the thermal conductivity, with some phonon MFPs well above 10 um. This is very different from the estimated average (so-called grey approximation) MFP of $\bar{\Lambda}\approx 40\,nm$ obtained from the kinetic theory ($k=\frac{1}{3}Cv\bar{\Lambda}$) [13, 14].

In order to study the thermal conductivity accumulation function experimentally, a systematic variation of L_c is performed [2]. As an example, the modulation frequency of the heat flux impinging on the sample can be varied. By changing the modulation frequency and consequently changing the thermal penetration depth $\left(L_P=\sqrt{D/\left(\pi f\right)}\right)$, the contribution of phonons with different MFPs to the thermal conductivity of the material can be revealed (Eq. (2.3)). The heater

[2] It should be noted that a direct correlation between L_c and MFP-dependent thermal conductivity is not always straightforward. In order to relate L_c to a MFP-dependent thermal conductivity, a suppression function is used.

size is another example of L_c to study the thermal conductivity accumulation function. This can be done by systematically changing the laser spot size, or by pattering heater arrays of different size. Studying the thermal conductivity accumulation function reveals the contribution of different heat carriers to thermal conductivity and allows for engineer and control thermal conductivity of different systems. For instance, this is desirable in thermo-electric materials in which the efficiency is inversely proportional to the thermal conductivity [34].

2.1.5 Thermal Conductivity of Different Materials

As mentioned earlier, electrons and phonons are the major heat carriers in most solids [3]. However, their relative contributions to thermal conductivity depends on the type of material. While free electrons are the major carriers in metals, phonons dominate heat conduction in dielectrics and light-to-moderately doped semiconductor crystals [25]. As an example, the contribution of phonons to thermal conductivity of pure copper is less than 5% [35, 36]. The thermal conductivity in semi-metals and heavily-doped semiconductors have considerable contributions from both electrons and phonons [25]. Contributions of electron and phonons to thermal conductivity of a several metals has been depicted in Figure 2-2.

[3] An example where electron and phonons are not the only energy carriers is magnetic materials, where magnons (collective spin excitations) also play a role.

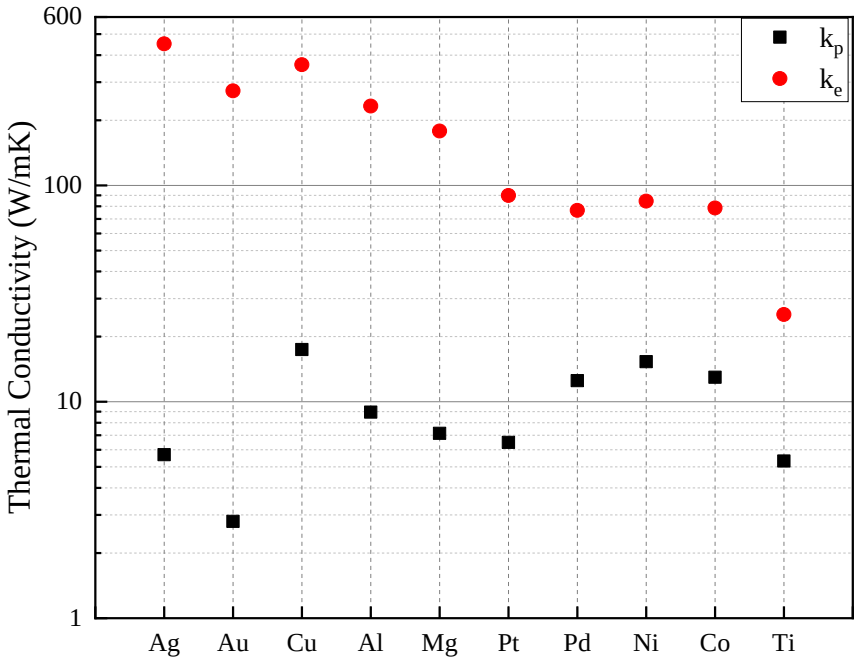

Figure 2-2. Electronic (k_e) and phononic (k_p) thermal conductivity for several metals from first-principles calculations. Data from Ref. [35].

Figure 2-3 compares thermal conductivity for a few solids, spanning metals, dielectrics, crystals and amorphous materials. In thermally isotropic solids, thermal conductivity typically ranges between ~1 W/mK (such as in amorphous materials) and ~2000 W/mK (such as in diamond) [21, 30]. On the other hand, thermally anisotropic materials span an even wider range of thermal conductivity [37], such as graphite with in-plane thermal conductivities of ~2000 W/mK [38, 39].

In general, materials with lower atomic mass, stronger interatomic bonds, simpler crystal structures and lower lattice anharmonicity exhibit higher thermal conductivity [40]. Other parameters that can affect the thermal conductivity include doping, impurities, defects, and finite size effects. For

instance, in-plane a thermal conductivity smaller than 25 W/mK was reported for 20 nm thick Si layers with bulk thermal conductivity of 148 W/mK [41].

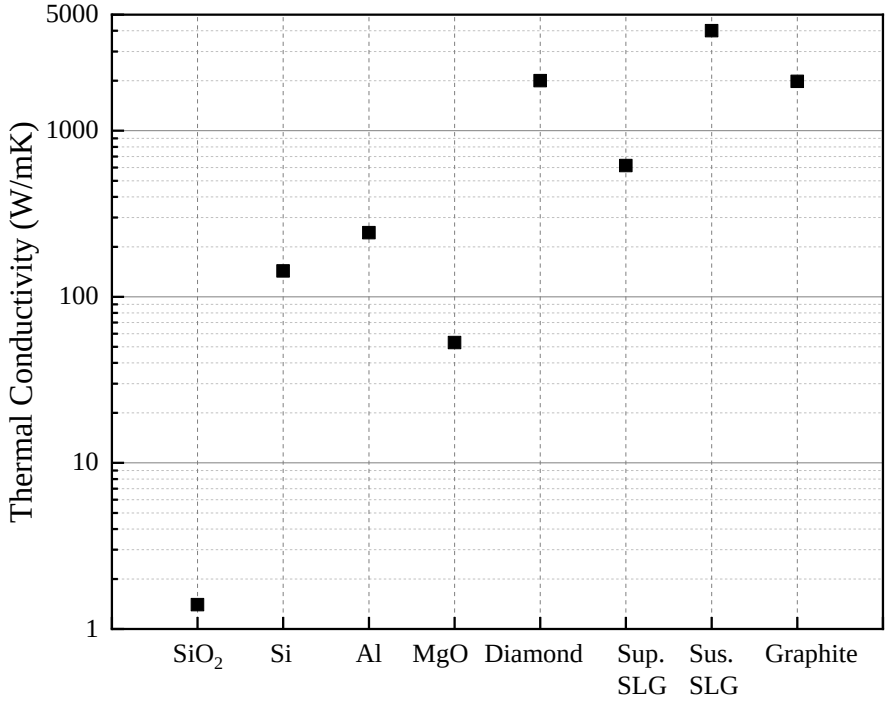

Figure 2-3. Thermal conductivity of different materials. Sup. SLG and Sus. SLG represent supported and suspended single layer graphene, respectively. The values for SLG and Graphite are the in-plane thermal conductivities. Data taken from Ref. [14, 39, 42-44].

2.2 Thermal Boundary Conductance: Heat Conduction across Interfaces

When heat carriers travel across two different materials, they experience a resistance at their interface. Depending on the materials being metallic or non-metallic, electrons, phonons or both can contribute to the thermal boundary resistance (its inverse is called thermal boundary conductance). The first observations of thermal resistance at an interface were made in 1941 by

Kapitza who found a temperature drop between superfluid helium and copper at their interface under constant heat flux [45]. Later, it was realized that this temperature drop exists at the interface of any two dissimilar materials [46]. The thermal boundary conductance is mainly determined by the materials forming the interface, but interfacial characteristics such as roughness, bonding and intermixing of the materials can significantly affect it [47]. This resistance forms a temperature discontinuity at the interface, as depicted in Figure 2-4.

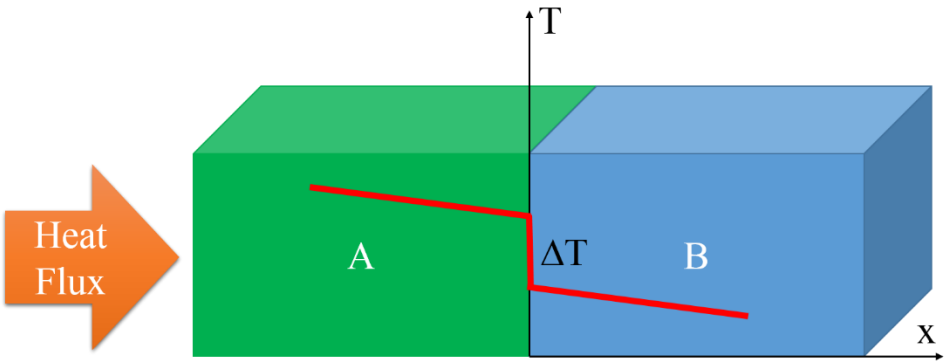

Figure 2-4. Illustration of the thermal boundary conductance.

Thermal boundary conductance (G) is described as the proportionality constant linking the net heat flux to the temperature drop across the interface, and describes how strongly an interface conducts heat [15]:

$$G = \frac{q_{net}}{\Delta T} = \frac{q_{12} - q_{21}}{T_1 - T_2} \tag{2.4}$$

where q_{ij} represents the heat flux from the side i to the side j. Analytically, q_{ij} can be described as [48]:

$$q_{ij} = \sum_{p} \int_{\phi=0}^{2\pi} \int_{\theta=0}^{\pi/2} \int_{\omega=0}^{\omega_{i,\max}} \eta_i \zeta_i \alpha_{ij} \sin\theta d\theta d\phi d\omega \tag{2.5}$$

with ω being the phonon frequency, p the phonon polarization, (θ, ϕ) the directional angles of incident phonons (Figure 2-5), and ζ the Bose-Einstein (or Fermi-Dirac) statistical factor for phonons (or electrons) [48]. α_{ij} is the transmittance probability and $\eta_i = \frac{1}{4\pi} \hbar \omega v_i DOS_i \cos\theta$, where $v_i(\omega, p)$ is the group velocity and $DOS_i(\omega, p)$ is the density of states [48]. Therefore, for isotropic materials:

$$q_{12} = \sum_{p} \frac{1}{4\pi} \int_0^{2\pi} d\phi \int_0^{\pi/2} \sin\theta \cos\theta d\theta \int_0^{\omega_{1,\max}} v_1 \hbar \omega DOS_1(\omega, p) \zeta_1(\omega, T_1) \alpha_{12} d\omega \tag{2.6}$$

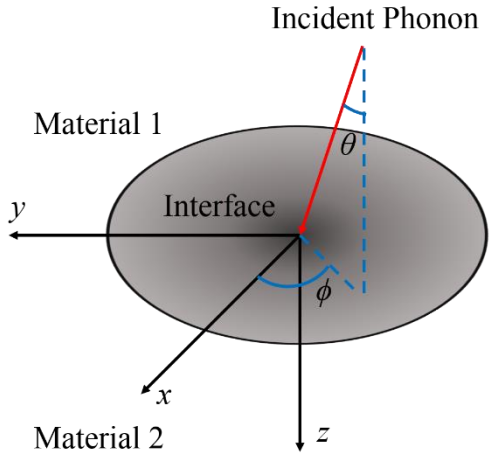

Figure 2-5. Definition of phonon direction when scattering at an interface. Adapted from Ref. [49].

Assuming the phonon reflectivity from one side equals the phonon transmissivity from the other side [49]:

$$1 - \alpha_{12} = \alpha_{21} \tag{2.7}$$

With attention to the principle of detailed balance, which implies that in thermal equilibrium the number of phonons with frequency ω travelling from the side i to the side j is equals the number of phonons with the same conditions travelling from the side j to the side i per unit area per unit time [50]:

$$q_{net} = \sum_p \frac{1}{4\pi} \int_0^{2\pi} d\phi \int_0^{\pi/2} \sin\theta \cos\theta d\theta \times \int_0^{\omega_{1,\max}} v_1 \hbar \omega DOS_1(\omega, p) \left[\zeta_1(\omega, T_1) - \zeta_2(\omega, T_2) \right] \alpha_{12} d\omega \tag{2.8}$$

Eventually, by introducing $C = \hbar \omega DOS(\omega, p) \frac{d\zeta(\omega, T)}{dT}$ as the mode-dependent specific heat and substituting $\mu = \cos\theta$, for small temperature differences due to the principle of detailed balance, the thermal boundary conductance can be written as [49]:

$$G = \sum_p \frac{1}{2} \int_0^1 \int_0^{\omega_{1,\max}} v_1 C_1 \alpha_{12} \mu d\omega d\mu \tag{2.9}$$

According to Eq. (2.9), the thermal boundary conductance depends on the dispersion, the temperature, and the transmission probability (α_{12}). The transmission probability is the quantity that is most difficult to calculate. In this regard, models such as acoustic mismatch model (AMM) and diffuse mismatch model (DMM) have been presented. Although they both are described by Eq. (2.9), they differ in the assumptions used to calculate the transmission probability, and they are applicable in different situations.

2.2.1 Acoustic Mismatch Model (AMM)

The first model developed to explain the temperature drop at interfaces was the acoustic mismatch model (AMM), proposed by Khalatnikov in 1952 [51]. Khalatnikov based his model on a continuum acoustic approach where phonons were represented by acoustic plane waves in a semi-infinite medium [50]. Based on this approach, it was considered that the acoustic waves (i.e. phonons) reflect specularly and no (diffusive) scattering happens at the interface at low temperatures [49]. This is appropriate as at low temperatures the phonon population is comprised of low-energy and long wavelength excitations, and therefore the assumption of plane waves is valid even at relatively rough interfaces. As the reflection of these acoustic waves disrupt the heat flow across the interface, a resistance against heat flow is generated [52].

In order to calculate the angle of reflection/transmission of these acoustic waves as well as their transmission coefficients, acoustic analogs of Snell's law and Fresnel equations for electromagnetic waves are used [50]. In these analogs, the acoustic impedance defined as $Z = \rho v$, with ρ as the mass density and v as the phonon velocity, plays a similar role to the optical refractive index for electromagnetic waves [49, 52]. Therefore, for an incident phonon wave vector with the polarization of p and with incident angle $\theta_{p,1}$ and refracted angle $\theta_{p,2}$:

$$\frac{\sin\theta_{p,1}}{\sin\theta_{p,2}} = \frac{v_{p,1}}{v_{p,2}} \tag{2.10}$$

In a similar way to optics, if the phonon incident angle is too large, the phonons can undergo total internal reflection. For a simple case of phonon waves normal to the interface, the transmission probability α_{12} is calculated as [46]:

$$\alpha_{12} = \frac{4Z_{p,1}Z_{p,2}}{\left(Z_{p,1} + Z_{p,2}\right)^2} \tag{2.11}$$

By combining Eqs. (2.9) and (2.11), the thermal boundary conductance using AMM can be calculated.

2.2.2 Diffuse Mismatch Model (DMM)

Since AMM does not account for the discrete nature of the interface, it only works when the phonon wavelength is larger than interfacial roughness [50]. Moreover, AMM works best at very low temperatures where the wavelength of phonons is considerably larger than the lattice constant so that the phonons are not disturbed by the discrete nature of the lattice. However, as the temperature increases (T > 30 K), the phonon wavelengths become comparable to the length scale of atomic roughness [48, 53]. A quantitative estimate shows that the average phonon wavelength at room temperature is ~ 10-20 Angstrom in many materials [52], which is enough to be scattered diffusively by roughness of the interface [52]. For both of these examples (non-smooth interfaces, and at moderate temperatures), phonons can be scattered diffusively from the interface, and the scattering from the interface is not specular anymore (Figure 2-6).

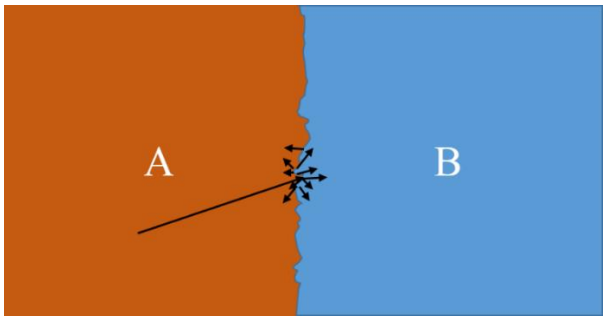

Figure 2-6. Diffusive scattering at an interface.

In order to describe the diffusive behavior of the scattering events at interfaces, Swartz and Pohl proposed the diffuse mismatch model (DMM) in 1987 [54, 55]. In contrast to AMM where the incident and the reflected waves were related, it is assumed in DMM that phonons can scatter in any direction [4] [20, 56], although they still retain their energy (i.e. the same frequency) [5] [20]. As a result, it is not possible to know if a phonon is being reflected or transmitted [50]. Instead, the transmission probability is proportional to the phonon density of states of the both sides of the interface, while the principle of detailed balance holds [20, 49]. In another words, while in the AMM the difference in the acoustic impedance of the materials forming the interface dominates the transmission probability, in the DMM the difference between the phonon density of states is the determining factor [57]. Therefore, as the mismatch between the acoustic impedances in AMM and the mismatch between the phonon densities of states of the two materials in DMM increases, the value of the thermal boundary conductance decreases.

As mentioned before, in order to calculate the thermal boundary conductance, the transmission probability as well as materials properties such as density of states need to be known.

In order to obtain the phonon density of states, the phonon dispersion needs to be known accurately. However, the Debye model can be used as an approximation to calculate the phonon dispersion in some cases [56]. Based on the Debye approximation, for sufficiently low frequencies, the relation between the frequency and wave vector of phonons is linear. At temperatures below the Debye temperature of both the materials forming the interface, the Debye approximation can

[4] Each scattering event respects momentum conservation. However, on average there is no correlation between incident and reflected/transmitted waves. Therefore, the specular condition can be dropped.
[5] This is in the case of elastic scattering. Other DMM models have been introduced to account for inelastic scattering and multiple-phonon scattering events.

be used. Therefore under the Debye approximation, the transmission probability can be calculated as [48]:

$$\alpha_{12} = \frac{\sum_p 1/v_{p,2}^2}{\sum_p 1/v_{p,1}^2 + 1/v_{p,2}^2} \tag{2.12}$$

However, as the temperature increases, the linear approximation of the Debye model breaks down and a more realistic phonon dispersion is required [49].

Many studies have shown that different parameters could affect the thermal boundary conductance of a system. Thus, often times there are discrepancies between the theoretical calculations and experimental measurements. This discrepancy can become even larger than an order of magnitude depending on the acoustic mismatch of the materials [58]. To resolve this issue, extensions to DMM have been proposed. While some of these extensions, such as using exact phonon dispersions and including electron-phonon coupling effects, help with explaining the results of acoustically matched interfaces [58], some other extensions such as, incorporating inelastic scattering, improve the analysis for acoustically mismatched interfaces [58]. As another example, the thermal boundary conductance obtained by Eq. (2.12) considering the Debye approximation for phonon density of states breaks down at higher temperatures. To resolve this issue, a correction that includes the effects of volumetric internal energy $\left(U(T) = \int_0^T C(T)dT\right)$ was proposed [49]:

$$\alpha_{12} = \frac{v_{p,2} U_{p,2}(T)}{v_{p,1} U_{p,1}(\mathrm{T}) + v_{p,2} U_{p,2}(\mathrm{T})} \tag{2.13}$$

It is worth mentioning that while the DMM generally describes the phonon-mediated interfacial thermal transport, an electronic version of it successfully described the thermal boundary

conductance of metal/metal interfaces of Al/Cu [59] and Pd/Ir [60]. The thermal boundary conductance in this electronic version of DMM is described by [60]:

$$G = \frac{Z_1 Z_2}{4\left(Z_1 + Z_2\right)} \tag{2.14}$$

where $Z = \gamma v_{fermi} T$ with γ being the material's Sommerfeld parameter, T the temperature and v_{fermi} the Fermi velocity.

2.2.3 Thermal Boundary Conductance of Different Structures

Thermal boundary conductance of several systems under different conditions have been measured using different techniques. A plot summarizing some of these results is shown in Figure 2-7. Moreover, the equivalent thickness $\left(d\right)$ of SiO_2 to achieve the same conductance $\left(G = k_{SiO2}/d\right)$ at each interface is also presented in the same plot. Since metals are highly electrically and thermally conductive, metal/metal interfaces usually have high thermal boundary conductance. At room temperature, the largest thermal boundary conductance measured (14±3 GW/m^{2}K) belongs to Pd/Ir [60], followed by ~ 4.7 GW/m^{2}K for a Cu/Nb interface [61] and ~4 GW/m^{2}K for an Al/Cu interface [59].

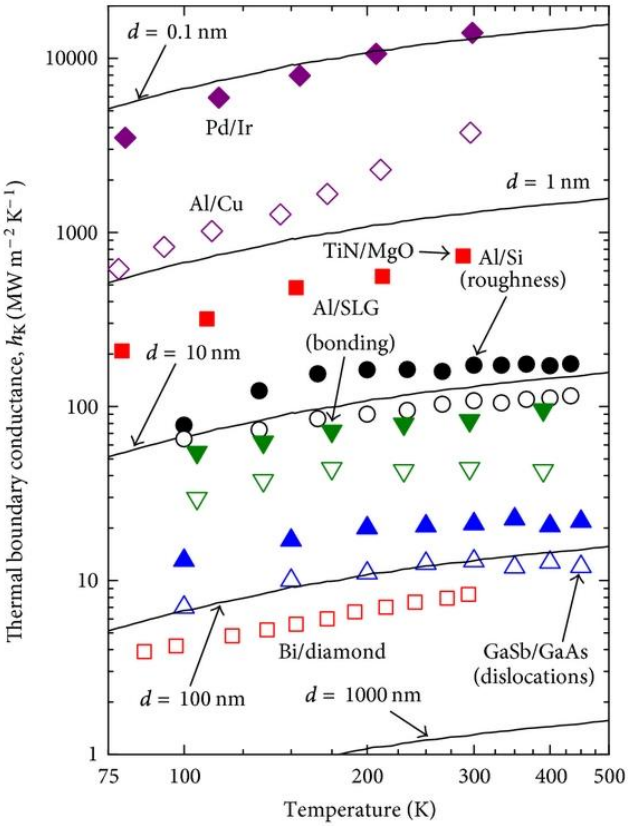

Figure 2-7. Thermal boundary conductance for different solid/solid systems [15] [6]. The solid line represents the equivalent thickness of SiO_2 to have the same conductance. Reduction of TBC is observed for Al/Si (roughness) curve by introducing interfacial roughness (filled and unfilled circles), and for GaSb/GaAs (dislocations) by introducing higher number of interfacial dislocations (filled and unfilled triangles). Whereas TBC was increased for Al/SLG (bonding) through strengthening the bonds between Al and SLG (filled and unfilled inverted triangles).

On the other side of the spectrum for phonon dominated interfaces, thermal b1oundary conductance as low as 8.5 MW/m^{2}K for Bi/diamond [62] and as high as ~700 MW/m^{2}K for TiN/MgO [63] have been reported. The low thermal boundary conductance of Bi/diamond can be explained by the high dissimilarity between their Debye temperatures. As such, many phonons

[6] This plot from Ref. [15] is under the Creative Commons Attribution License and properly cited re-use is permitted.

cannot traverse from the high-Debye-temperature material across the interface to the low-Debye-temperature material because of the absence of suitable phononic states, though inelastic scattering can increase the transmission.

2.2.4 What Extrinsic Factors Affect the Thermal Boundary Conductance?

When structures are fabricated, the interfaces are usually not completely sharp and perfect. In general, interfacial disorder and roughness decrease the thermal boundary conductance across interfaces. Interfacial bonding strength affects the thermal boundary conductance as well [57]. Another practical method to change the thermal boundary conductance of an interface is to incorporate an interstitial layer between the materials forming the interface. It has been shown that using a Ti layer can increase the thermal boundary conductance by several times [53, 64, 65]. More than a factor of 2 or 4 enhancement of thermal boundary conductance was observed by using a 1 nm layer of Cu or Cr as layers at the interface of Au/sapphire, respectively [66].

2.3 Thin Film Thermal Measurement Techniques

Over the years different techniques have been developed to study thermal properties of thin film materials. 3ω and optical pump-probe techniques are examples of these methods. Depending on the advantages and disadvantages of each technique, they can be used to study thermal properties of different structures.

2.3.1 3ω Method

Firstly described and implemented by Cahill and coworkers [67, 68], the 3ω method uses a metallic layer (such as Au or Pt with adhesive layers such as Cr or Ti) as both heater and thermometer, which is patterned on the surface of a sample [69]. The heater/thermometer is then subjected to a modulated electric current which causes a temperature gradient through the film of interest due to joule heating [69].

Because of the modulation of the electrical current with the frequency of ω, the resultant joule heating causes the temperature of the sample to change with the frequency of 2ω (joule heating is the same regardless of the direction of current flow). The amplitude and phase of the temperature fluctuations depends on the thermal characteristics of the system [70]. These temperature fluctuations change the resistance of the metallic layer with the frequency of 2ω, and mixed with the electrical current at frequency of ω, a voltage signal at 3ω will be generated, which is affected by the thermal properties of the system [70]. The detection of the thermal oscillations at 3ω has advantages in terms of signal to noise ratio with respect to the signal at 2ω, which in principle is equally as meaningful to extract the thermal properties of the system.

However, despite its simplicity, the 3ω method has some limitations. In order to study samples with 3ω method, the metallic layer needs to be patterned on the surface of the sample. As a result, micro-fabrication processes are necessary. Moreover, when investigating electrically conducting or semi-conducting materials, an electrically insulating layer (usually a thin layer of dielectric such as *a*-SiO_2) needs to be placed between the metallic layer and the thin film of the interest [69]. Therefore, the accuracy and the sensitivity of the measurements can be affected by the additional thermal resistance induced by the insulating layer [69]. The most important limitation of the 3ω

method is that the modulation frequency is typically limited to 100 kHz [23]; this limits the thermal penetration depth of the heat waves and the ability to characterize heat transport at small length scales. The penetration depth is expressed as $L_P = \sqrt{k / \pi C f}$, where k is the thermal conductivity, C is the volumetric heat capacity and f is the modulation frequency. Therefore a modulation frequency of 100 kHz leads to a thermal penetration depth of 17 μm in Si, limiting the access to transport over sub-micron length scales. To reach L_P = 1 μm in Si, f > 28 MHz is necesary.

2.3.2 Time Domain Thermo-Reflectance (TDTR)

Advances in optics and photonics have led to the development of optical metrology systems based on pump and probe techniques such as time domain thermoreflectance (TDTR) and frequency domain thermoreflectance (FDTR). Their popularity is driven in part by the simpler sample preparation, which unlike thermometry approaches do not require microfabrication or response calibration. FDTR and TDTR, along with their related techniques, allow in some cases simultaneous measurement of several thermal properties of bulk and thin film materials. In FDTR and TDTR, a thin metallic layer is deposited on the sample surface, which acts as a transducer, serving as both heater and thermometer. Changes in the transducer's optical reflectivity as function of temperature (thermoreflectance) allows a probing laser to sense the temperature changes induced by a pump laser beam.

TDTR employs ultrafast laser pulses to study thermal properties of thin structures. The output of a mode-locked laser is split into two branches of pump and probe beams. The modulated train of ultrafast pump laser pulses causes the surface temperature of the sample to change and the changes are monitored with probe beam through changes in reflectivity as a function of time [71, 72]. The

use of modulated pulses allow for lock-in detection and amplification and therefore increases signal to noise ratio. A variable optical delay stage is used to change the delay between pump and probe beams. By varying the delay between pump and probe pulses, pico-second to nano-second time evolution of the surface temperature of the sample is observed and therefore nano-second and pico-second carrier dynamics can be studied; an improvement over 3ω method. An example of a TDTR setup is shown in Figure 2-8.

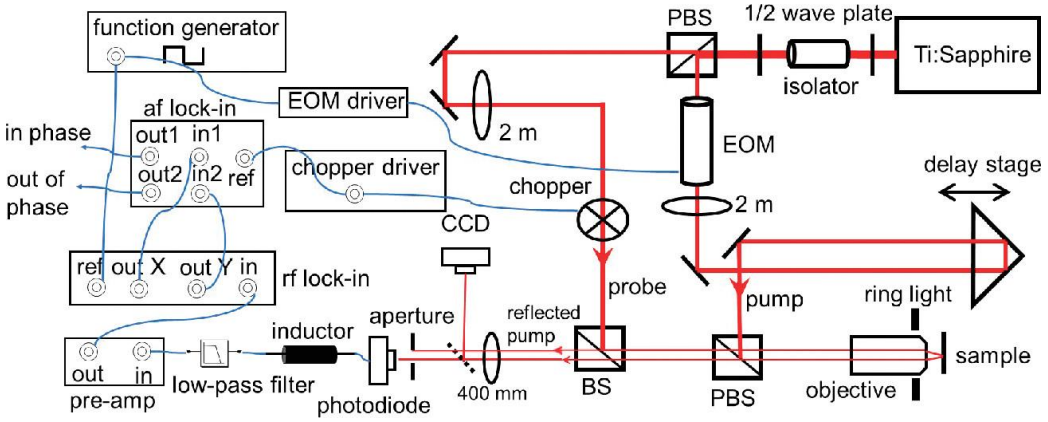

Figure 2-8. A TDTR setup [73]. EOM, PBS, and BS stand for electro-optic modulator, polarizing beam splitter, and non-polarizing beam splitter. Reprinted with permission from Rev. Sci. Instrum. 87, 064901 (2016). Copyright 2016 American Institute of Physics.

2.3.3 Frequency Domain Thermo-Reflectance (FDTR)

Although TDTR is a robust and powerful technique for measuring thermal properties, it is expensive and requires a complicated setup. FDTR and its variations, which are the methods of interest in this dissertation [7], are another non-contact method to measure thermal properties of

[7] FDTR will be discussed in more detail in section 3.1.

structures [74]. In contrast to TDTR, FDTR is less expensive and easier to build and maintain. The first implementation of the FDTR was presented by Schmidt and coworkers to obtain heat transport measurements with a modulation frequency of up to 20 MHz [75, 76]. Since then, FDTR has been improved over time. For instance, FDTR was used to simultaneously measure thermal conductivity and volumetric heat capacity of bulk and thin films [77], and was extended into an imaging technique to produce thermal maps of thermo-physical properties [78]. The same technique was used by Yang and co-workers to measure the in-plane thermal conductivity and the thermal boundary conductance (TBC) of a metal/graphene/SiO_2 structure by increasing the pump modulation frequency up to 50 MHz [42]. While in TDTR the phase lag between pump and probe beams is monitored as a function of time delay between the beams at a fixed modulation frequency, in FDTR the phase lag between pump and probe beams is measured as a function of modulation frequency. In both cases the phase lag is then fitted to the solution of the heat diffusion equation to extract unknown thermal properties of the sample [16, 79]. The FDTR setup implemented in our lab is shown in Figure 2-9.

We recently demonstrated how further combining a beam-offset approach with high frequency FDTR performed using small spot sizes can lead to lower uncertainties in the measurement of thermally anisotropic samples [80]. This will be covered in section 3.2.

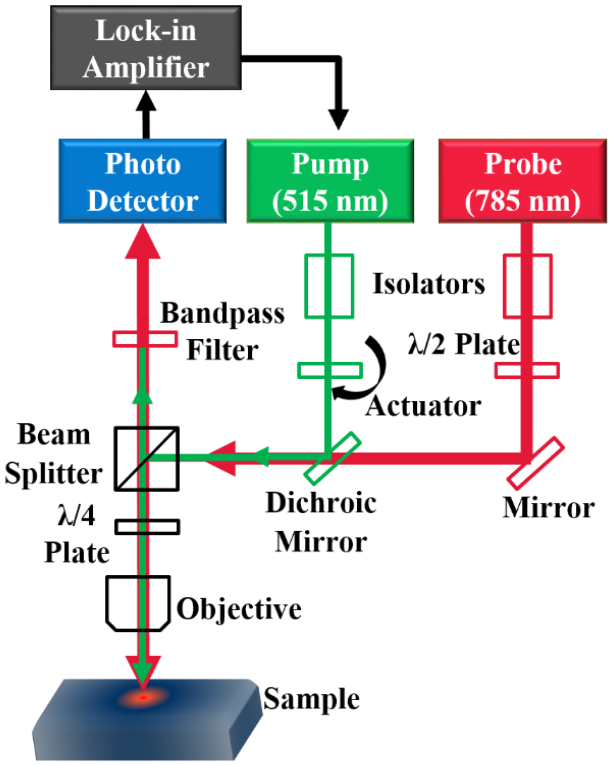

Figure 2-9. A schematic of our typical FDTR setup.

2.3.4 Broad-Band Frequency Domain Thermo-Reflectance (BB-FDTR)

As discussed earlier, a systematic change of thermal penetration depth (L_P) through heating frequency (as an example of L_c) allows for studying the contribution of heat carriers with different MFP to the thermal conductivity. Furthermore, as thermal penetration depth is inversely proportional to the heating frequency ($L_P = \sqrt{D/\pi f}$), by increasing the heating frequency and subsequently decreasing the thermal penetration depth, heat carriers with smaller MFP (in other words, thinner materials) can be studied.

However, with the modulation frequency of the pump in FDTR going beyond 20 MHz, the signal to noise ratio drops down significantly. This is mainly due to increasing coherent pickup of the

modulation signal by the receiver electronics, as well as amplitude reduction of the surface temperature response. It can be shown that for an isotropic slab with thermal conductivity of k and volumetric heat capacity of C under a one-dimensional heat flux $q = q_0 e^{ift}$ with frequency of f, the surface temperature $\left(T\left(z=0\right)\right)$ is [16]:

$$T\left(z=0\right) = \frac{q_0}{\sqrt{kCf}} \exp\left[i\left(ft - \pi/4\right)\right] \tag{2.15}$$

Eq. (2.15) shows that the surface temperature amplitude is proportional to $1/\sqrt{f}$. Therefore by increasing the modulation frequency of the heat flux, the surface temperature amplitude and consequently the thermal signal strength decreases.

Accordingly, most FDTR measurements have been performed up to 20 MHz [14, 16]. In order to enhance the signal to noise ratio at increasing frequencies and be able to study thinner structures, a modification of FDTR also known as the Broad-Band FDTR (BB-FDTR) was introduced [14, 16]. BB-FDTR employs a heterodyne approach to detect signals with modulation frequencies up to 200 MHz [14]. BB-FDTR has also been used to measure the phonon MFP spectra [14].

In order to improve the SNR of FDTR, Regner and co-workers used a heterodyning approach to shift the detection of the high-frequency thermal signal to a lower frequency before optical detection, thereby limiting RF noise in the detection cabling and electronics [16]. More specifically, in their work, an external electro-optic modulator (EOM) modulates the output of the pump laser at f_1 while the CW probe laser measures the surface temperature of the sample (Figure 2-10). Then another EOM working at f_2 is placed before the detector and modulates the probe light reflected from the sample, generating heterodyne frequencies at $f_1 \pm f_2$. The

component of $f_1 - f_2$ is then detected. As the thermal response is measured at the heterodyne frequency of $f_1 - f_2$, which can be freely selected, having a low heterodyne frequency results in lower noise [16]. This is because a great deal of the noise in the detection circuit at frequencies > 10 MHz results from coherent RF pickup between the cables connecting signal generator and modulator to the cables connecting photodetector and lock-in amplifier. By detecting at $f_1 - f_2$, the coherent noise at frequencies f_1 and f_2 is rejected.

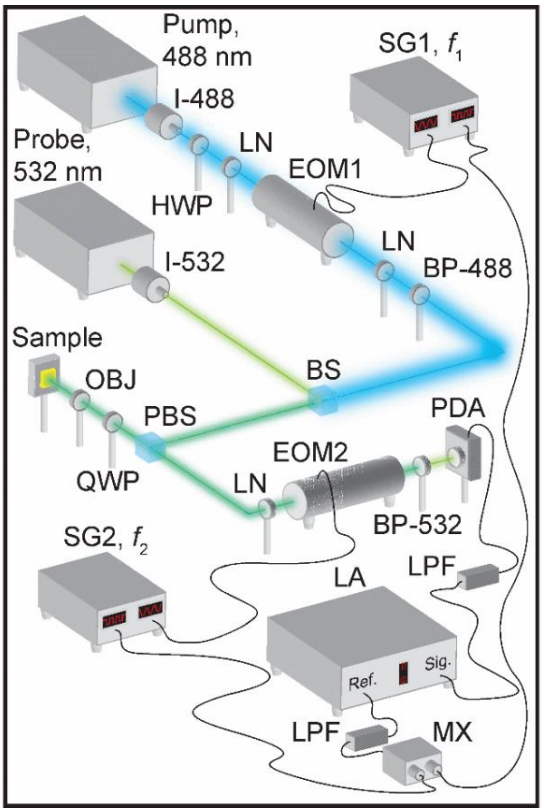

Figure 2-10. A schematic of BB-FDTR [16]. Two electro-optical modulators generate the two frequencies for heterodyne detection. Abbreviations are as follows: I-488/532: 488/532 nm isolator, BS: beam splitter, PBS: polarizing beam splitter, QWP: quarter wave plate, HWP: half wave plate, LN: focusing lens, BP-488/532: 488/532 nm bandpass filter, PDA: amplified photodiode, EOM1/EOM2: electro-optic modulator at 488/532 nm, OBJ: objective, LA: lock-in amplifier, SG1/SG2: signal generator, MX: electronic mixer, LPF: low pass filter. Reprinted with permission from Rev. Sci. Instrum. 84, 064901 (2013). Copyright 2013 American Institute of Physics.

In FDTR and its related techniques, the quantity of interest is the thermal phase lag of the temperature of the sample with respect to the heat flux generated by the pump beam. To isolate the thermal phase from other experimental sources of phase offset, a reference measurement is needed (described in more detail in section 3.1) [16].

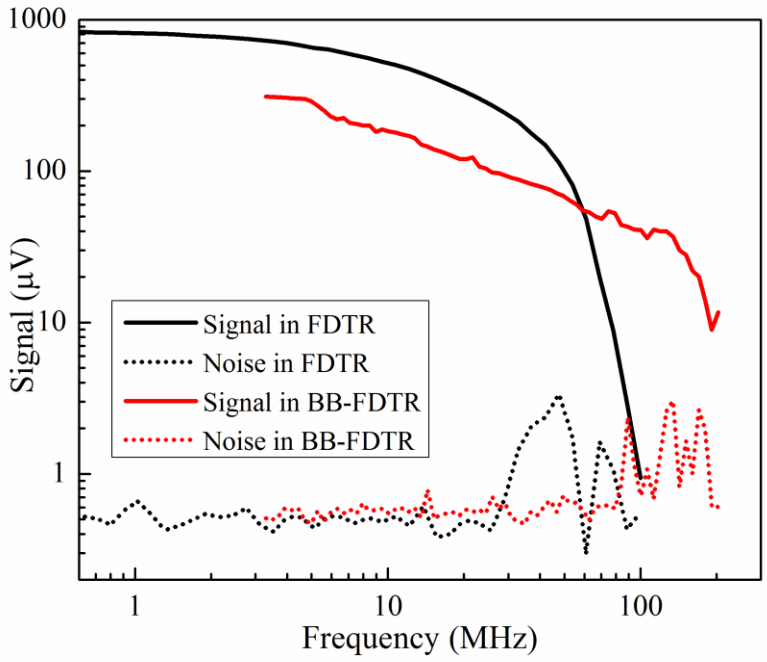

Figure 2-11. A comparison between strength of thermal signal and noise in a typical FDTR measurement and a BB-FDTR measurement.

Figure 2-11 shows the SNR for a BB-FDTR measurement based on the heterodyning approach introduced by Regner and co-workers. Using a heterodyne frequency of 100 kHz, the SNR becomes smaller than 10 at around 170 MHz in comparison with typical FDTR where this happens at around 70 MHz (Figure 2-11). The test sample in this case is a multi-layered Al(59nm)/SiO_2(150nm)/Si sample, under incident powers of 10 mW and 18 mW of 515 nm and

785 nm, respectively with rms spot size of ~ 1.4 μm. The BB-FDTR technique developed by Regner and co-workers requires the use of two EOMs, which add significantly to the cost of implementation. While the signal depicted in Figure 2-11 represents the amplitude of the thermal signal detected by probe laser through thermoreflectance, noise is extracted by detecting the probe laser while the pump laser is blocked.

2.4 Sample Preparation and Ancillary Characterization

As the presence of a transducer is vital for thermoreflectance studies, in this section the properties of the transducer will be reviewed. Then, the knife-edge profiling technique as a method to measure beam spot size will be discussed. Finally, the four-point probe technique to measure the electrical conductivity of the transducer will be introduced. The transducer characteristics and beam spot size are necessary to relate the optical measurements to the thermal properties of interest.

2.4.1 Sample Preparation: Transducer

In order to make a TDTR or FDTR measurement, the sample needs to have a thin metallic layer deposited on its surface, which is often referred to as the transducer. This transducer acts as both heater and thermometer; as it absorbs heat from the pump laser to generate the heat flux stimulus, and converts the surface temperature variations to intensity changes in the reflected probe beam [69]. The temperature-dependent behavior of the transducer is explained by its coefficient of thermo-reflectance at a given wavelength [16]:

$$\beta_\lambda = \left[1/\Re_{o,\lambda}\right]\left[d\Re_\lambda(T)/dT\right] \tag{2.16}$$

where $\Re_{o,\lambda}$ and $\Re_\lambda$ are the room temperature nominal reflectivity and the temperature dependent reflectivity, respectively, at wavelength λ [16]. It should be noted that Eq. (2.16) is based on the assumption of linear dependence of the reflectivity on temperature. That is not typically the case, therefore the temperature changes should be kept small.

The thickness of the transducer is usually between 50 to 100 nm [78], thick enough to be considered as an optically opaque layer on top of the sample [81]. If the transducer is optically too thin, then part of the beam reaches the layers beneath the transducer and therefore the optical properties of all of the layers need to be considered in the model in the order to fit for thermal properties, and the thermal model needs to consider sub-surface heat sources [81]. If the transducer is too thick, on the other hand, the temperature drop across the transducer increases and the sensitivity to thermal properties of the underneath layers decreases [81]. Precise knowledge of the thickness of the transducer and its thermal properties is essentially important when analyzing FDTR/TDTR measurements. Choosing the appropriate material as the transducer not only increases the signal to noise ratio, but also reduces the optical penetration depth and prevents volumetric heating in the sample [16].

In order to select a good material as the transducer, several points need to be accounted for. Since the signal in a FDTR measurement is proportional to the thermo-reflectance coefficient (Eq. (2.16)) of the transducer and the temperature variations of the surface of the sample [16], the transducer needs to be chosen such that it features high thermo-reflectance coefficient at the wavelength of the probe laser [16]. While the characteristics of the transducer are essential in FDTR, the choice of material does not change the measured thermal conductivity of the sample beneath [69].

Recently the analysis of the optical and thermal transport in thermoreflectance measurements has been further refined to allow FDTR characterization of semiconducting samples without the need for a transducer [82].

Al, Pt, Au, and Ag are considered as popular choices for transducer [17, 81], depending on their absorption coefficients at the pump wavelength and the thermo-reflectance coefficients at the probe wavelength. Aluminum (Al) is often used when the temperature of the measurement is not high, as Al has a relatively low melting point [69]. When the measurement temperature is high, Platinum (Pt) can be used instead [69].

2.4.2 Four-Point Probe Measurement

In the four-point probe measurements, an electrical current is supplied by two probes and sensed by two other probes (Figure 2-12). The use of 4 probes allows to remove the contribution of contact resistance and obtain directly the resistance of the sample. By measuring the sheet resistance using this method and utilizing the Wiedemann-Franz law, the in-plane thermal resistivity/conductivity of a thin film with known thickness can be calculated. This is done routinely to determine the transducer thermal conductivity in thermoreflectance measurements.

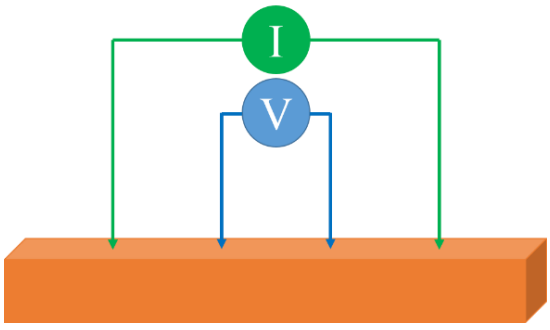

Figure 2-12. Schematic of a four-point probe measurement.

2.4.3 Knife-Edge Technique

In order to measure the laser beam spot size, a knife-edge profiling technique is used, in which a sharp edge such as that of a doctor blade is scanned across the focal plane of a focused light beam to determine its diameter. A photodetector or a power meter collects the laser beam that is reflected from (or transmitted through, depending on the relative position of the detector) the cleaved edge of a crystal such as a Silicon wafer. By precisely moving this edge and measuring the amount of light getting to the detector, the beam profile can be determined. Assuming a TEM_{00} beam with Gaussian intensity profile of [17]:

$$I(r) = \frac{2A_0}{\pi\omega_0^2}\exp\left(\frac{-2r^2}{\omega_0^2}\right) \tag{2.17}$$

where A_0 is the beam power and ω_0 is the $1/e^2$ of beam radius. The laser beam can be assumed to be Gaussian (which is an appropriate approximation in most situations), and the resulting profiles in the x and y directions will be the same. Moving the edge of a sample in the x direction, and performing a Gaussian fit on the derivative of the total intensity of light collected by the detector [17]:

$$I(x) = \frac{A_0}{\omega_0}\sqrt{\frac{2}{\pi}}\int_{-\infty}^{x} dx \exp\left(\frac{-2x^2}{\omega_0^2}\right) \tag{2.18}$$

the spot size ω_0 can be measured. An example of this has been plotted in Figure 2-13.

It is noteworthy to mention that the one-dimensional spot size measurement mentioned above relates to the beam size in the x direction. If the beam profile is not circular, the profile along the y direction will differ [17].

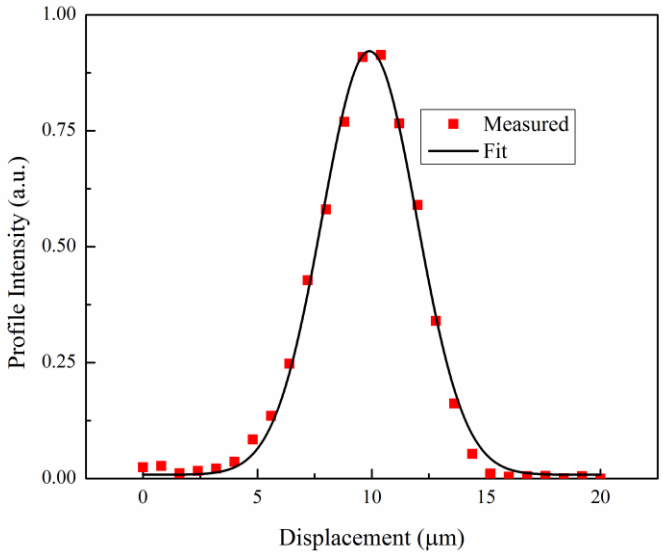

Figure 2-13. Measured intensity profile and its Gaussian fit, yielding a spot size and its lateral displacement.

In order to accurately measure the beam spot sizes as they are in the thermal measurement, it is vital for the beams to be on the same focal point that they were in the thermal measurement. In order to achieve the same focal point for both thermal and spot size measurements, several methods can be employed. For instance, a CCD camera can be used to inspect the focal position of the laser and ensure that the sample is in the same focal point [78]. Another method is to maximize the thermoreflectance signal while profiling and while performing thermal measurements [14].

2.5 Determining thermal properties from thermoreflectance measurements

The unknown thermal properties of interest can be extracted by fitting FDTR/TDTR measurement data to a solution of the heat equation. Cahill described the heat transport in a semi-infinite isotropic layered system illuminated by concentric Gaussian-shaped pump and probe beams in the frequency domain in a cylindrical coordinate system [83]. Schmidt *et al.* extended the solution to

account for anisotropic thermal conduction [39]. They also showed that by appropriately choosing the pump and probe spot sizes as well as the modulation frequency, they could measure both in-plane and out-of-plane thermal conductivity of thermally anisotropic materials [39]. Feser and Cahill provided an alternative method to measure the in-plane thermal conductivity of anisotropic layered materials by using a lateral offset between axisymmetric pump and probe beams, under the condition that the lateral diffusion is comparable with the laser spot size [38]. They then extended their method for non-transversely isotropic systems with arbitrary thermal conductivity tensor and general laser intensity profiles, as long as the spot sizes are comparable or smaller than in-plane heat diffusion [71].

Here, we review the frequency domain solution for the surface temperature presented by Feser and Cahill to account for beam offset as well as anisotropic transport in layered materials [38]. It should be noted that, in what follows, heat transport is treated diffusively and non-diffusive transport can be seen as a deviation that yields "unexpected" thermal properties. While deviations from the diffusive model can be used to investigate non-diffusive transport in materials with known thermal properties, it is harder to make this distinction for materials that are not as well known. In this case, tests for non-diffusive transport should be carried out. This issue is discussed in more detail in Chapter 5.

One-dimensional (z direction) transient heat conduction can be expressed using heat diffusion equation:

$$C\frac{\partial T}{\partial t} = k\frac{\partial^2 T}{\partial z^2} \tag{2.19}$$

The temperature fluctuations of a layered system imposed by a Gaussian pump beam and detected by a Gaussian probe beam that can be fit to the FDTR experimental data is described as:

$$\Delta T(f) = \frac{2\pi}{A_s}\int_0^\infty G(f,h)P(h)S(h)hdh \tag{2.20}$$

for which three main ingredients are needed: the Hankel transforms of the intensity profiles of the pump $P(h)$ and probe $S(h)$ beams, and the Green's function solution $G(f,h)$ for the temperature response of the system under a periodic point heat source of unit power with the frequency of f [38].

$G(f,h)$ can be calculated iteratively from:

$$G(f,h) = \left(\frac{B_1^+ + B_1^-}{B_1^+ - B_1^-}\right)\frac{1}{\gamma_1} \tag{2.21}$$

with:

$$\begin{pmatrix} B^+ \\ B^- \end{pmatrix}_n = \frac{1}{2\gamma_n}\begin{pmatrix} \exp(-u_n t_n) & 0 \\ 0 & \exp(u_n t_n) \end{pmatrix} \times \begin{pmatrix} \gamma_n + \gamma_{n+1} & \gamma_n - \gamma_{n+1} \\ \gamma_n - \gamma_{n+1} & \gamma_n + \gamma_{n+1} \end{pmatrix}\begin{pmatrix} B^+ \\ B^- \end{pmatrix}_{n+1} \tag{2.22}$$

$$u_n = \left[4\pi^2 h^2\left(\frac{k_r}{k_z}\right) + q_n^2\right]^{1/2} \tag{2.23}$$

$$q_n^2 = \frac{i2\pi f}{D_{z,n}} \tag{2.24}$$

$$\gamma_n = k_{z,n}u_n \tag{2.25}$$

where the n is the layer number (n = 1 for the topmost layer), k_r and k_z are the in-plane and out-of-plane components of the thermal conductivity, D_z is the out-of-plane thermal diffusivity, t is the thickness, and h is the Hankel transform variable. The bottom-most layer can be assumed to

be semi-infinite if the thermal waves don't penetrate through its thickness, and therefore for the last layer B^+ and B^- are set to 0 and 1, respectively.

The intensity of a Gaussian distributed pump laser beam, with ω_0 being the $1/e^2$ radius and A_P being the total absorbed intensity, can be described as:

$$p(r) = \frac{2A_P}{\pi\omega_0^2} \exp\left(\frac{-2r^2}{\omega_0^2}\right) \tag{2.26}$$

The Hankel transform of $p(r)$ is then written as:

$$P(h) = A_P \exp\left(\frac{-\pi^2 h^2 \omega_0^2}{2}\right) \tag{2.27}$$

The last ingredient is the Hankel transform of the intensity profile of the probe beam. In case of a probe beam coaxial with the pump beam, $S(h)$ would be similar to Eq. (2.27). However, when there is a lateral offset between pump and probe beams [38]:

$$\begin{aligned} S(h) = \frac{A_S}{\pi} \exp\left(-\left[\left(\frac{\sqrt{2}x_0}{\omega_1}\right)^2 + \left(\frac{\pi\omega_1 h}{\sqrt{2}}\right)^2\right]\right) \\ \times \sum_{n=0}^{\infty} \frac{1}{(n!)^2} \left(\frac{\sqrt{2}x_0}{\omega_1}\right)^{2n} l_n\left(\frac{\omega_1 h}{\sqrt{2}}\right) \end{aligned} \tag{2.28}$$

where ω_1 is the $1/e^2$ radius of the probe beam, A_S is the intensity of the probe beam, and the polynomial $l_n(x)$ is defined recursively as:

$$l_{n+1}(x) = -\frac{1}{x}\left[\begin{array}{l}\left(\pi^2 x^3 - x\right) l_n(x) + \left(\frac{1}{4\pi^2} - x^2\right) l_n'(x) \\ + \frac{x}{4\pi^2} l_n''(x)\end{array}\right] \tag{2.29}$$

where l'_n and l''_n are the first- and second-order derivative of l_n and $l_0=\pi$.

The fitting routine is performed through a least squares algorithm in which the error between the measured phase and the modeled phase (Eq.(2.20)) is minimized [75, 84].

Chapter 3: FDTR Instrumentation

Chapter 3 has been partially adapted, with permission, from:

M. Shahzadeh, M. Rahman, O. Hellwig, and S. Pisana, "High-frequency measurements of thermophysical properties of thin films using a modified broad-band frequency domain thermoreflectance approach," *Review of Scientific Instruments*, vol. 89, no. 8, p. 084905, 2018. Copyright 2018 American Institute of Physics.

M. Rahman, **M. Shahzadeh**, P. Braeuninger-Weimer, S. Hofmann, O. Hellwig, and S. Pisana, "Measuring the thermal properties of anisotropic materials using Beam-Offset Frequency Domain Thermoreflectance," *Journal of Applied Physics*, vol. 123, no. 24, p. 245110, 2018. Copyright 2018 American Institute of Physics.

M. Rahman, **M. Shahzadeh**, and S. Pisana, "Simultaneous measurement of anisotropic thermal conductivity and thermal boundary conductance of 2-dimensional materials," *Journal of Applied Physics*, vol. 126, no. 20, p. 205103, 2019. Copyright 2019 American Institute of Physics.

3.1 FDTR

In FDTR, two light beams (usually referred to as pump and probe) are focused on the surface of a sample. FDTR can be implemented with both pulsed and CW lasers. If a pulsed laser is used, the two light beam branches usually come from the same laser [76], and then are separated in time by an optical delay stage (similar to TDTR) so that the probe beam is time-delayed by an appropriate amount, as determined by the sensitivity of the measurement and the sample of interest. The pump is intensity-modulated at a frequency f and this frequency is scanned to obtain data at multiple

frequency values. Likewise, in the case of CW lasers, a pump laser beam is intensity-modulated at a frequency f and scanned within a spectral range of interest [18]. A periodic heat flux is generated by the absorbed pump laser on a thin metallic layer on the surface of the sample, and therefore the surface temperature oscillates at the same frequency as the modulation frequency of the pump laser (*f*). The probe laser picks up the temperature response through the principle of thermoreflectance and becomes intensity-modulated at *f*. As both amplitude of the surface temperature and phase lag between the heat flux (generated by the pump laser) and the surface temperature (observed by the reflected probe laser) contain information about the thermal properties of the sample, these quantities will be used to extract the unknown thermal properties of the sample by fitting the measured temperature response to the solution of the heat diffusion equation (Eq.(2.20)) [16]. In the following we will focus on implementations of FDTR based on CW lasers.

The signal recorded by the detector from a FDTR measurement involves phase responses from the electronic and optical components, as well as the thermal response of interest. This phase lag needs to be referenced to extract the thermal phase and cancel out the extra phases. In FDTR, this is usually achieved by measuring a branch of the pump beam which passes through the same optics and electronics to cancel all the unwanted phases from the measurement except the thermal phase. This reference measurement contains a negligible amount of thermal phase information for two reasons: (1) the pump wavelength may have a negligible thermoreflectance coefficient, and (2) the thermoreflectance signal is much smaller than the reflectance (typically a factor of 10^4 smaller).

A schematic of a typical FDTR setup is presented in Figure 2-9. A lock-in amplifier (Zurich Instruments HF2LI) is used to modulate the intensity of the pump laser (Omicron A350 operating at 515 nm) while the probe (Omicron A350 operating at 785 nm) remains unmodulated. These two operating wavelengths were chosen in order to swap the role of the pump and probe lasers

according to the samples being study, so that the laser wavelength corresponding with the larger thermoreflectance coefficient of the sample is used as the probe. Typically, 515 nm and 785 nm are effective probe wavelengths when using Au and Al transducers, respectively. Optical isolators (Conoptics M711A and M712B) are used to minimize back-reflections that can destabilize the laser sources. We also avoid back-reflections of the probe from entering the pump, and vice versa, to prevent inadvertent intensity modulation through optical cavity modulation. Half-wave plates, a polarizing beam splitter and a quarter-wave plate are used to ensure maximum light throughput in a coaxial setup as light reaches the sample and is reflected back towards the detector. A 40X objective (Olympus RMS40X) is used to focus the beams on the surface of the sample. The small spot sizes obtained (~1.5 μm) improve the signal and improve sensitivity to in-plane thermal transport. This is in contrast with most TDTR and FDTR implementations that use beam sizes above 10 μm. The negative aspect of using smaller spot sizes is that a very careful spot size calibration is necessary to avoid errors in the data analysis. The surface temperature of the sample oscillates at the frequency of pump, as the pump light is absorbed on the transducer. The unmodulated probe laser samples the temperature response from the transducer by thermoreflectance, i.e. changes of reflectivity due to the surface temperature. The probe signal is then measured by a photodetector (Thorlabs PDA8A) and demodulated by the lock-in amplifier.

In order to isolate the thermal phase lag of interest in FDTR, two measurements are performed. The phase of the first measurement, the thermal measurement, has contributions from the thermal, optical and electrical phases with respect to a reference phase from the lock-in amplifier, i.e $\theta_1 = \theta_{Thermal} + \theta_{Optical} + \theta_{Electrical} + \theta_{ref}$. Then, a non-thermal measurement θ_2 is performed to recover the thermal phase of interest from other unwanted phases; i.e. $\theta_2 = \theta_{Optical} + \theta_{Electrical} + \theta_{ref}$.

Therefore $\theta_1 - \theta_2 = \theta_{Thermal}$. The non-thermal measurement is typically achieved by replacing a filter in front of the detector in order to measure the modulated pump, rather than the probe.

In order to check the validity of our FDTR measurements, we start by measuring standard samples using our FDTR setup depicted in Figure 2-9 and Figure 3-1.

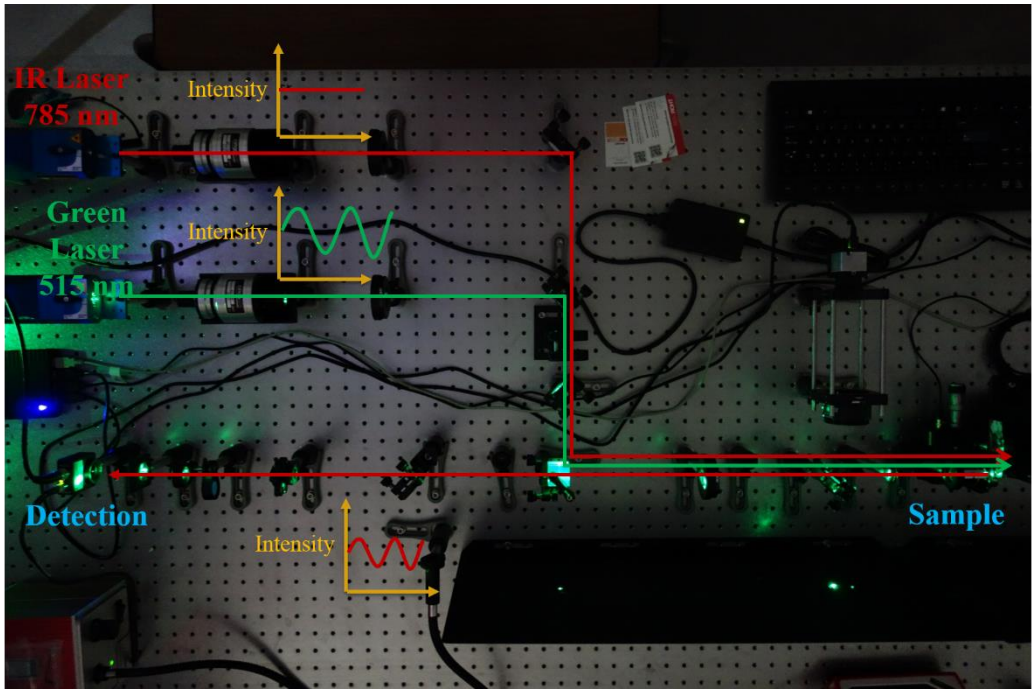

Figure 3-1 . Our typical FDTR configuration.

As an example, the result of a measurement performed up to 72.3 MHz on Al/SiO_2/Si (Figure 3-2) is presented. The data was modeled as a five-layer system consisting of three finite-thickness material layers and two interfaces. All material parameters and sources are shown in Table 3-1, and an RMS spot size of 1.15 μm was measured by the knife-edge technique. Fitting for the thermal conductivity of SiO_2 as a free parameter, the thermal conductivity of 1.28 ± 0.03 W/mK was

extracted. The results are in good agreement with the expected thermal conductivity of SiO_2 (1.3-1.4 W/mK). The thermal phase measured using our FDTR system and the fit from our model is also depicted in Figure 3-3.

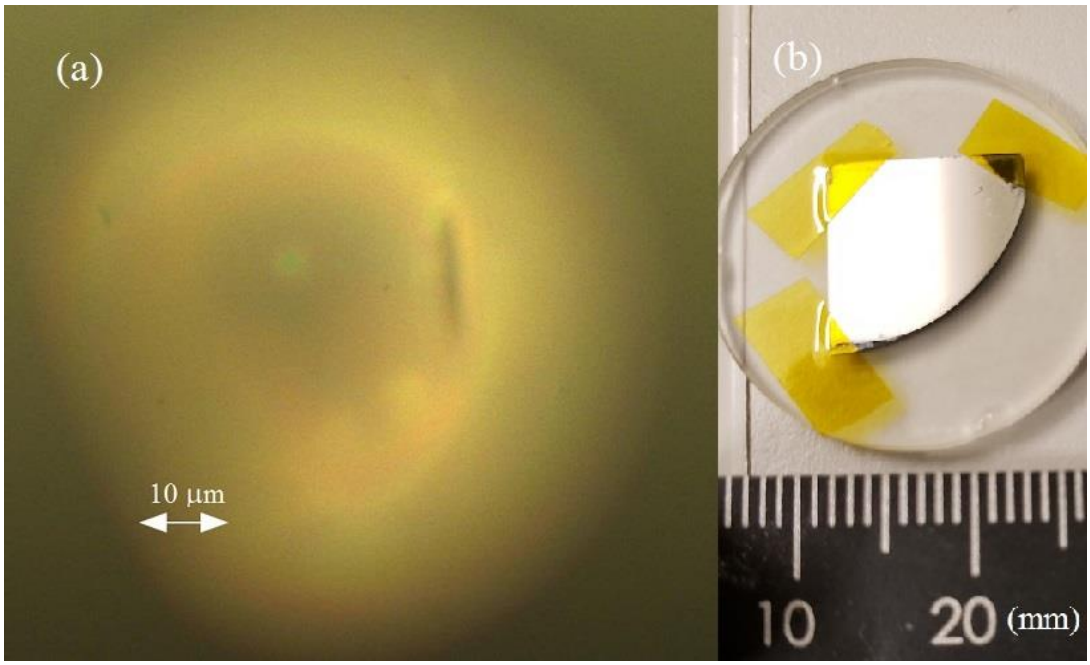

Figure 3-2. Image of the Al/SiO_2/Si sample (a) under microscope, and (b) taped for measurement.

Table 3-1. Material parameters used for fitting Al/SiO_2/Si system. The TBC of Al/SiO_2 and SiO_2/Si was set to 100 MW/m^{2}K and 28 MW/m^{2}K, respectively.

	k (W/mK)	C (MJ/m^{3}K)	t (nm)
Al	k_z = 243, k_r = 96.8	2.42	35
SiO_2	Determined by Fit	1.59	100
Si	145	1.64	Semi-Infinite

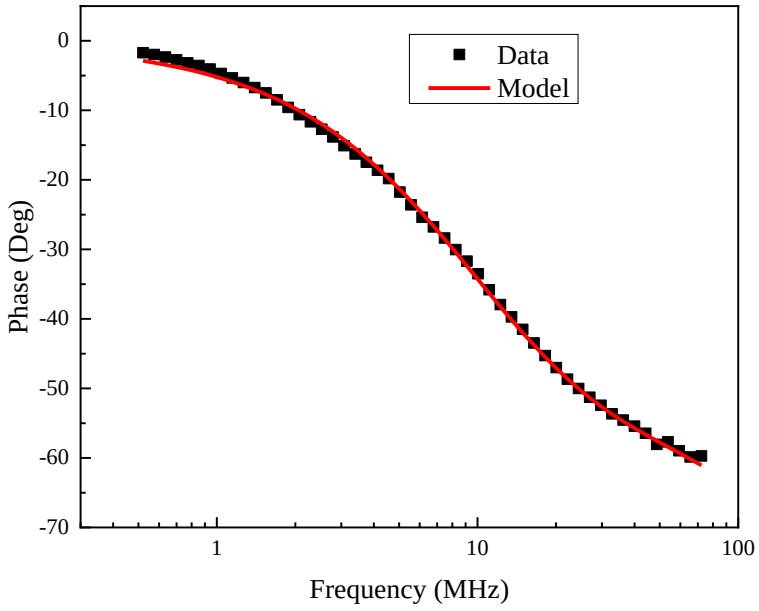

Figure 3-3. The measured thermal phase (black squared symbols) and the calculated fit (red line) for the Al/SiO_2/Si sample.

As mentioned earlier, the fitting routine is performed by a least squares algorithm. The error analysis is performed by calculating the variance of the desired parameters using the elements of variance-covariance matrix and calculating the standard deviation of the fitted parameters as a representation of the quality of fit. In case of the above example for thermal conductivity of SiO_2, the value of 1.28 ± 0.03 W/mK accounts for ~68% of the thermal conductivity uncertainty distribution.

3.1.1 Extension of FDTR to High Frequency

A useful method to increase the modulation frequency in FDTR while maintaining a sufficient SNR, is briefly described here which provides economical means to characterizing heat transport

at submicron length scales. This method doesn't rely on heterodyning to perform measurements at a frequency where RF noise is minimized (such as BB-FDTR discussed in 2.3.4). Instead, reducing the spot sizes leads to increases in the signal amplitude, due to the increase in the magnitude of the surface temperature oscillations. In this case, care must be taken to ensure that the temperature oscillations do not yield a nonlinear thermoreflectance response, that the local temperature rise is not above the desired value or result in irreversible sample modification. This can be done by checking that the thermal phase obtained is power-independent. Reducing the spot size also increases potential sources of error in accurately determining the spot size, therefore local spot size measurements for each sample are important. A lock-in amplifier capable of demodulating the signal at the selected frequency range is needed. Here we use a Zurich Instruments HF2LI lock-in amplifier. Although the nominal bandwidth of the HF2LI is 50 MHz, and the signal strength is reduced beyond this, the instrument is capable of demodulating signals up to 100 MHz. The use of several ferrite cores on the signal cables reduces coherent noise. In spite of the bandwidth limitations of both the lock-in amplifier and photodetector, we can perform measurements to ~100 MHz.

In order to further cancel residual RF noise in the detected thermal signal, we used a mathematical approach, since the noise is coherent with the signal. By subtracting at each frequency the measured complex noise vector (obtained by blocking the modulated probe laser light from the detector) from the measured complex signal vector, we obtain the thermal signal of interest. In practice, for the noise measurement, since we want to keep any source of coherent noise coming from the modulation process without directly detecting the modulated probe light, the probe laser is negatively biased to below the lasing threshold, but its modulation input is left on. This procedure facilitates automating the process of measuring the complex noise vector, as it is simpler

to implement than steering or filtering the probe light. The noise measurement was averaged to obtain a value with sufficient accuracy. We note that using small spot sizes not only increases the thermal signal, but also reduces the sources of coherent noise since the amplitudes of the voltage signals used to modulate the lasers while maintaining a sufficiently strong signal thermal signal are lowered.

Figure 3-4 shows the thermal phase measured using FDTR extended up to 90 MHz before and after the noise correction using the mathematical approach described above.

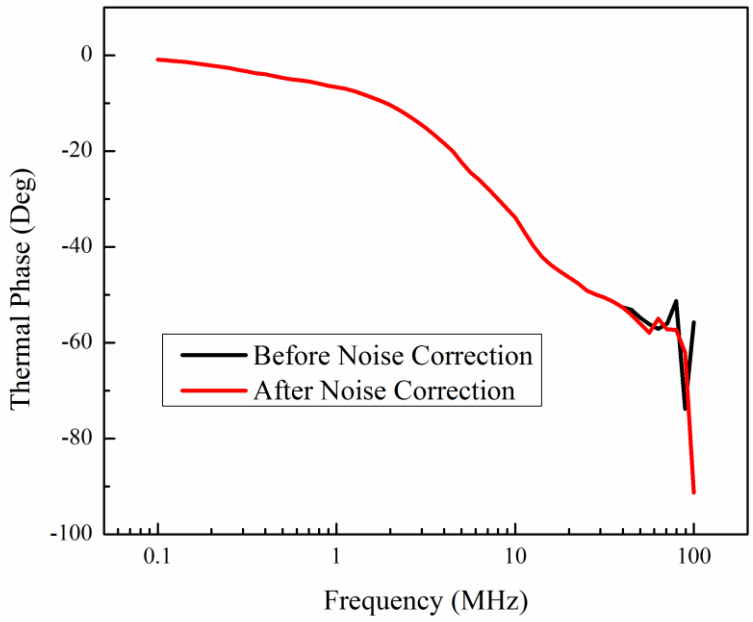

Figure 3-4. Extension of FDTR to 90 MHz; comparing the thermal phase before and after mathematical noise correction for Al/SiO_2/Si. The drop in SNR at higher frequencies is caused by the smaller FDTR signal and the nominal bandwidth of the lock-in amplifier, as well as greater coherent RF noise picked up by the electrical cables.

3.2 Beam Offset FDTR

3.2.1 Introduction

Both FDTR and TDTR are able to measure thermo-physical properties of a wide variety of materials. However, as the anisotropy of heat transfer increases, these methods do not have enough sensitivity to measure the in-plane thermal conductivity. This situation often takes place in 2D materials, where there is a strong in-plane thermal conductivity compared to a weak out-of-plane thermal conductivity. In addition to 2D materials, anisotropic heat transport becomes important in multilayers where there are several interfaces between layers impeding heat conduction [85, 86].

To show the effectiveness of using offset in FDTR measurements, an Al-coated substrate is considered. By fixing the spot size (1 μm), the Al/substrate TBC (150 MW/m^2K), and reference thermo-physical parameters of Al, the sensitivity to isotropic thermal conductivity of the substrate is examined by changing the pump and probe offset (0 and 1.5 μm). As Figure 3-5a shows, using offset increases the sensitivity to thermal conductivity regardless of the value of substrate's thermal conductivity.

Furthermore, Figure 3-5b depicts improvement of the sensitivity plot using offset when the substrate possesses anisotropic thermal conductivity (k_r = 10 W/mK and k_z = 1 W/mK).

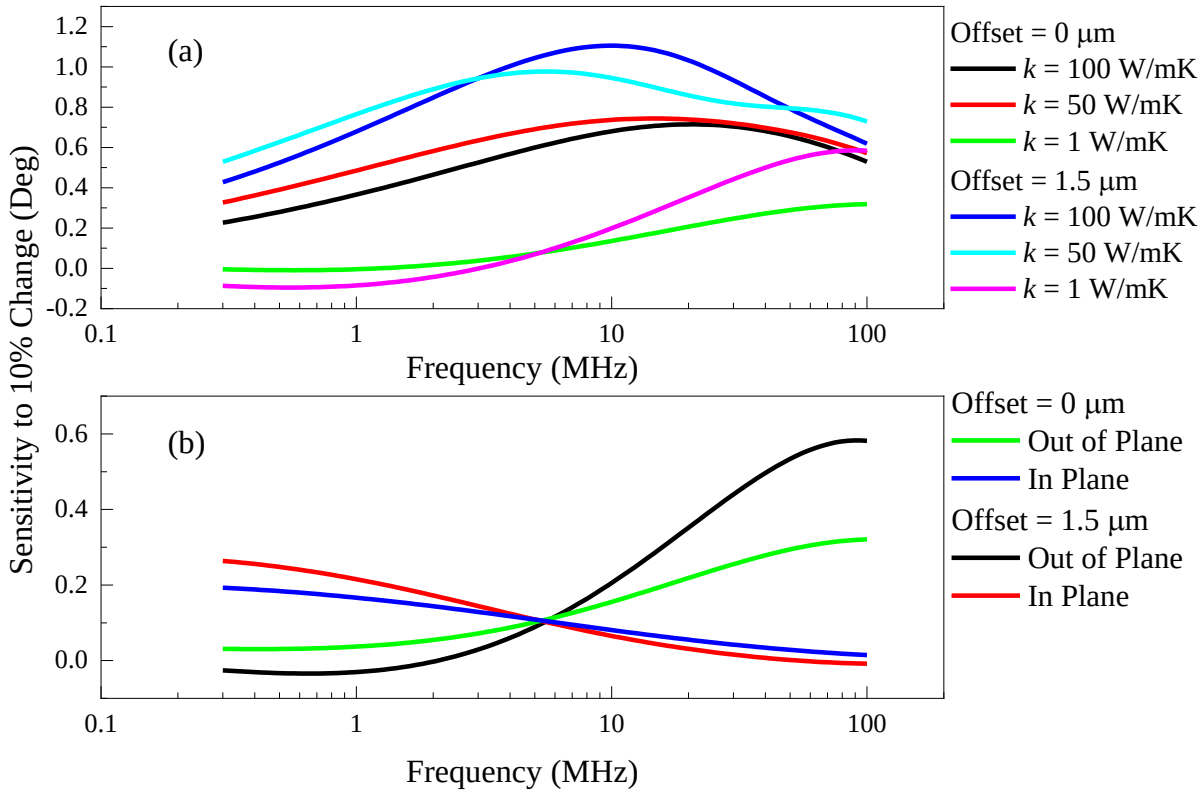

Figure 3-5. Phase sensitivity to 10% change of thermal conductivity with pump and probe offset values of 0 and 1.5 μm, and spot size of 1 μm. (a) isotropic thermal conductivities of 100, 50, and 1 W/mK. (b) Anisotropic thermal conductivity values of 10 W/mK and 1 W/mK for in-plane and out-of-plane components, respectively.

The sensitivity of measurement can be affected by spot size as well. For instance, Figure 3-7 shows that the sensitivity to in-plane thermal conductivity can be significantly enhanced by using a smaller spot size. Since the temperature fluctuations of the sample surface are inversely proportional to the spot size [83], using smaller spot size increases the temperature changes and consequently yields a higher signal. This often allows for measurements with wider frequency range. However, care must be taken into account when small laser spots are used as they can induce large errors if not measured correctly. Furthermore, a smaller spot size can increase the local temperature rise, so the total power should be managed in order to avoid sample damage or make

measurements at undesired elevated temperatures. Temperature rises can be estimated beforehand or the results can be checked to ensure they are not dependent on laser power.

Although in-plane thermal conductivity of some materials have been measured, the required increase in sensitivity to radial transport was achieved using different spot sizes [42]. This technique, despite being experimentally possible, requires the realignment of the optics every time the spot size is changed and might affect the accuracy of the measurements.

In order to compare the sensitivity of FDTR measurements to different thermal model parameters with the phase noise of the measurements, the phase noise has been plotted in Figure 3-6 at three different lock-in time constants. It should be noted that sensitivity plots presented in this work are the sensitivity to 10% change of parameters. Therefore, once phase noise is larger than phase sensitivity of a particular parameter, the accuracy of the values extracted from fits drops down.

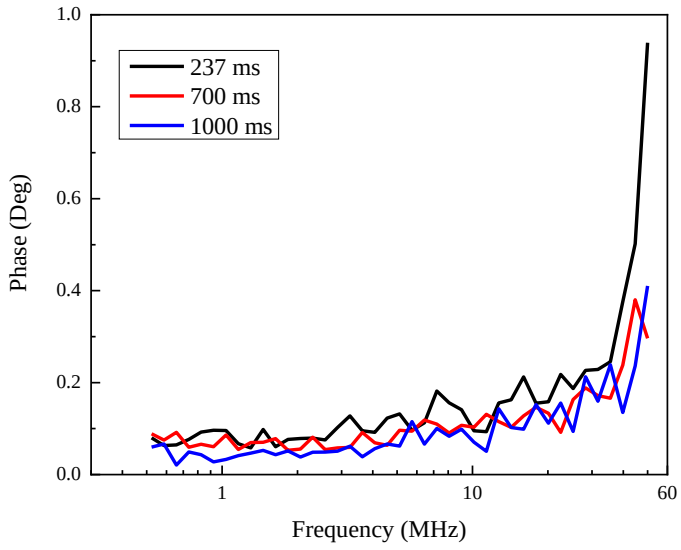

Figure 3-6. Phase noise of FDTR measurement at three different lock-in time constants. The measurement was performed on Al/SiO_2/Si sample. The noise represents the RMS phase variations over 30 measurements at each frequency point with measurement interval of more than the respective time constant.

In order to increase sensitivity to in-plane thermal transport, Feser and Cahill presented a beam offset TDTR method which takes advantage of a lateral offset between pump and probe laser beams to increase the sensitivity to in-plane heat transport [38]. Although anisotropic heat transport is important in 2D materials, there are only a few reports that demonstrate the determination of anisotropic thermal conductivity using FDTR [42, 75, 78, 87].

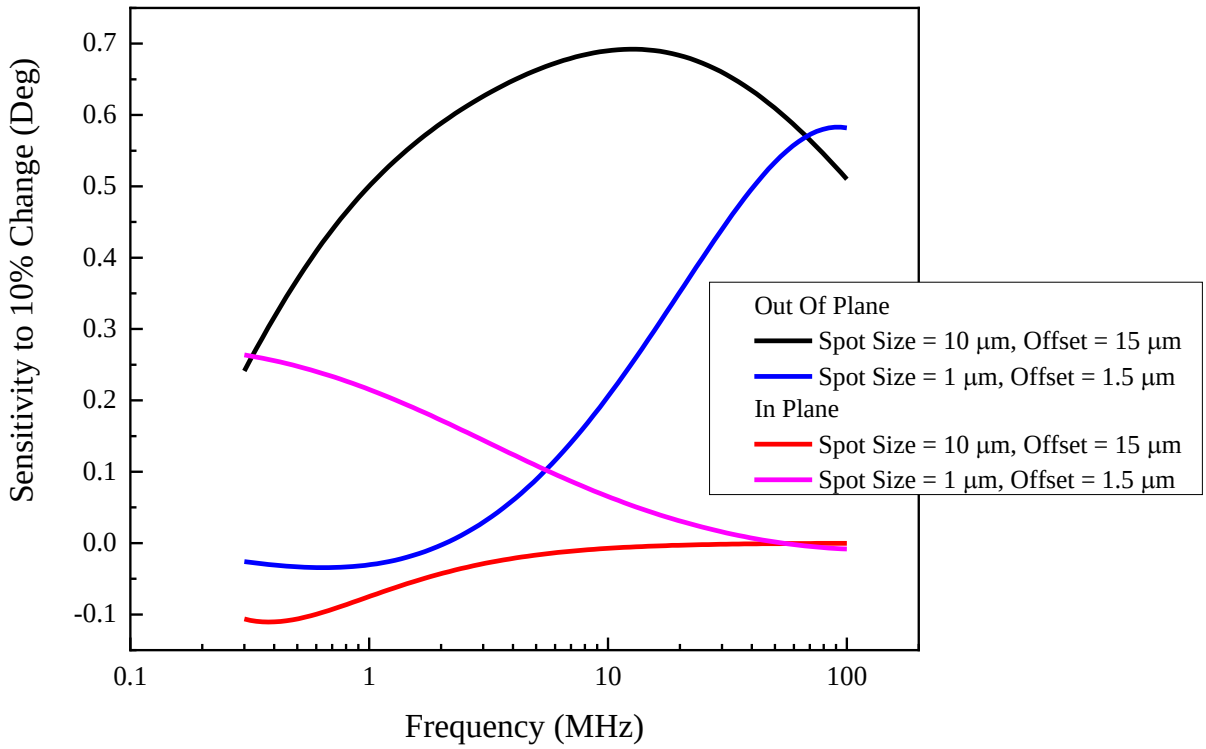

Figure 3-7. Sensitivity to 10% change of thermal conductivity components for two cases of spot size (1 and 10 μm). The offset is set to be 1.5 times the spot size. The system of materials is similar to Figure 3-5b.

By taking advantage of small laser spot sizes, we established a beam-offset FDTR method to measure the in-plane and out-of-plane components of thermal conductivity of anisotropic materials

as well as TBC from a single data set measured at different beam offsets. This does not require any re-alignment of the experimental setup.

3.2.2 Experimental Setup

The schematic of the beam offset FDTR setup is depicted in Figure 3-8a. The setup is similar to our typical FDTR setup (Figure 2-9), with an added Newport TRA12CC actuator to steer an optical window in order to obtain offsets between pump and probe beams (depicted in Figure 3-8b).

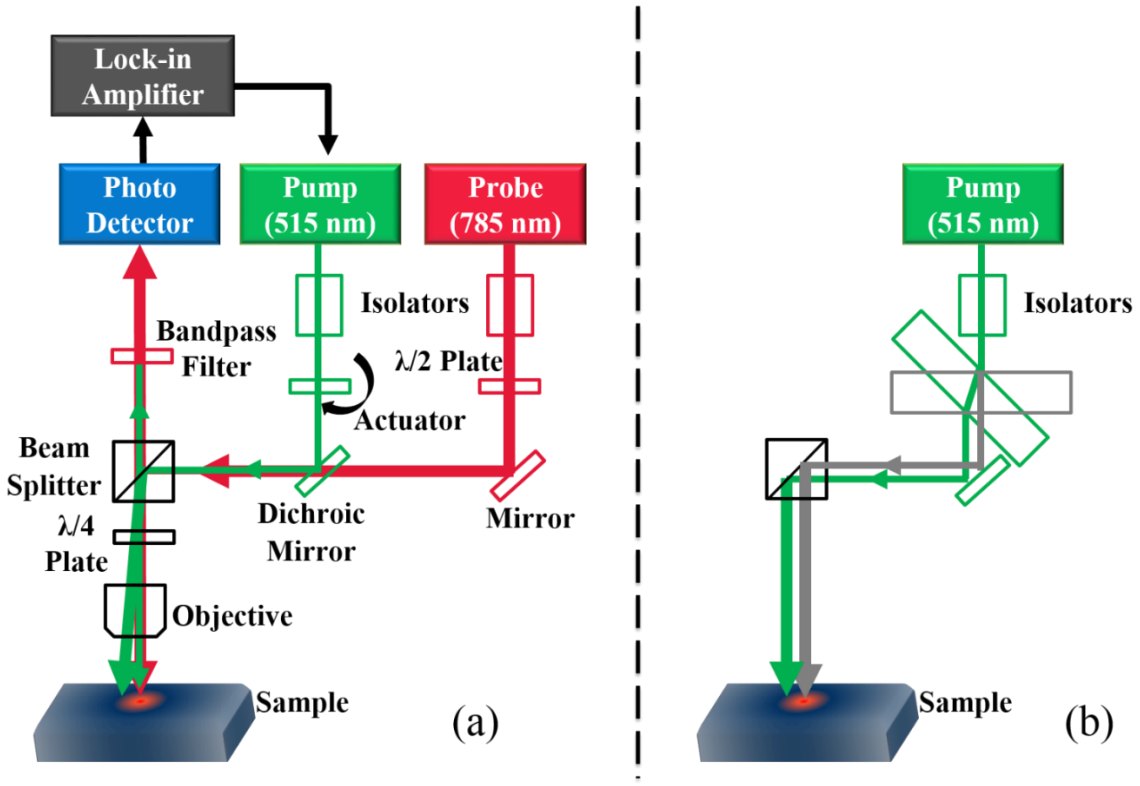

Figure 3-8. (a) Schematic of beam offset FDTR setup. (b) Mechanism of achieving offset by steering an optical window.

3.2.3 Results

In order to show the effectiveness of beam offset FDTR in enhancing the sensitivity to anisotropic thermal transport, a sensitivity analysis is performed by taking the absolute difference in the modeled thermal phase when the parameter of interest is changed by 10%. The sample of interest in this case is Al(50 nm)/Graphite and the parameters investigated are Al/Graphite TBC as well as in-plane and out-of-plane components of thermal conductivity of Graphite. As an example of the literature values reported for graphite, TBC of 50 MW/m^{2}K, out-of-plane thermal conductivity of 6.1 W/mK, and in-plane thermal conductivity of 1983 W/mK have been reported [39].

Figure 3-9 shows the sensitivity of Al/Graphite TBC when the offset between pump and probe beams increases from 0 to 2 μm. The rms spot size in this case is considered to be 1.4 μm. As Figure 3-9 shows, the sensitivity to TBC decreases by increasing the offset.

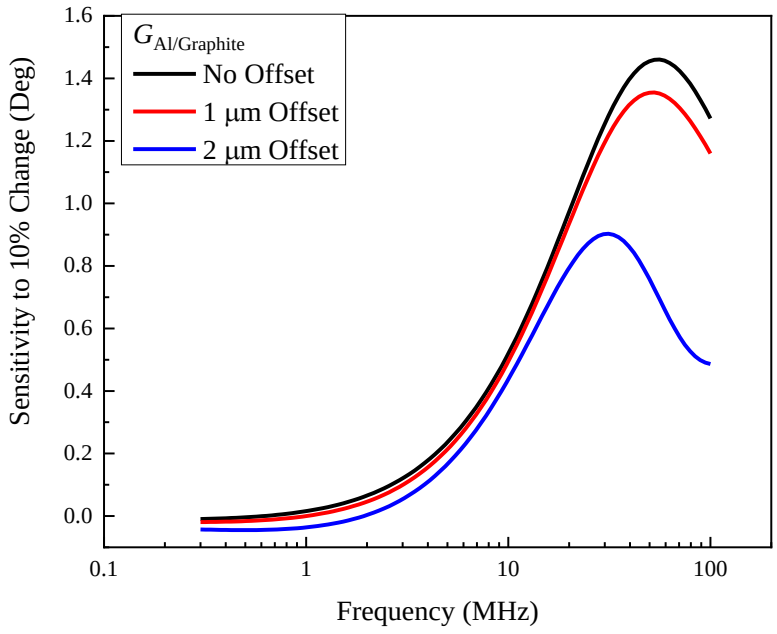

Figure 3-9. Sensitivity of Al/Graphite TBC as a function of beam offset. The rms beam spot size is 1.4 μm.

The sensitivity of Graphite thermal conductivity is depicted in Figure 3-10. In contrary to the sensitivity of Al/Graphite TBC to offset (Figure 3-9), the sensitivity to both in-plane and out-of-plane components of thermal conductivity increases with offset. This enhancement in sensitivity plays a major role in determining the anisotropic thermal conductivity components.

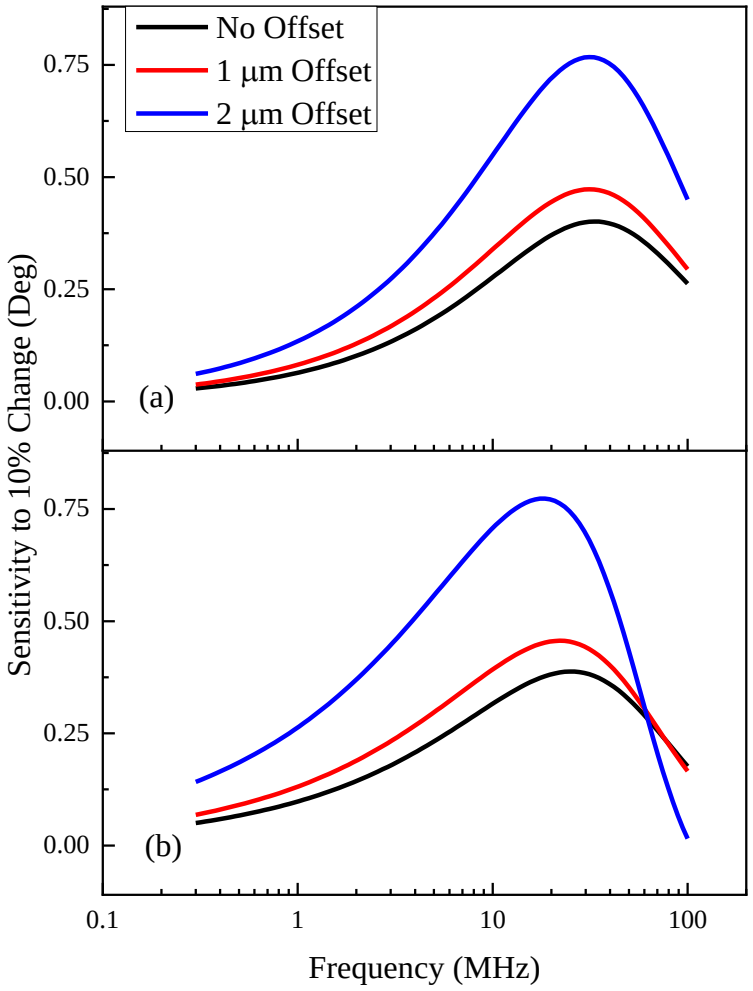

Figure 3-10. Sensitivity of Graphite thermal conductivity as a function of beam offset: (a) out-of-plane component and (b) in-plane component. .

Since the parameters of interest in measurements on transducer-coated bulk crystals are typically the TBC and components of thermal conductivity, a simultaneous measurement of all three parameters can be obtained by performing beam offset FDTR with different offset values if the shape of the sensitivity curves as function of frequency are different enough. This approach was employed to extract the TBC and components of thermal conductivity of an Al/Graphite sample. The sample was measured at four different offset values of 0.8, 1.3, 1.95 and 2.25 μm offset between pump and probe beams. It should be noted that the rms spot size was increased from 1.35 to 1.54 μm as a result of offsetting. The TBC, out-of-plane and in-plane conductivities of 48.6 ± 9.1 MW/m^{2}K, 5.25 ± 2.63 W/mK and 1175.2 ± 416 W/mK were extracted, respectively. The results are in good agreement with those reported in literature [38, 39]. The fit is plotted in Figure 3-11.

Here, it is worth comparing the extracted k_r = 1175.2 ± 416 W/mK with k_r = 1983 W/mK reported in the literature [39]. Schmidt *et al.* measured k_r of graphite with a pump and probe spot sizes of 27 and 5 μm, respectively. By comparing the experimental values of k_r with Boltzmann transport equation calculations through density functional perturbation theory for graphite performed by Fugallo *et al*. [88], we attribute the reduced thermal conductivity to non-diffusive transport in graphite. This phenomenon has been explored in more detail in Chapter 5 for Tungsten Disulfide.

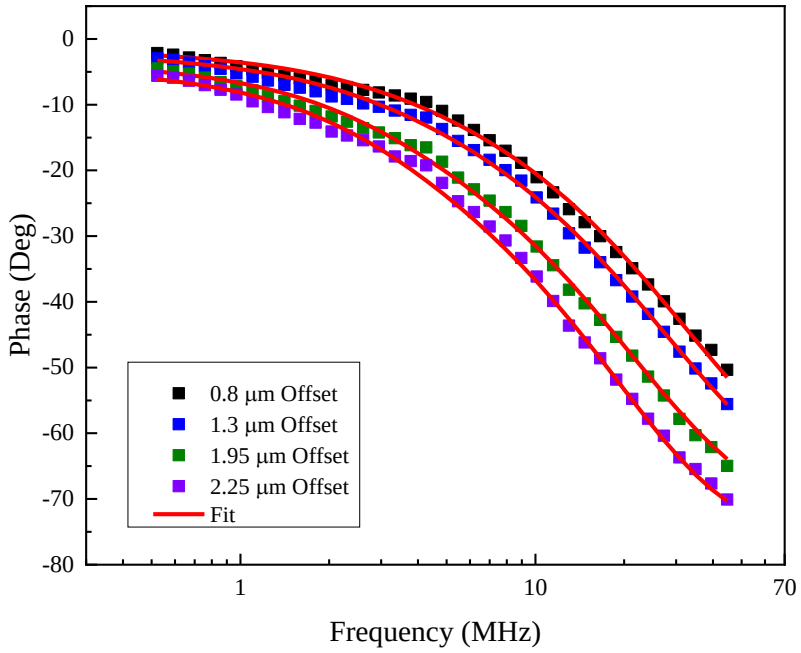

Figure 3-11. Thermal phase measured from Al/Graphite at different offset values (squared symbols) and fit (solid line).

3.3 Frequency Domain Magneto-Optical Kerr Effect (FD-MOKE)

3.3.1 Introduction

As mentioned earlier, rectifying a lack of sensitivity to in-plane thermal transport measurements for some materials (such as 2D materials) using FDTR and TDTR methods requires development of new techniques. Despite in-plane thermal conductivity measurement of some anisotropic materials through thermoreflectance techniques such as beam offsetting [38, 80, 87] and varying spot sizes [39], the experimental sensitivity needs to be further increased to measure the anisotropic thermal conductivity as well as TBC of 2D materials, especially for the case of single and few-layer structures.

Magneto-Optical Kerr Effect has been used in a TDTR setup (TR-MOKE: Time-Resolved Magneto-Optical Kerr Effect) to enhance the sensitivity to in-plane heat transport [89]. In TR-MOKE, a ferromagnetic metal film acts as the transducer to induce changes in the polarization of the reflected probe light as a result of temperature-dependent variations in magnetization (dM/dT) [89], compared to a nonmagnetic metal transducer in FDTR/TDTR which induces temperature-dependent changes in the intensity of the reflected probe light. The temperature-dependent magnetization in TR-MOKE induces changes of polarization of reflected probe beam due to the magneto-optical Kerr effect [89].

An important advantage of MOKE-based methods is that the transducer is much thinner than the transducer in other FDTR/TDTR methods. For instance, a 20 nm thick CoPt multilayer transducer can be used in TR-MOKE [89] compared to 50-100 nm thick nonmagnetic transducers in FDTR/TDTR [78, 79]. As a result of using a thinner transducer, the lateral heat transport in the transducer decreases and the sensitivity to the properties of the underlying layers will be increased due to a smaller thermal mass of the transducer [71]. Additionally, as the signal is based on the temperature changes of the magnetic transducer, using a thin non-opaque transducer is possible and the reflected beams from the layers underneath the transducer does not affect the measurement [89]. This is due to the fact that only the relative changes in the intensity of orthogonally polarized components of the reflected probe beam is detected and the background intensity from the layers underneath the transducer remains constant.

In theory, MOKE can be incorporated in FDTR as well. FDTR is less expensive and easier to set-up compared to TDTR, and the ability to modulate the frequencies over a wider range in FDTR compared to TDTR allows for control over the thermal penetration depth [16, 79, 80]. In what follows, I briefly describe our implementation of Frequency Domain Magneto-Optical Kerr effect

(FD-MOKE), a new approach to quantify the thermal properties of anisotropic materials based on the Kerr effect, yielding enhanced sensitivity to lateral heat transport.

3.3.2 Experimental Setup

A schematic of our FD-MOKE setup is depicted in Figure 3-12. The setup is similar to our beam offset FDTR setup (Figure 3-8), with the following modifications. Non-polarizing optics are used to route the beams in order to avoid affecting the strength of the Kerr signal. A Wollaston prism splits the beam into two orthogonal polarization states, and a half-wave plate balances their intensities before reaching a balanced photodetector.

The optical system is set-up in the polar Kerr configuration for ease of implementation, and this implies that the detected signal is sensitive to changes of the magnetization state of the transducer in the direction perpendicular to the sample surface. In this case which has been adopted in TR-MOKE in the literature [89], transducer materials with perpendicular magnetic anisotropy would be needed to use in the polar Kerr configuration, but this would also complicate sample preparation. For example, perpendicular magnetic anisotropy can be obtained with carefully tuned sub-nm thick M/N multilayers, where M can be Fe, Co or Ni, and N is typically Pd or Pt. We choose simple Nickel thin films as transducer for several reasons. First, Ni is readily available and a thin film with repeatable magnetic characteristics can be easily deposited irrespective of the choice of substrate or film thickness. Since the demagnetizing field of the thin film dominates any other source of magnetic anisotropy, the remanent magnetization will be in-plane. In order to achieve Kerr contrast in the polar geometry, the magnetization needs to be brought out of the plane of the sample, so using Ni, which is a ferromagnet with relatively low magnetization ~500 emu/cc,

requires a relatively weak field of ~6.3 kOe to sufficiently tilt the magnetization out of the plane. Lastly, Ni has a relatively low Curie temperature ~350 C, therefore its magnetization curve as function of temperature will have a comparatively large slope dM/dT near room temperature, aiding in the measurement of the temperature induced changes to the magnetization.

To isolate the thermal phase lag of interest, we perform two measurements of the phase of the signal as function of modulation frequency. We first null the probe signal in the balanced detector by rotating the half-wave plate, then we perform the first measurement while applying a saturating perpendicular field to the sample using an external permanent magnet. This measurement is referred to as $\theta_1(f)$, and it contains the modulation frequency-dependent phase information from the temperature fluctuations in the magnetic layer, reference phase, optical phase, and electrical phase. Since the measurement was preceded by nulling the probe signal at zero applied magnetic field, only the response from the magnetic transducer contributes to the signal, whereas any other contribution such as thermoreflectance from underlying layers is rejected. Another measurement is required to determine the reference phase, and optical and electrical contributions. This measurement is referred to as $\theta_2(f)$, and is performed by detecting the pump beam. Subtracting the two frequency-dependent phases $(\theta_1 - \theta_2)$ yields the desired thermal phase, which is fit to a model based on the diffusive heat equation to extract the thermal properties of interest. Two optical bandpass filters are used to separate the pump and probe beams before the balanced photodetector.

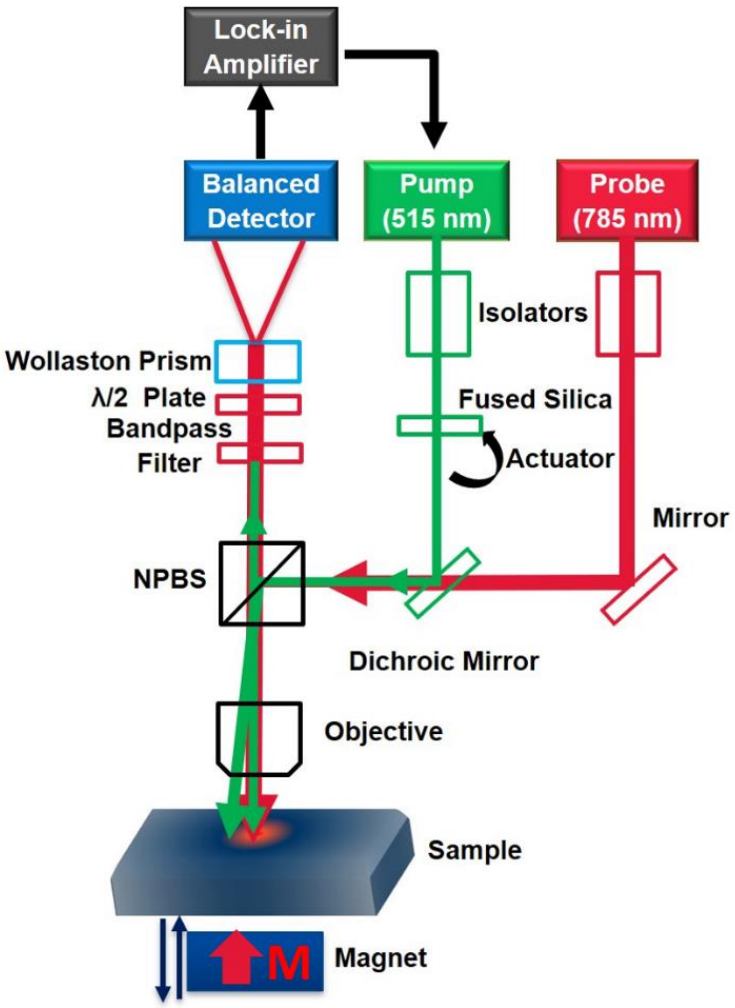

Figure 3-12. Schematic of FD-MOKE setup. NPBS represents non-polarizing beam splitter.

3.3.3 Results

An example result of measurements with FD-MOKE is plotted in Figure 3-13. The sample consists of single layer graphene on SiO_2(300 nm)/Si coated with 20 nm Ni and capped with 3 nm Al to prevent oxidation of the Ni layer. The in-plane thermal conductivity of 636 ± 140 W/mK was measured for graphene [90]. The result is in good agreement with those reported in the literature, for instance 617 W/mK [42]. Furthermore, a 17 ± 0.2 MW/m^2K TBC was measured across

Ni/graphene/SiO_2 [90]. The measured TBC is smaller than those reported in the literature [91, 92], however the reduced TBC can be related to several interface parameters such as the presence of impurities or oxygen.

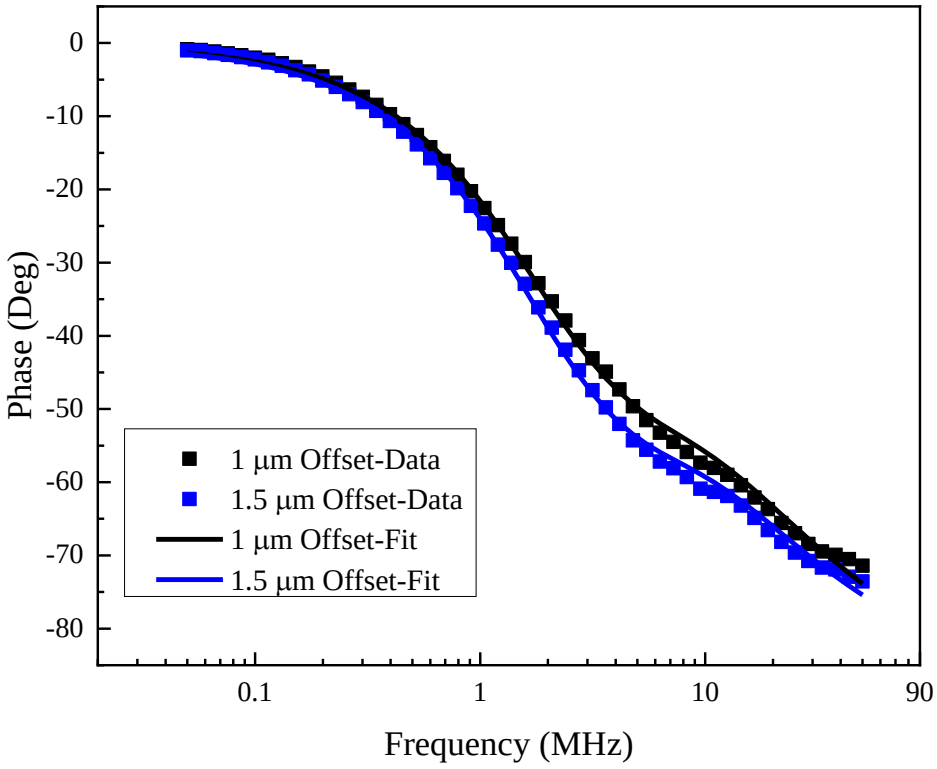

Figure 3-13. Thermal phase measured from Ni/Graphene/SiO_2/Si at different offset values (squared symbols) and fit (solid line)

3.4 High-frequency measurements of thermophysical properties of thin films using a modified broad-band frequency domain thermoreflectance approach

3.4.1 Introduction

As discussed in sections 2.3.3 and 2.3.4, most FDTR measurements are limited to around 20 MHz. At frequencies larger than 20 MHz, the SNR drops significantly due to the decrease of the signal (surface temperature oscillations vary as $f^{1/2}$ for the 1D case) and increase in noise (mostly coherent RF noise picked up by the electrical cables). Figure 2-11 shows the amplitude of the thermal signal and noise in a typical FDTR measurement, where the SNR rapidly drops above 10 MHz. To overcome this limitation, BB-FDTR implemented by Regner and co-workers (discussed in section 2.3.4 and depicted in Figure 3-14a) was used to increase the pump modulation frequency up to 200 MHz [16] and to determine the contribution of phonons with different MFPs to the thermal conductivity in different metallic and non-metallic materials [14, 93, 94].

In the original implementation of BB-FDTR by Regner and co-workers, two EOMs was used: one after the pump laser and the other one before the detector to heterodyne the probe beam. They proposed an alternative placement for the heterodyning EOM: on the probe path before the sample, in a similar way as the pump beam EOM. However, in this case, they did not propose a method to recover the thermal phase of interest from the unwanted instrumental contributions to the measured phase. Herein, we resolve this issue by presenting two different techniques to perform BB-FDTR measurements beyond 100 MHz, the so-called differential broadband frequency domain thermoreflectance (DBB-FDTR). Since the laser beams are modulated before the sample, both methods eliminate the use of expensive EOMs altogether, by using analog modulated pump and probe lasers. We recover the thermal phase of interest through a differential approach. Measuring

a differential thermal phase by either varying the spot size or offsetting the pump and probe beams, the thermophysical properties of materials can be extracted. This approach enables the study of nanoscale heat transport where non-equilibrium phenomena are dominating.

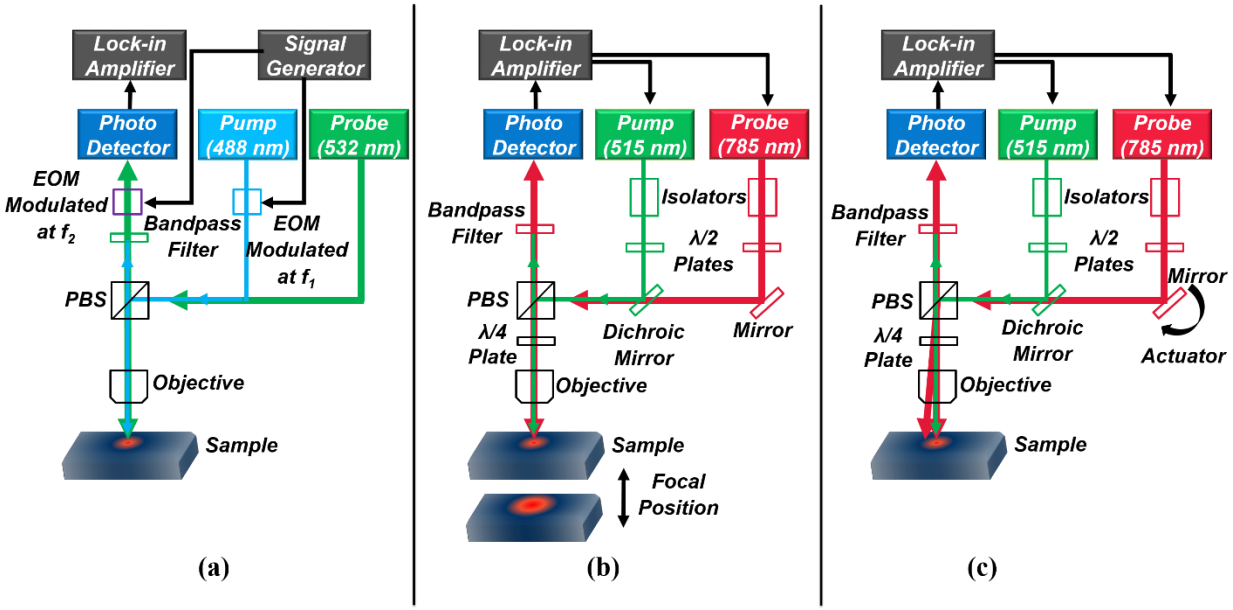

Figure 3-14. (a) Regner's BB-FDTR configuration. (b) DBB-FDTR configuration described in this work based on changing the focal point, and (c) based on changing the offset between pump and probe.

3.4.2 DBB-FDTR Implementation

Schematics for two approaches of the differential BB-FDTR (DBB-FDTR) setup are shown in Figure 3-14b and Figure 3-14c. A two-channel function generator (Anritsu-MG3740A) is used to modulate the intensities of the pump and probe lasers (Omicron A350 operating at 515 nm and 785 nm) at f_1 and f_2, respectively. The rest of the setup is similar to FDTR setup described in section 3.1. The surface temperature of the sample oscillates at the frequency of pump (i.e. f_1), as

the pump light is absorbed on the transducer. The probe laser operating at frequency f_2 samples the temperature response from the transducer by thermoreflectance, i.e. changes of reflectivity due to the surface temperature. The heterodyne frequencies of $f_1 \pm f_2$ generated on the surface of the sample by mixing the pump and probe signals are then measured by a photodetector (Thorlabs PDA8A). We note that the photodetector's 50 MHz bandwidth is not necessary for DBB-FDTR, as we typically measure the low-frequency heterodyne component where the noise is at a minimum and limited by the detector. A lock-in amplifier (Zurich Instruments HF2LI) locked at the frequency $f_1 - f_2$ is used to demodulate the signal. We note that a high-frequency lock-in amplifier is not necessary to implement DBB-FDTR.

As discussed in section 3.1, the phase measured at the lock-in amplifier has contributions from the thermal, optical and electrical phases with respect to a reference phase from the signal generator, i.e. $\theta_1 = \theta_{Thermal} + \theta_{Optical} + \theta_{Electrical} + \theta_{ref}$. Typically in FDTR and BB-FDTR, after performing the thermal measurement θ_1 (a measurement that includes the thermal phase lag of interest) a non-thermal measurement θ_2 is used to recover the thermal phase of interest from other unwanted phases; i.e. $\theta_2 = \theta_{Optical} + \theta_{Electrical} + \theta_{ref}$. Therefore $\theta_1 - \theta_2 = \theta_{Thermal}$. The non-thermal measurement is typically achieved by replacing a filter in front of the detector in order to measure the modulated pump, rather than the probe. This approach is not viable when the pump and probe are directly modulated (as we do here), as the pump is not heterodyned and there is no signal at $f_1 - f_2$ for the measurement θ_2. This was reviewed in section 3.4.1.

In the DBB-FDTR presented here, after performing the first thermal measurement ($\theta_1 = \theta_{1,Thermal} + \theta_{1,Optical} + \theta_{1,Electrical} + \theta_{1,ref}$), another thermal measurements is performed either at a

different focal point (using a Thorlabs KPZNFL5 piezo translational stage, depicted in Figure 3-14b), or on the same focal point but with an offset between the pump and probe beams (using a Newport TRA12CC actuator, depicted in Figure 3-14c). In this case, $\theta_2 = \theta_{2,Thermal} + \theta_{2,Optical} + \theta_{2,Electrical} + \theta_{2,ref}$. Key to our approach is to perform two thermal measurements that yield a sufficiently different thermal response, but otherwise have identical instrumental phases. Subtracting these two thermal measurements gives a differential thermal phase (DTP) that can be analyzed to extract the thermal parameters of interest.

As it will be shown later, accurate knowledge of the pump and probe spot sizes or the offset between the pump and probe spots is important to reduce errors. To this end, the spot sizes are measured locally every time a DBB-FDTR measurement is made. We measure the spot sizes by analyzing the convoluted response obtained by scanning the relative offset between the Gaussian pump and probe beams [38]. These measurements are performed at 43 MHz to minimize the effects of in-plane thermal transport on the measured profile, and further increasing the modulation frequency has no effect on the spot size obtained. The results obtained in this way have been checked with a razor profiler for consistency.

In focal DBB-FDTR (Figure 3-14b), two thermal measurements are performed in the same frequency range at two different focal positions. Any frequency-dependent variation to the electrical phase is common between the measurements performed at the two focal points, since the frequency range is identical, and therefore $\theta_{1,Electrical} = \theta_{2,Electrical}$. Moreover, since the beams are modulated with the same source, $\theta_{1,ref} = \theta_{2,ref}$. The optical phase shift for each beam travelling in free space is $\theta = kd$, where d is the distance travelled and k is the modulation wavenumber, so the optical phase shift difference between pump ($\theta_P = k_P d$) and probe ($\theta_S = k_S d$) is $\frac{2\pi}{c}\left(f_P - f_S\right)d$

, where f_P and f_S are frequencies of modulation for pump and probe beams. By choosing a heterodyne frequency of 100 kHz and given that the sample is typically defocused by shifting it over a distance of 7 μm, the optical phase difference is $\sim 10^{-8}$ deg . Therefore, $\theta_{1,Optical} - \theta_{2,Optical} \sim 0$, and the Differential Thermal Phase (DTP) then can be extracted by calculating $\theta_1 - \theta_2 = \theta_{1,Thermal} - \theta_{2,Thermal}$.

By fitting the difference in the solutions of the diffusive heat equation calculated at the two focal points to the measured DTP, the unknown thermophysical properties can be extracted. The method to determine the thermal properties from thermoreflectance measurements was reviewed in section 2.5.

3.4.3 Samples Considered and Sensitivity Analysis

Three different samples have been studied in this work to demonstrate DBB-FDTR. The samples were prepared by sputter deposition of Al thin films on various substrates. Sample 1 consists of Al(59nm)/SiO_2(150nm)/Si, sample 2 is Al(59nm)/Si and sample 3 is Al(59nm)/MgO. The thickness of the layers was determined by X-Ray reflectivity and the in-plane thermal conductivity of the Al transducers were determined by 4-point probe electrical conductivity and applying the Wiedemann-Franz Law. The thermophysical parameters of the samples are listed in Table 3-2. The values for the out-of-plane thermal conductivity and volumetric heat capacity were taken from the literature.

Table 3-2. Thermophysical properties of the samples studied in this work. The values for the in-plane thermal conductivity of Al and film thickness are specific to our samples, all other values in the table are taken from the literature.

	k_z (W/mK)	k_r (W/mK)	C (MJ/m^{3}K)	t (nm)
Al	173	173	2.42	59
SiO_2	1.32	1.32	1.59	150
Si	145	145	1.64	Semi-infinite
MgO	Determined by Fit	Determined by Fit	3.37	Semi-infinite

In order to investigate how sensitive the thermal phase is to different parameters, a sensitivity analysis is performed. The definition typically used for the sensitivity is the logarithmic derivative of the phase with respect to the changes of a given parameter [16]. Here we prefer to calculate the absolute difference in the thermal phase when the parameter of interest is changed by 10%. This definition leads to a direct insight into whether a quantity is measurable or not by comparing the phase sensitivity to the typical phase noise of the measurement.

Figure 3-15a and Figure 3-15b show the sensitivity analysis and the modeled DTP for Al/SiO_2/Si for focal DBB-FDTR. The modeled DTP is highly dependent on the spot sizes used in the focal DBB-FDTR configuration. The DTP increases by increasing the difference between the first and the second measurement's rms spot sizes, however one should note that the thermal signal magnitude decreases at larger spot sizes due to the reduction in surface temperature oscillations.

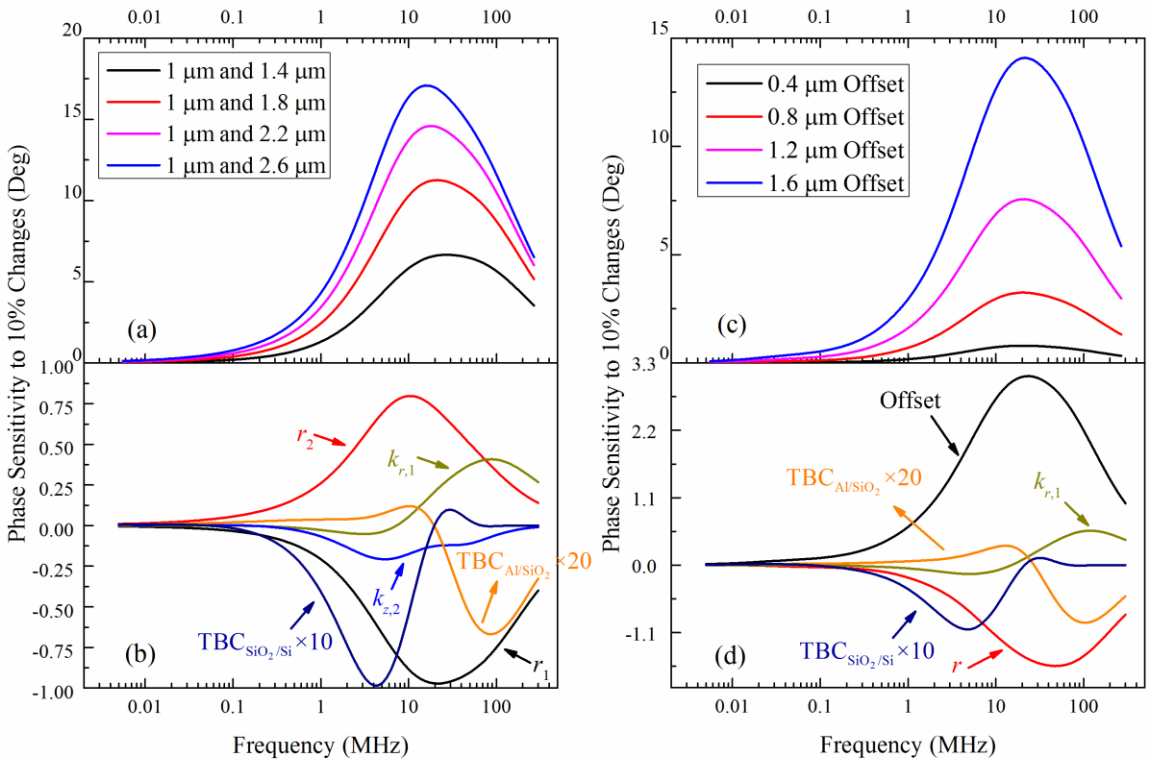

Figure 3-15. Modeled response of DBB-FDTR signals. For all the curves above, the sample is Al(59)/SiO_2(150)/Si. (a) Modeled DTP in focal DBB-FDTR for different pairs of rms spot sizes. The larger the amount of defocus, the larger is the resulting rms spot size, though the associated signal will be lower. (b) Sensitivity of DTP with respect to 10% changes in different parameters. r_1 and r_2 are the rms value of pump and probe spot sizes at two focal positions. $k_{r,1}$ is the radial thermal conductivity in the Al layer, TBC is the thermal boundary conductance, and $k_{z,2}$ is the perpendicular thermal conductivity of SiO_2. (c) Modeled DTP in offset DBB-FDTR for different pump-probe beam offset values. (d) Sensitivity of DTP with respect to 10% changes in different parameters. r and Offset are the rms value of pump and probe spot sizes, and the offset between pump and probe beams, respectively.

Figure 3-15c and Figure 3-15d show the sensitivity analysis and the modeled DTP for Al/SiO_2/Si for offset DBB-FDTR. Similar to the case for focal DBB-FDTR, the DTP obtained by offset DBB-FDTR increases with increasing the offset between the pump and the probe beams. However, the thermal signal magnitude decreases by increasing the offset. Figure 3-15 shows that both focal and

offset DBB-FDTR methods show phase sensitivity to important parameters of the particular sample of study ($Al/SiO_2/Si$). However, offset DBB-FDTR is more favorable when anisotropic heat transport is important [38, 80].

3.4.4 Results

Figure 3-16a shows the DTP for $Al/SiO_2/Si$ measured by focal DBB-FDTR. The in situ measured rms spot sizes are 1.45 μm and 2.3 μm for the first and for the second focal positions, respectively. The fit resulted in the Al/SiO_2 thermal boundary conductance (TBC) of 87.6 ± 15 MW/m^2K and SiO_2/Si TBC of 28.2 ± 2.25 MW/m^2K, which are consistent with values reported previously [95-97]. Using focal DBB-FDTR, the TBC of the Al/Si sample has been measured to be 192.5 ± 10 MW/m^2K (Figure 3-16b), which is in agreement with the values reported in the literature [15, 98]. Focal DBB-FDTR was used to measure the TBC of Al/MgO as well as the thermal conductivity of MgO. Figure 3-16c shows the obtained fit and the measured DTP which resulted in Al/MgO TBC of 163.8 ± 9.95 MW/m^2K and k_{MgO} of 55.3 ± 11.2 W/mK. The results are consistent with the values reported in the literature [99].

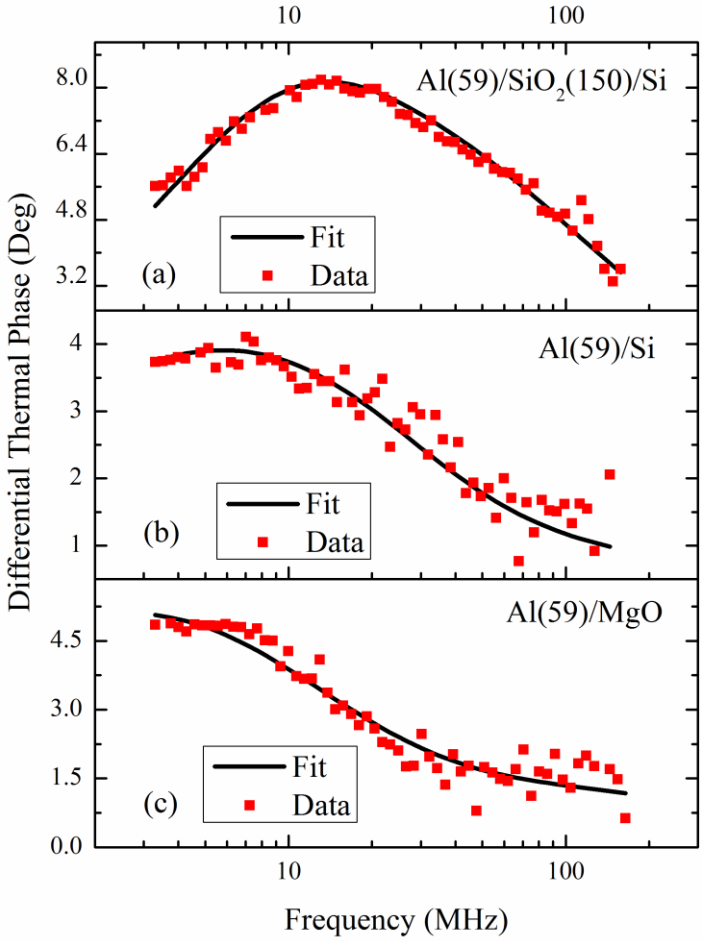

Figure 3-16. Measured DTP (squares) and the obtained fit (lines) for (a) Al/SiO₂/Si, (b) Al/Si, and (c) Al/MgO, obtained by focal DBB-FDTR.

Moreover, the results for offset DBB-FDTR with 1.5 μm pump-probe offset for Al/SiO₂/Si indicated TBCs of 63.2 ± 26 MW/m^{2}K for Al/SiO₂ and 33.3 ± 10.6 MW/m^{2}K for SiO₂/Si (Figure 3-17a) which are consistent with the results obtained from focal DBB-FDTR.

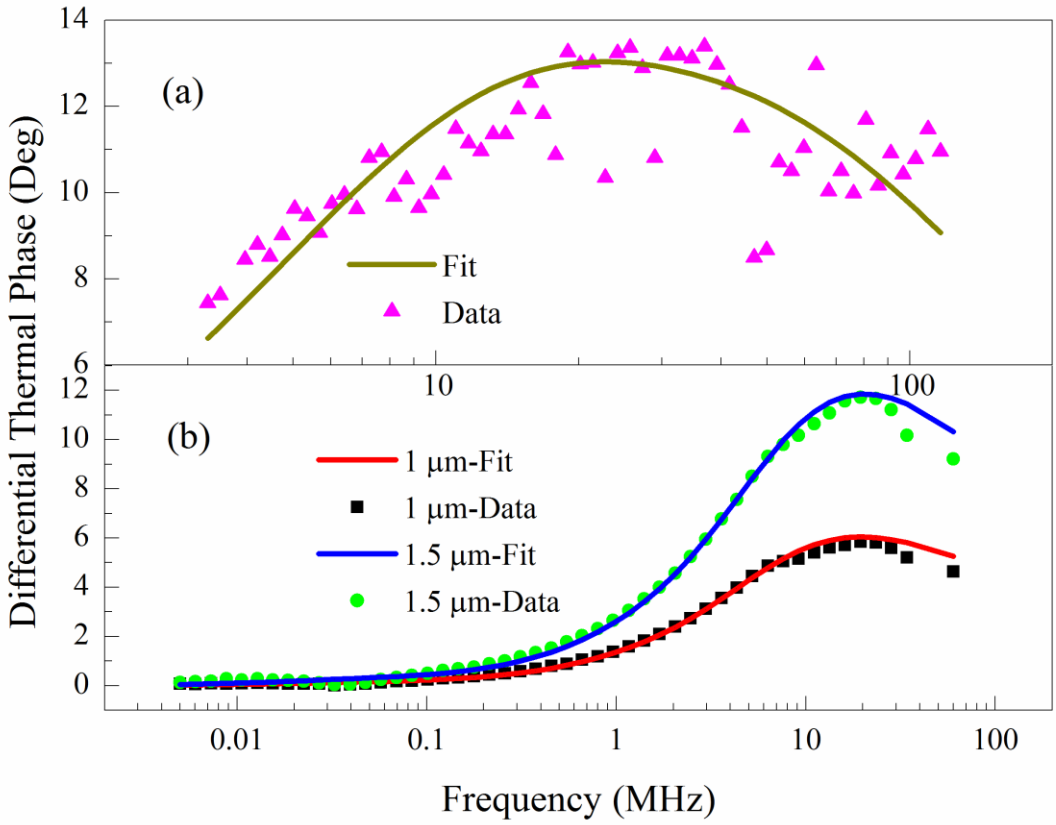

Figure 3-17. (a) Measured DTP (triangles) and the obtained fit (line) for Al/SiO_2/Si by offset DBB-FDTR with 1.5 μm pump-probe offset. (b) Measured DTPs (symbols) and the obtained fits (lines) in offset differential FDTR for the same sample, obtained at two different pump and probe offsets.

By comparing the results of focal and offset DBB-FDTR on the Al/SiO_2/Si sample (Figure 3-16a and Figure 3-17a), one can see that the results obtained from the focal DBB-FDTR measurement are considerably more accurate and less noisy than those obtained by the offset DBB-FDTR. We attribute the inaccuracy in the offset DBB-FDTR measurement to the limited repeatability of the actuator that determines the offset between pump and probe beams. Due to the randomness in the

reference phase obtained from the analog signal generator every time a new frequency is set, the thermal phase at each frequency is measured at two different offset points, then the frequency is changed (rather than making a full measurement as a function of frequency at the first offset point, then making the next full measurement as a function of frequency at the second offset point). Therefore, the actuator is activated twice at each frequency point to take two measurements at different offset values. Our calibration showed that to obtain a 1 μm offset between the pump and probe beams, the actuator needs to be moved by 6 μm, while the repeatability of the actuator is limited to ±0.5 μm. In order to show the effectiveness of the offset DBB-FDTR technique while minimizing the error introduced by the limited repeatability of the actuator, two thermal FDTR measurements (without heterodyning) at two different offset values were performed up to 50 MHz. Since these measurements used the lock-in amplifier as signal source, each FDTR curve as function of frequency was measured separately, and the actuator was used only once. By subtracting the two phases measured, the instrumental contributions to the recorded phase were canceled (as described in DBB-FDTR Implementation section). Figure 3-17b shows the DTP measured for Al/SiO_2/Si and the obtained fits for two different offset values. This resulted in fitted SiO_2/Si TBC values of 29.8 ± 4.5 MW/m^2K and 30 ± 4.2 MW/m^2K for 1 μm and 1.5 μm offsets, respectively; which are consistent with those obtained from DBB-FDTR. However, for the measurements of Figure 3-17b, the sensitivity to Al/SiO_2 TBC is too small within the frequency range measured with FDTR, and a high-frequency approach such as DBB-FDTR is necessary (see Figure 3-15d). By comparing the results obtained from offset DBB-FDTR and offset differential FDTR (Figure 3-17a and Figure 3-17b, respectively), one can see that the repeatability issues of the actuator have been eliminated.

Both focal and offset DBB-FDTR approaches are capable of identifying thermophysical properties at sub-micron length scales. This is achieved by the reduction of spot size and by decreasing the thermal penetration depth of heat carriers through increasing the frequency range of thermoreflectance measurements. Any frequency dependence in the thermophysical parameters originating from non-diffusive heat transport can be studied using such high-frequency systems [97]. An example was presented by Regner and co-workers who showed frequency dependence (i.e. heat carrier mean free path spectra) of thermal conductivity of Si [14, 16]. The interpretation of these results however depends on knowledge of non-diffusive heat conduction mechanisms [94, 100], and is a subject worthy of study, as it closely relates to how heat is transported in nanoscale systems. The samples studied in this work were not susceptible to the observation of frequency dependence in the thermal conductivity, as described below.

Firstly, we used Al transducers, and given the high electron-phonon coupling in Al, it is safe to neglect electron and phonon non-equilibrium effects within the transducer [100, 101]. For the Al/SiO_2/Si sample, the thick SiO_2 layer prevents the heat from reaching the Si layer, and given the disordered amorphous structure of SiO_2, only phonons of MFP ~1 nm are expected to contribute to its overall thermal conductivity [102]. Therefore, since the MFP in SiO_2 are much smaller than the shortest thermal penetration depth and spot size used in this experiment (~40 nm and ~1 μm, respectively), only diffusive transport is expected, yielding bulk-like thermophysical properties. For the Al/Si sample, the presence of the native <10 nm oxide layer causes the phonon spectral heat flux injected in the Si layer to be filtered in such a way that the apparent thermal conductivity of Si matches that of the bulk [103]. This is opposite to the work of Wilson and Cahill, where the oxide layer was removed, allowing for the full phonon spectrum to penetrate the Si substrate and yielding a frequency and spot size dependence to the apparent thermal conductivity data [100].

In the case of the MgO sample, the high modulation frequencies used in this work lead to thermal penetration depths as low as 200 nm. This, as well as the small spot sizes used, may lead to non-diffusive transport that manifests itself through an apparent thermal conductivity that is lower than the expected value. Wilson and Cahill report a lower apparent thermal conductivity for the Al/MgO system with spot sizes of ~1 μm, and calculate a thermal conductivity accumulation function for MgO yielding ~75% of the bulk conductivity for phonon MFP up to ~300 nm [104]. We have calculated the thermal conductivity accumulation function of MgO from first principles (more on this in the next section) and find that, contrary to ref. [104], phonons with MFP of ~200 nm contribute >90% of the thermal conductivity (see section 3.4.5: Thermal Conductivity Accumulation Functions). This indicates that at our experimental modulation frequencies we may be at the cusp of detecting non-diffusive transport in this system. Given that a diffusive model does not fit our experimental data very closely, a non-diffusive model may be needed to assess non-diffusive transport in this case, but this is out of the scope of this work. The data by Wilson and Cahill indicates that the non-diffusive effects in Al/MgO are much weaker than those in Al/Si [104].

3.4.5 Thermal Conductivity Accumulation Functions

The thermal conductivity accumulation functions of Si and MgO were calculated through the Boltzmann transport equation using phonon dispersions and scattering rates obtained by *ab initio* density functional theory (DFT).

The phonon interatomic force constants are calculated through Quantum Espresso [105] using the projector augmented-wave (PAW) method using Perdew-Burke-Ernzerhof pseudopotentials. The

crystals were modeled starting from the relaxed lattice constants [106] using a 10x10x10 Monkhorst-Pack wavevector grid. The wavefunction kinetic energy cut-off value was checked by monitoring the convergence of the system's total energy. Coulomb interactions were taken into account by computing Born effective charges. The second-order force constants were extracted using the package Phonopy [107]. Third-order force constants were extracted with a 3x3x3 supercell using the package Thirdorder [108]. Finally, the thermal conductivity accumulation functions are calculated via the almaBTE package [109] using a 24x24x24 wavevector grid, which includes energy and wavevector specific scattering rates and isotopic scattering.

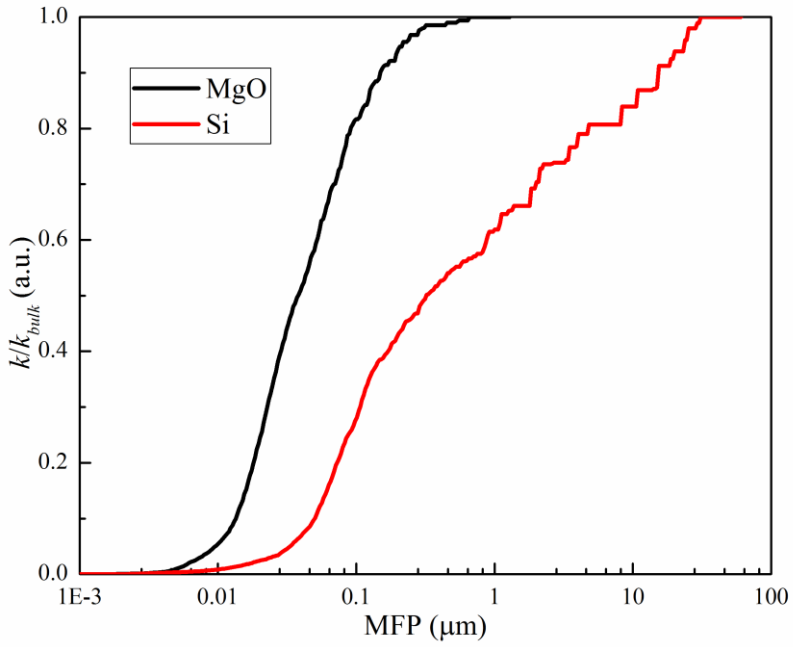

Figure 3-18. Thermal conductivity accumulation as function of phonon mean free path calculated via DFT.

The results for Si and MgO are shown in Figure 3-18. The accumulation for Si follows closely the dependence previously reported [110]. The accumulation for MgO shows a faster saturation at lower phonon mean free paths as compared to the curve reported in ref. [104], but we note that one source for the difference is that the calculation reported here uses phonon scattering rates determined from first principles calculations, whereas in ref. [104] phonon scattering rates are modeled analytically through a frequency-dependent power law.

3.5 Conclusion

In this chapter, implementation of FDTR method along with a sample result was presented. An economical extension of FDTR to higher frequencies was then shown by a mathematical approach to increase SNR. To increase the sensitivity to anisotropic transport, two methods of beam offset FDTR and and FD-MOKE were described and their results were presented. Finally, two methods to extend FDTR were proposed to perform high frequency measurements of the thermophysical properties of submicron films using DBB-FDTR method. Both methods eliminate the need to use expensive electro-optic modulators.

Chapter 4: Non-diffusive transport and anisotropic thermal conductivity in high-density Pt/Co superlattices

Despite the numerous reports over the last two decades dedicated to the study of interfacial thermal transport, the physics of thermal transport across nanoscale metallic multilayers is less explored. This is in part due to the relatively high conductance characteristic of these interfaces, which renders them difficult to characterize. Interfacial transport in these systems has so far appeared to be diffusive, a surprising behavior as the interface density increases and the layer thicknesses become comparable with mean free path of electrons. To address the limit of diffusive theories describing heat transport across high density metallic interfaces, we investigate heat transport in and across Pt/Co multilayers systematically via frequency domain thermoreflectance. Through a combination of laser beam offset and small laser spot size to gain sensitivity to radial heat transport, the anisotropic thermal conductivity of the multilayers is measured. By changing the number of interfaces while keeping the overall thickness of Pt and Co layers constant, the effect of interface density on the effective thermal conductivity of the multilayers is studied. The extracted thermal boundary conductance of Pt/Co interface is then compared with calculations from the electronic diffuse mismatch model and experimental data available in the literature. We show that as the period thickness of the multilayers becomes much smaller than the mean free path of the electrons, a marked deviation is observed from the diffusive transport theory. We attribute this deviation to the non-diffusive nature of heat transport in sub-nanometric scales at interface densities above 1/nm.

4.1 Introduction

Metallic multilayers have attracted a substantial amount of attention due to their impact in fields such as magnetic memory [111, 112] and spintronics [112-115] as well as their high mechanical strength at the nanometric scale [116-118]. For instance, multilayers of Pt/Co are a way to create materials with perpendicular magnetic anisotropy used in current-controlled magnetization [119]. Thanks to the high electrical conductivity at metallic interfaces, the thermal transport in metallic multilayers is often more efficient compared to metal/dielectric multilayers, such as Mo/Si multilayers used in extreme ultraviolet and soft X-ray optics [86], in which phonon-mediated transport dominates. In spite of this, the thermal resistance across metallic multilayers is still an important barrier against heat transfer, particularly when a high interface density between the heat source and the heat sink limits heat dissipation. This heat transport hindrance can, for instance, compromise the thermal stability of spintronic devices [112]. So far, little work has been done on heat transport in nanometric and sub-nanometer metallic multilayers, where the electron mean free path Λ approaches or exceeds the layer thickness and heat transport deviates from the diffusive Fourier regime [8].

Heat transport takes place anisotropically in multilayers and heat is carried in-plane more readily compared to out-of-plane [86]. This is mainly due to the increased resistance in the out-of-plane direction originating from the presence of the interfaces. Although recent advances in optical metrology techniques have enabled researchers to study heat transport across different interfaces [16, 83], most of the studies so far have focused on metal/non-metal or non-metal/non-metal structures. Gundrum *et al*. measured the room temperature thermal boundary conductance (G) of

[8] It should be noted that when the mean free path is larger than the layer thickness, scattering mechanisms such as boundary scattering become more dominant.

the Al/Cu interface to be ~4 GW/m^{2}K, which is an order of magnitude larger than interfaces with phonon-mediated transport [59]. Wilson and Cahill measured the effective thermal conductivity of Pd/Ir multilayers and extracted a value for *G* of 14 ± 3 GW/m^{2}K, the highest value reported so far [60]. Cheaito *et al*. extracted $G_{Cu/Nb}$ ~ 4.7 GW/m^{2}K [61], and by comparing the results presented for Al/Cu [59] and Pd/Ir [60] interfaces to Cu/Nb interfaces, they demonstrated that *G* is dominated by the temperature derivative of the electron energy flux, and less influenced by the transmission probability given by the interfacial mismatch in electronic properties [61]. This is unlike phonon-mediated interfaces in which *G* is more dependent on interfacial phonon mismatch.

Measuring *G* in metallic and highly conductive interfaces requires high measurement sensitivity due to its low contribution to the overall thermal resistance of the system, therefore studies have generally concentrated on samples having hundreds of interfaces or have been able to provide only a lower bound value for *G*. In this regard, lower bounds of 8 GW/m^{2}K and 5 GW/m^{2}K have been reported for *G* in Pt/Co [120] and Pt/Au [121] interfaces, respectively.

To quantify electron-mediated heat transport at metallic interfaces, an electronic extension to the commonly used diffuse mismatch model (DMM) used to describe phonon-mediated transport has been successfully employed [122]. The electronic DMM (EDMM), introduced by Gundrum *et al*. [59] considers diffuse interface scattering, a degenerate metal with an isotropic Fermi surface and temperature-independent density of states. The resulting relation to describe *G* is a function of the electronic heat capacity and Fermi velocities of the metals adjacent the interface and does not depend on layer thickness.

To the best of our knowledge, there is no evidence in the literature that *G* in metallic multilayers is affected by non-diffusive transport or deviates from the EDMM theory. Previous work has highlighted that diffuse scattering at metal interfaces seems to be an assumption that holds in light

of the experimental observations [59, 60], and that for layer thickness as low as $\sim \Lambda / 3$ the transport is consistent with Fourier's law [60, 123]. In other words, if transport at metal interfaces can be treated as diffusive even when the constituent layer thickness are so small, then the effective thermal resistance across the structure will simply be given by the sum of the layer thermal resistance and the interface resistance. This appears to be in contradiction of other instances where diffusive thermal transport break down, as it does for example when the apparent thermal conductivity of a thin semiconductor slab is reduced with respect to its bulk value when its thickness becomes comparable to the phonon mean free path [124]. As for metal multilayers, two reasons why transport would be characterized as diffusive even when interfaces are closer than Λ are that (1) the interfaces may induce mostly elastic scattering, or that (2) interface scattering does not alter the electronic energy for its distribution to deviate significantly from equilibrium. This raises several questions: when does the assumption of diffusive interface scattering break down so that *G* is no longer constant as the interface density increases? Would one observe a minimum in the effective thermal conductivity in metallic multilayers? [125] In this work, the anisotropic thermal conductivity of Pt/Co multilayers is measured at room temperature with interface densities approaching 2/nm (about one order of magnitude below Λ of 7-10 nm for Pt [120] and 5-12 nm for Co [123, 126]). The value for *G* of Pt/Co is then extracted and compared with expectations from the EDMM [59]. We show that as the interface density increases a deviation from the model is observed, and attribute this deviation to non-diffusive transport at sub-nanometric scales.

4.2 Experimental Setup, Sample Preparation and Sensitivity Analysis

The anisotropic thermal properties of the multilayers are measured by frequency domain thermoreflectance (FDTR) [79]. To increase the sensitivity to the in-plane component of the

thermal conductivity, a beam-offset approach was utilized [80]. The schematic of the FDTR setup is shown in Figure 3-8a [79, 80]. Briefly, a continuous-wave laser (Omicron A350 operating at 515 nm) is intensity modulated using a lock-in amplifier (Zurich Instruments HF2LI) over a range of frequencies up to ~20 MHz. This pump laser absorbs on the sample surface and introduces heat flux at the desired modulation frequency. Another continuous-wave laser (Omicron A350 operating at 785 nm) then probes the resulting temperature fluctuations of the sample surface through changes in temperature-dependent reflectivity. The reflected light is then collected using a photodetector (Thorlabs PDA8A) and demodulated using the lock-in amplifier. By introducing a laser beam offset between pump and probe (1.25 μm at the sample surface) and small laser spot size (typically 1.4 μm $1/e^2$ diameter), the signal magnitude and the sensitivity to in-plane thermal transport is improved. The resulting thermal phase spectrum is then fitted to a solution of the diffusive heat equation where the unknown thermophysical properties can be extracted. It may be counterintuitive to use a diffusive model for data analysis in cases where non-diffusive transport could be taking place. However, non-diffusive transport would result in the apparent thermal parameters deviating from the expected values as well as the EDMM, and it can therefore be identified.

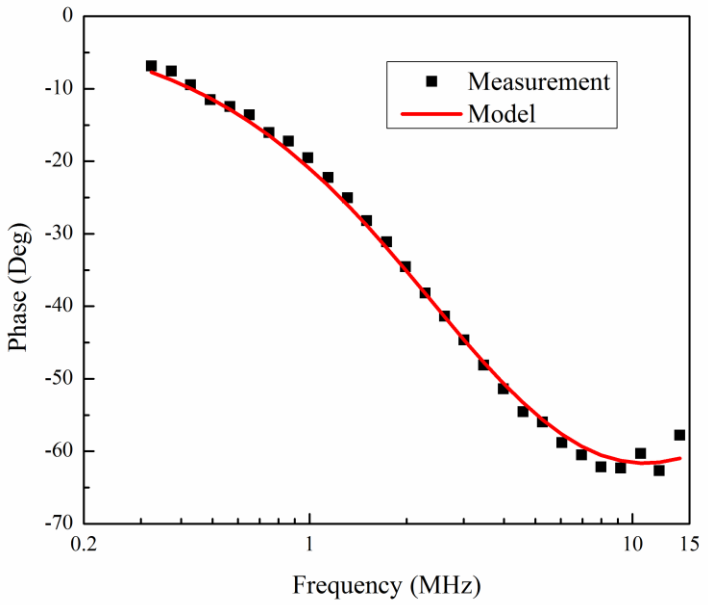

Figure 4-1. Measurement and fit to the thermal phase for the ML-3 structure with 1.25 μm offset.

In FDTR samples are often coated with a thin metallic layer to act as both heater and thermometer. Although the presence of this transducer is often important to improve the signal in FDTR measurements [90], its presence can reduce sensitivity to transport in the layers beneath, particularly if they have high thermal conductivity. This is due to heat spreading in the transducer, which reduces the temperature gradient across the volume of interest. In this work, we do not coat the samples with transducers as the Pt/Co multilayers have shown to possess a substantial thermoreflectance coefficient. The lack of the transducer leads to increased sensitivity to the heat transport in the multilayers.

Table 4-1. Characteristics of the multilayers studied in this work. t_{ML} represents the total thickness of the Pt(2)/[Pt(t_{Pt})/Co(t_{Co})]$_n$/Pt(20)/Ta(1.5) layers, k_r is the in-plane thermal conductivity measured by 4-point probe, and C_{ML} is the volumetric heat capacity of these layers calculated using a weighted average of the volumetric heat capacities of Pt and Co.

	Sample Structure	t_{ML}(nm)	k_r (W/mK)	C_{ML} (MJ/m^{3}K)
ML-1	[Pt(0.7nm)/Co(0.4nm)]x128	164.3	15.0	3.34
ML-2	[Pt(0.7nm)/ Co(0.4nm)]x64	93.9	17.2	3.28
ML-3	[Pt(2.8nm)/ Co(1.6nm)]x32	164.3	22.2	3.34
ML-4	[Pt(11.2nm)/ Co(6.4nm)]x8	164.3	33.0	3.34
ML-5	[Pt(44.8nm)/Co(25.6nm)]x2	164.3	39.8	3.34

The samples studied in this work are layered as Pt(2)/[Pt(t_{Pt})/Co(t_{Co})]$_n$/Pt(20)/Ta(1.5)/SiO_2(100)/Si, where the numbers in parenthesis are the layer thickness in nm (Table 4-1). Note that we have prepared two samples at the highest interface density having different total thickness by varying the total number of Pt/Co repeats. Otherwise the total thickness of Co and Pt is kept constant. The multilayers were deposited at room temperature using an AJA magnetron sputtering system at a base pressure of 1.7×10^{-7} Torr and sputtering pressure of 3 mTorr. The deposition rates for Co and Pt were 0.653 Å/s and 1.002 Å/s, respectively. The thickness of all layers is measured by X-Ray reflectivity. Although not from the same sample, a cross-sectional TEM of such MLs fabricated by the same group who prepared the MLs discussed here [127] is shown in Figure 4-2.

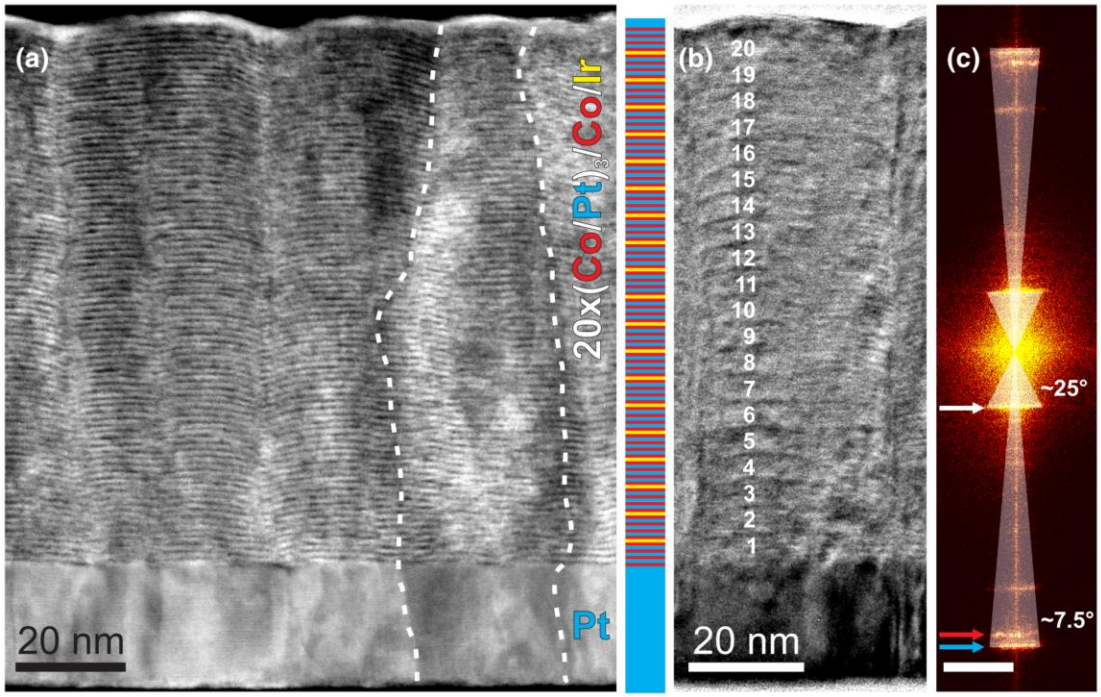

Figure 4-2. (a) High resolution STEM image of 20 repeats of ([Co(0.5 nm)/Pt(0.7 nm)]$_3$/Co(0.5 nm)/Ir(0.5 nm))$_{19}$[Co(0.5 nm)/Pt(0.7 nm)]$_4$ structure on Pt seed layer [127]. The illustration shows the structure where blue, yellow, and red represent Pt, Ir and Co, respectively. (b) Blocks of [Co(0.5 nm)/Pt(0.7 nm)]$_3$/Co(0.5 nm)/Ir(0.5 nm) labeled in high-resolution TEM image. (c) Fast Fourier transform of (a) with scale bar of 1/nm. Reprinted with permission from Phys. Rev. B 100, 140411(R) (2019). Copyright 2019 American Physical Society.

For the thermal analysis of the FDTR data, the samples have been modeled by treating the multilayers along with the cap layer, the seed layer and Ta adhesive layer as a single effective medium as ML/$G_{ML/SiO2}$/SiO_2(100)/$G_{SiO2/Si}$/Si, where ML represents the thermal conductivity of the Pt(2)/[Pt(t_{Pt})/Co(t_{Co})]$_n$/Pt(20)/Ta(1.5) layers. The parameters of interest in this work are the out-of-plane (k_z) and in-plane (k_r) components of the anisotropic thermal conductivity of ML, as k_z will later be used to extract G for the Pt/Co interfaces.

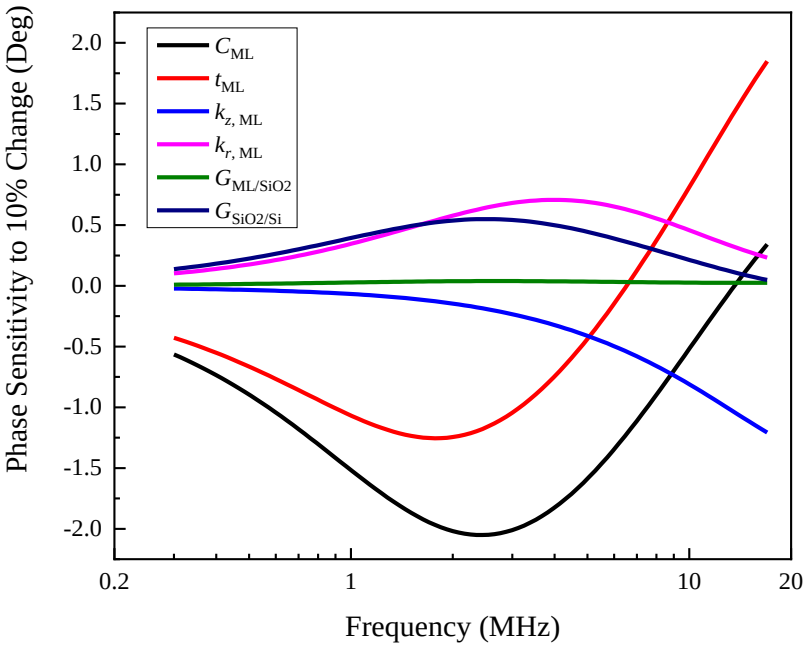

Figure 4-3. Thermal phase sensitivity to 10% change in the parameters labeled for sample ML-3 at 1.25 μm beam offset.

Figure 4-3 shows the sensitivity analysis for the sample ML-3 at 1.25 μm beam offset, where the absolute difference in the modeled thermal phase for each parameter of interest is changed by 10%. The sensitivity analysis depicted in Figure 4-3 shows that by using a frequency range of 300 kHz to 8 MHz, the sensitivity to the parameter of interest is reasonably large compared to the phase noise, rendering measurements of anisotropic thermal conductivity possible. We note that the sensitivity to $G_{SiO2/Si}$ is comparable to k_r. $G_{SiO2/Si}$ was extracted from measurements made on the same substrate coated with Al and kept constant for the analysis of the ML samples. We extracted $G_{SiO2/Si}$ = 27.02 ± 0.78 MW/m^{2}K which is in agreement with our previous measurements [79]. Furthermore, we are using a constant value of 250 MW/m^{2}K as the effective conductance across the ML/SiO_2 layers ($G_{ML/SiO2}$), in agreement with reference [128]. Isotropic thermal conductivities

of k_{SiO2} = 1.32 W/mK and k_{Si} = 145 W/mK, and volumetric heat capacities of C_{SiO2} = 1.59 MJ/m^{3}K and C_{Si} = 1.64 MJ/m^{3}K have been used for the SiO_2 and Si layers. Figure 4-1 shows the thermal phase measured for sample ML-3 and its corresponding fit. To estimate the uncertainties associated with the fitted thermal conductivity measured here (Figure 4-4), a Monte Carlo approach has been employed. Accordingly, errors of ± 0.1 μm for the rms spot size and offset, and ± 1 MW/m^{2}K for $G_{SiO2/Si}$ have been considered over 300 iterations.

To further explore how well we can distinguish fitted values of k_z and k_r, we present contours of uncertainty arising from correlation between k_r and k_z. This is performed by calculating the mean square error between model and measured data for combinations of k_r and k_z values using the mean square error $\sigma = \frac{1}{n}\sum_{i=1}^{n}\left(\frac{X_{m,i} - X_{d,i}}{X_{d,i}}\right)^2$ where n is the number of frequency points and $X_{m,i}$ and $X_{d,i}$ represent phase values from the model and the measurement at the i-th frequency point, respectively [129]. Figure 4-5 shows the contours of combinations of k_r and k_z for ML-1 (with the largest correlation between k_r and k_z) and ML-5 (with the smallest correlation between k_r and k_z), which produce a standard deviation smaller than $2\sigma_{min}$, where σ_{nin} represents the best fit. The correlation for ML-1 is present, as evident by the contour's diagonal. However, the correlations are restricted to narrow ranges in k_r and k_z for good fits, rendering the extracted values meaningful. The correlation for ML-5 is weak, indicating the fit to these two parameters is relatively independent. However, the contours are broad for k_z, indicating a larger uncertainty for the extraction of this parameter. This is due to the low thermal resistance for this ML sample having the fewest number of interfaces.

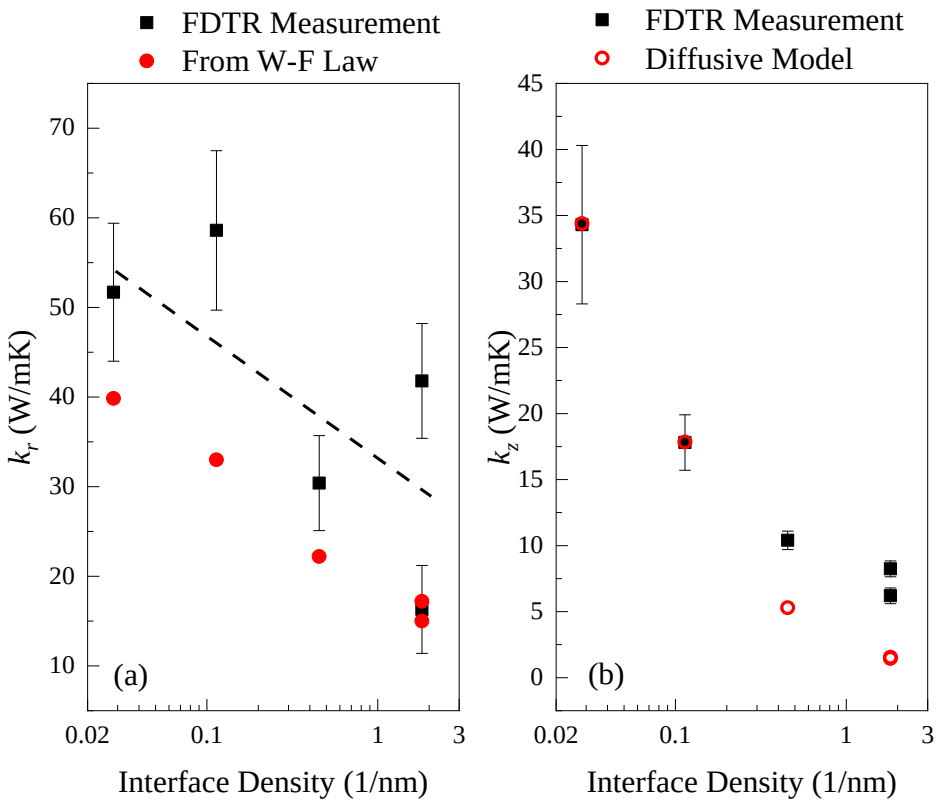

Figure 4-4. (a) In-plane thermal conductivity of the Pt/Co multilayers as function of interface density extracted from FDTR fits (squares) and 4-point probe through Wiedemann-Franz law (circles). The dashed line is a guide to the eye that shows the average offset between the FDTR and electrical data. (b) Out-of-plane thermal conductivity of the Pt/Co multilayers as function of interface density from FDTR (square) and diffusive model (Eq. 1) with constant G of 2.5 GW/m^{2}K (circle). At the highest interface density point, two different samples have been measured, and for these the model prediction for k_z overlaps.

4.3 Results and Discussions

Figure 4-4a compares k_r for the multilayers extracted from FDTR fits and from the 4-point probe measurements and applying the Wiedemann-Franz law, showing a reasonably similar trend in light of the difficulty in extracting k_r of metallic layers via FDTR. The uncertainties in k_r do not affect the analysis and interpretation of k_z, and indicate that the multilayers have an anisotropy k_r/k_z increasing from ~1.2 to ~2 as the interface density increases from ~0.03/nm to ~2/nm. We note

that FDTR is measures the total thermal conductivity, due to both electron and phonon transport, whereas the 4-point probe measurement is representative of electron transport only. Therefore, the somewhat higher value extracted through FDTR can be attributed in part to the additional contribution of phonon transport. Overall k_r reduces by about a factor of 2 in the range of interface densities studied here, an effect that can be attributed to increased scattering due to finite layer size [130, 131].

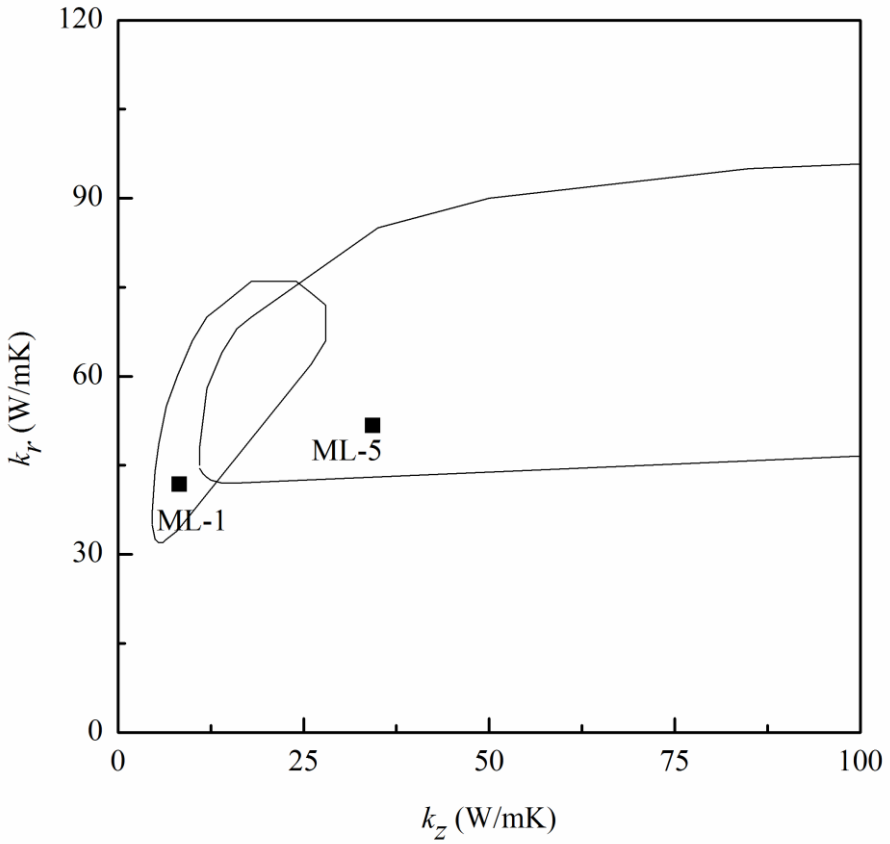

Figure 4-5. Contour plots of the correlation in the fitted values for k_r and k_z for (a) ML-1 and (b) ML-5.

The effective out-of-plane thermal conductivity k_z of the multilayers is depicted in Figure 4-4b as function of interface density. As expected, k_z decreases as the number of interfaces increase due

to their increasing resistive contribution to the overall transport. For purely diffusive transport, one could relate G of the Pt/Co interfaces to k_z using [60]:

$$\frac{t_{ML}}{k_z} = R_0 + \frac{n}{G_{Pt/Co}} \tag{4.1}$$

where t_{ML} is the thickness of the multilayer, R_0 is the total thermal resistance per unit area of the Pt and Co layers excluding the interfaces, and n is the number of interfaces. We set the value of R_0 as determined by the thermal conductivity for the in-plane direction, therefore $R_0 = \frac{t_{ML}}{k_r}$. By extracting R_0 from the k_r values measured by FDTR in Figure 4-4a we are able to capture finite size and microstructural contributions to k_z and make no assumptions for the conductivity of the Pt and Co layers. The values for G obtained this way are depicted in Figure 4-6 as a function of interface density. One can observe that G is not constant beyond the experimental uncertainty and increases from a value of ~2.5 GW/m^{2}K at low interface densities to ~15 GW/m^{2}K at high interface densities, an indication of non-diffusive transport. This deviation from a diffusive model is also shown in Figure 4-4b where the result of equation (4.1) is plotted for constant G = 2.5 GW/m^{2}K. Next, we will present how this data compares with theory and other literature data.

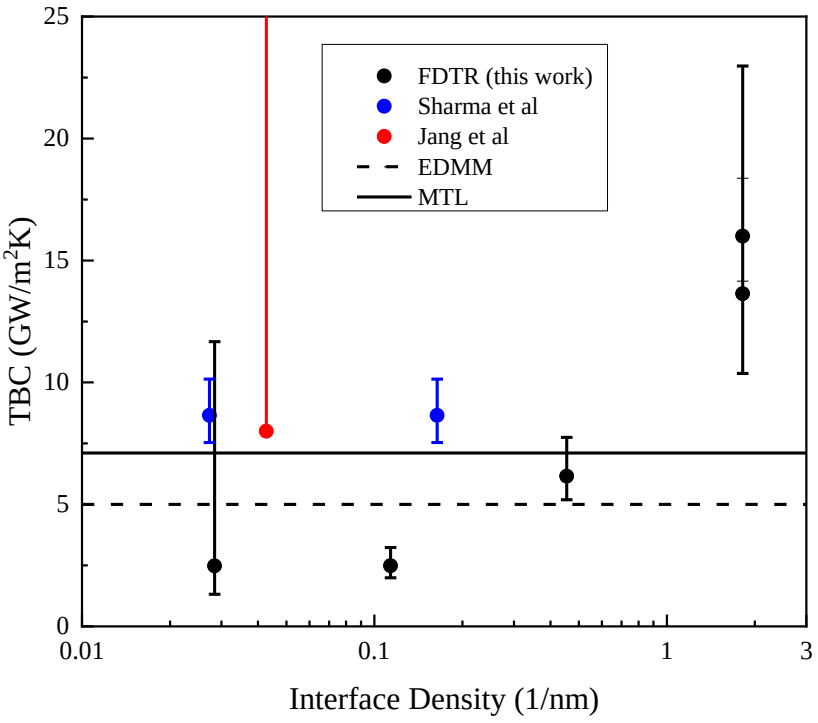

Figure 4-6. Thermal boundary conductance of Pt/Co extracted from FDTR fits compared with literature data from Sharma [132], Jang [120], and the predictions from EDMM and MTL.

We start the theoretical analysis by estimating the maximum theoretical value of $G_{Pt/Co}$. The maximum transmission limit (MTL) for electrons, which is a special case of the EDMM, sets an upper limit for G in metallic interfaces by allowing perfect transmission and is only limited by the first and the second laws of thermodynamics [23]. Accordingly, the upper limit can be calculated by $G_{MTL} = \frac{v_f \gamma T}{4}$, where v_f is the Fermi velocity, γ is the Sommerfeld parameter and T is temperature with the product γT being the electronic volumetric heat capacity. Considering the (111) *fcc* crystal structure of the multilayers confirmed by X-Ray diffraction, we take the v_f value along this direction $v_{f,Pt} = 2.37 \times 10^5 ms^{-1}$ [133] and $v_{f,Co} = 3.3 \times 10^5 ms^{-1}$ [134], and

$\gamma_{Pt} = 400\,Jm^{-3}K^{-2}$ [120] and $\gamma_{Co} = 680\,Jm^{-3}K^{-2}$ [120] for the Sommerfeld parameters, and obtain G_{MTL} = 7.11 GW/m^{2}K. Beyond this limiting case, according to the EDMM [59, 60], the thermal boundary conductance is $G = \frac{Z_1 Z_2}{4(Z_1 + Z_2)}$, where $Z = \gamma T v_f$ and the subscripts refer to materials 1 and 2 on either side of the interface. Using the Fermi velocities and electronic heat capacities for Pt and Co, $G_{Pt/Co}$ = 5.0 GW/m^{2}K. The results of the MTL and EDMM are also shown in Figure 4-6. For the samples with sub-nanometric layers (ML-1 and ML-2) having an interface density ~2/nm, a large deviation is observed from the predictions of MTL and EDMM. Since both MTL and EDMM are based on diffusive transport, we attribute this deviation to the non-diffusive nature of transport in these two samples, as the mean free path of electrons is much larger than the period thickness in ML-1 and ML-2.

Here, we claim that the trend observed in Figure 4-6 is not affected by structural defects and discontinuities, as defects reduce the TBC through increased scattering and the continuity of the layers is ensured through magnetization hysteresis loops.

It is worth comparing $G_{Pt/Co}$ obtained in this work with that of Jang *et al*. [120], who measured it to be $\geq$ 8 GW/m^{2}K. Their experiment was performed on a Pt (42 nm)/Co (0.8 nm)/Pt (4 nm)/sapphire sample consisting of two Pt/Co interfaces. The reason why they were only able to set a lower bound for the conductance was likely due to a small sensitivity of their measurement to the two highly conductive interfaces.

Another method to infer the thermal conductance of the metallic interfaces is through Current-Perpendicular-to-Plane (CPP) electrical resistivity measurements [135]. In CPP, the sample of interest is sandwiched between two contacts allowing a uniform current to pass through the sample. The specific resistance (*AR*, where *A* and *R* represent area through which current passes and sample

resistance, respectively) of the interface is then extracted from the total specific resistance of the sample measured as a function of number of interfaces for samples with different number of interfaces [135]. Wilson and Cahill showed that the *AR* measurements of Pd/Ir layers can be related to *G* through the interfacial form of the Wiedemann-Franz law [60], expressed as $\frac{GAR}{T} = L_0$, where L_0 is the Sommerfeld value of the Lorenz number (2.45×10^{-8} ΩWK^{-2}). Sharma *et al*. measured the specific resistance of Pt/Co interfaces as $AR = 0.85 \pm 0.125$ $f\Omega m^2$ [132], which translates to $G \sim 8.65$ GW/m^2K using the interfacial form of the Wiedemann-Franz law. We note that the literature data by Jang and Sharma are similar, are close to G_{MTL} but are obtained at interface densities below 0.2/nm.

We have so far only considered electron transport in our discussion, under the assumption that it dominates the transport in the metallic multilayers. Thermoreflectance measurements yield the total thermal conductivity, consisting of both electron and phonon carriers. The work of Wilson and Cahill is indicative that the interfacial form of the Wiedemann-Franz law holds at room temperature at least to interface densities up to ~0.5/nm and that the EDMM is sufficient to accurately describe the system [60]. The agreement between thermoreflectance measurements and EDMM in their work indicates that even at such relatively low k_z, the thermal transport in the multilayer system is dominated by electrons. In our measurements the higher value for k_r obtained by FDTR with respect to electrical conductivity measurements would point to a non-negligible phonon contribution to the total conductivity. This is also supported by the value we derived for $G_{Pt/Co}$, which is lower than the EDMM prediction, consistent with phonon contribution to the overall k_z being non-negligible. The onset of non-diffusive transport observed in Figure 4-6 appears for layer thickness well below the mean free path for both electrons and phonons. This opens the question of whether the non-diffusive transport we are observing originate from the

electronic contribution, phononic contribution or both. While we cannot conclusively say which case applies here, there is indication that the electron transport dominates, since the difference in FDTR and 4-point probe data points to electrons being the greatest contributor to the conductivity in Figure 4-4a. Future thermal conductivity measurements coupled with CPP electrical conductivity measurements at interface densities above 1/nm may further clarify the relative role of electron and phonons and confirm whether the interfacial form of the Wiedemann-Franz law remains valid in this limit.

The increase in $G_{Pt/Co}$ has been interpreted here as evidence for non-diffusive transport, but the mechanism should be explored further. In the particle picture of transport, this would be an indication that carriers are not in equilibrium as they traverse the structure and quasi-ballistic transport is present, but in the wave picture a diverging conductance is a sign of coherence [125]. The former, for instance, can be explained by electron not being scattered enough or being scattered elastically at the interfaces and therefore travelling a longer distance before getting thermalized. The latter however seems unlikely for electron-mediated transport at room temperature, given the very small electron coherence lengths. While we do not observe a minimum in k_z for the interface density range explored in this work, one might speculate that k_z would increase in the limit where the Pt/Co layering is extended to monoatomic thickness as is the case for the thermal conductivity of L_10 ordered crystal phases as compared to equiatomic disordered alloys [99].

4.4 Conclusion

In conclusion, the anisotropic thermal conductivities of different Pt/Co multilayers were measured as a function of interface density. The thermal boundary conductance of Pt/Co interface was

extracted and compared with calculations from the electronic diffuse mismatch model. We showed an increase in the boundary conductance at high interface densities which might be arising from the non-diffusive heat transport at sub-nanometric scales.

Chapter 5: Room-temperature micrometer-scale phonon ballistic transport in WS_2

Thermal transport in 2D crystals is tied to their performance in a variety of applications, but the transport physics can significantly deviate from the bulk when carrier mean free path becomes comparable with the size of the heat source or device length. Here, we report a strong heater size dependence of the apparent in-plane and out-of-plane components of the thermal conductivity of bulk WS_2 when measured with variable laser spot sizes via frequency domain thermoreflectance. Changing the pump laser spot size from ~14 μm to ~1.5 μm, the measured in-plane thermal conductivity reduces by ~60%, while a ~35% reduction is observed for the out-of-plane component of the thermal conductivity. We interpret this reduction of thermal conductivity by comparing the laser spot size to the phonon mean free path spectra determined by first-principle calculations. The results presented here show a dramatic behavior for WS_2, as its in-plane thermal conductivity is dominated by contributions from phonons with mean free paths above 1 micrometer. These results also highlight that care must be taken when interpreting thermal conductivity data in 2D crystals when the heater spot size is small, a situation that can often take place using thermoreflectance or Raman thermometry measurements.

5.1 Introduction

Advances in synthesis and characterization of 2D materials have attracted a lot of interest for electronics and optoelectronics applications. However, their thermal characterization often lags optoelectronic characterization, even though for applications both aspects need to be well

understood. As thermal characterization might be performed using varied techniques and different 2D crystals vary in their thermal characteristics, often displaying anisotropic properties, care must be taken when comparing and interpreting the results.

When material characteristic length scales (L_C) become comparable to the mean free path (MFP) of the energy carriers (e.g. phonons in semiconductors and dielectrics), thermal transport becomes non-diffusive and the apparent thermal properties diverge from their bulk values. Examples of these material characteristic length scales are the heater size [13, 89, 103, 136], thermal penetration depth (a depth at which the temperature amplitude is $1/e$ of the surface temperature amplitude) [14, 16], and physical dimensions (such as sample size or discontinuities such as grain boundaries) [12, 29, 137]. A comparison between L_C and the MFP of phonons determines whether the heat transfer is diffusive (L_C >> MFP) or non-diffusive (L_C ~ MFP or L_C << MFP). Signs of non-diffusive transport could be a reduced apparent thermal conductivity, L_C dependence of the thermal conductivity, or generally a lack of proportionality between heat flux and thermal profiles. In these different regimes interpreting the thermal behavior is not trivial and subject of research.

The thermal conductivity accumulation function, $k_{accum}(\Lambda^*)$, can be used to study the contributions of phonons with different MFPs to the overall thermal conductivity:

$$k_{accum}(\Lambda^*) = \frac{1}{3}\int_0^{\Lambda^*} Cv\Lambda\left(d\Lambda/d\omega\right)^{-1} d\Lambda \tag{5.1}$$

where C, v, and Λ represent mode dependent specific heat, group velocities and MFP, respectively [136]. $k_{accum}(\Lambda^*)$ describes the contribution of phonons whose MFPs are smaller than Λ^* to the thermal conductivity, so $k_{accum}(\Lambda^*) \rightarrow k_{bulk}$ as $\Lambda^* \rightarrow \infty$.

The contribution of phonons up to a specific MFP can be experimentally obtained by changing the L_C such that the contribution of larger MFP phonons is suppressed [136]. Through a systematic variation of L_C, the MFP distribution of thermal conductivity can be constructed [98, 124]. This, however, assumes that the suppression function that relates thermal conductivity to MFPs is known. Nonetheless, seeing size scale (or time scale) dependence for the experimentally determined thermal conductivity is an indicative sign that non-diffusive transport is taking place and that L_C is approaching MFP.

Finite-size effects can arise in several thermal characterization techniques used to investigate 2D materials. For instance, Raman thermometry has been used to measure thermal conductivity of mono- and bilayer WS_2 [138], MoS_2 [139, 140], $MoSe_2$ [140], h-BN [141], and single layer Graphene [142]. However, since the spot size in these experiments is often of the order of 1 μm or smaller [138-143], non-diffusive effects can ensue when the MFPs of heat carriers become comparable with the heating laser spot size. For instance, Liu and coworkers measured the thermal conductivity of MoS_2 crystal using a beam offset time-resolved magneto-optical Kerr effect (TR-MOKE) and showed a reduction of in-plane thermal conductivity (k_r) from 110 ± 20 W/mK to 85 ± 6 W/mK when the spot size decreased from ~6 μm to ~1.2 μm [89]. A k_r of ~105 W/mK was also reported for bulk MoS_2 using a beam-offset time domain thermoreflectance (TDTR) spot size of ~2.7 μm [144]. This would roughly indicate that at a size scale of ~1 μm some phonons travel non-diffusively. Non-diffusive phonon transport has also been recently observed in MoS_2 thin films through thickness dependent out-of-plane thermal conductivity (k_z) measurements [12].

WS_2 is a transition metal dichalcogenide (TMD) crystal whose layered structure can yield 2D crystals [145]. The bandgap of different TMDs range from visible to infrared [146], and interestingly, the bandgap can change from indirect to direct when the thickness is reduced from

bulk to monolayer [147]. A bulk WS_2 crystal behaves as a semiconductor with an indirect band gap of 1.3-1.4 eV [148], while monolayer WS_2 exhibits a direct bandgap of 1.8-2.1 eV [148]. This tunable bandgap of TMDs is desirable for many applications where other well-known 2D materials, such as zero-bandgap graphene, are not suitable [147].

In this work, we reveal non-diffusive phonon transport in WS_2 and show that this takes place at relatively large values of L_C just below 10 μm. Pisoni and coworkers employed a steady state method to measure the thermal conductivity of single crystal WS_2 and reported room temperature values of k_r = 124 W/mK and k_z = 1.7 W/mK [149]. In this type of measurements, any deviation from a perfect crystal would arise due to sample imperfections such as grain boundaries. Lindroth and Erhart used first-principles calculations to study the anisotropic thermal conductivity of different TMDs [150]. They revealed that phonons with MFP smaller than 1 μm are responsible for only ~10% of k_r and ~60% of k_z of bulk WS_2 and consequently, a large portion of heat transport in WS_2 takes place by phonons having MFP above 1 μm at room temperature [150]. Further measurements [151] and calculations [152] showed agreement with the results presented by Pisoni and coworkers [149] and Lindroth and Erhart [150]. We note that the thermoreflectance measurements by Jiang *et al*. [151] have indicated some non-diffusive effects in k_z. A summary of thermal conductivity measurements on WS_2 is listed in Table 5-1.

The laser spot size dependence of the k_r and k_z of WS_2 will be presented here, as determined by frequency domain thermoreflectance (FDTR). Our results present, to the best of our knowledge, the first experimental evidence that transport in WS_2 at room temperature is strongly non-diffusive even at length scales of several μm. The results are corroborated using first principle calculations. The contribution of phonons with such a long MFP to k_r is not common, and comparable to graphite [88].

Table 5-1. A summary of theoretical and experimental k_r and k_z values of bulk WS_2 at room temperature reported in the literature.

	k_r (W/mK)	k_z (W/mK)
Theory (Ref. [152])	153	3.9
Theory (Ref. [150])	126	4.7
Exp. (Ref. [151])	120	2.8
Exp. (Ref. [149])	124	1.7

5.2 Experimental Setup, Sample Preparation and Sensitivity Analysis

The thermal properties of interest were measured through FDTR as described elsewhere [79, 80]. Briefly, the temperature fluctuations caused by an intensity modulated pump laser are measured by a probe beam at the sample surface through changes in temperature-dependent reflectivity variations, i.e., thermoreflectance. The reflected light then is collected using a photodetector and demodulated using the lock-in amplifier. The measured parameter, i.e. the phase lag between the heat flux and the surface temperature, which contains the temperature response of the sample is then fitted to the solution of the heat diffusion equation to determine k_r and k_z. The measurements are repeated as function of laser spot size. In the case of diffusive heat transport the resulting values would be independent of laser spot size.

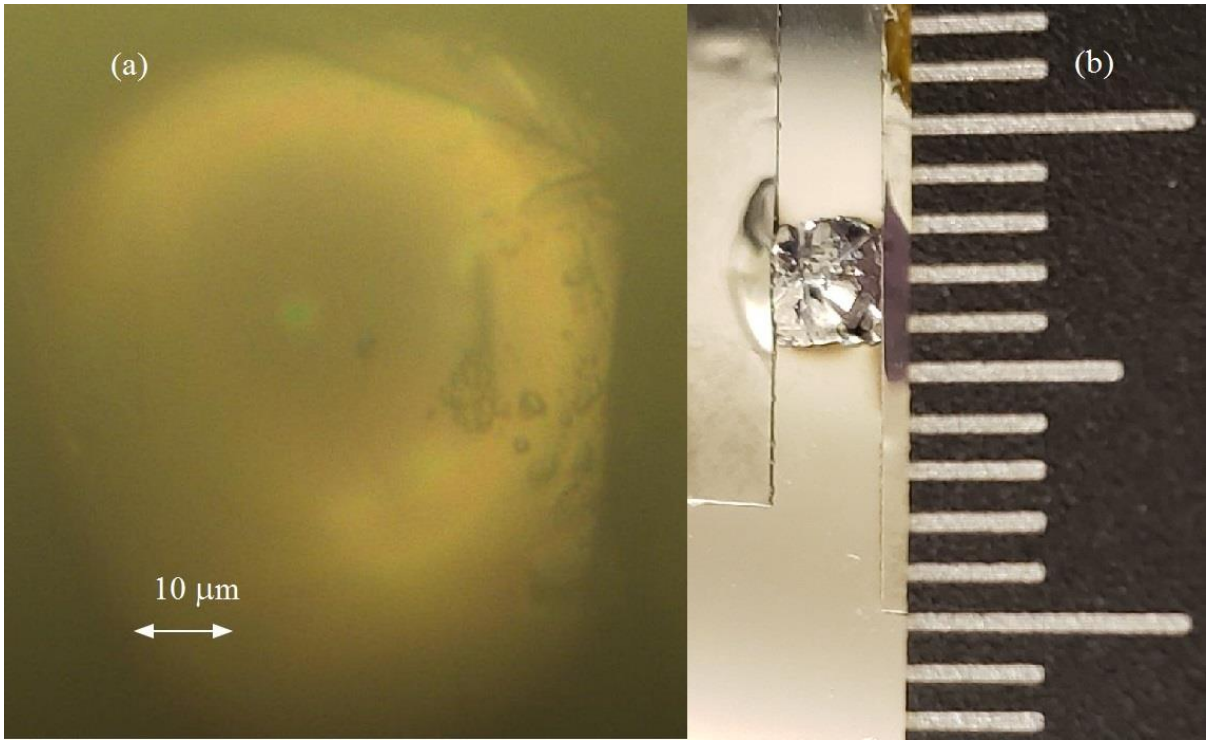

Figure 5-1. Image of the Al/WS_2 sample (a) under microscope, and (b) taped for measurement. Each line represents one millimeter.

The samples were coated with a 52 nm Al layer to perform FDTR measurements (Figure 5-1). Two WS_2 crystals sourced differently were used to validate the results. Four-point probe measurements were used to determine the in-plane thermal conductivity of the Al layer as 85 W/mK through the Wiedemann-Franz law. To vary the optical spot size, we used Olympus 4X (pump spot size of 13.9 μm), 10X (pump spot size of 5.42 μm) and 40X (pump spot size of 1.45 μm) objectives. When changing spot size, laser powers were changed accordingly to keep the temperature rise relatively the same between measurements with different spot sizes.

In order to gain insight into the sensitivity of measurement to different thermophysical parameters of a given system, we perform a sensitivity analysis to examine how sensitive the thermal phase is

to different parameters. This is achieved by taking the absolute difference in the modeled thermal phase when the parameter of interest is changed by 10%. The sensitivity of the thermal phase to changes of k_r and k_z of WS_2 using difference spot sizes is depicted in Figure 5-2.

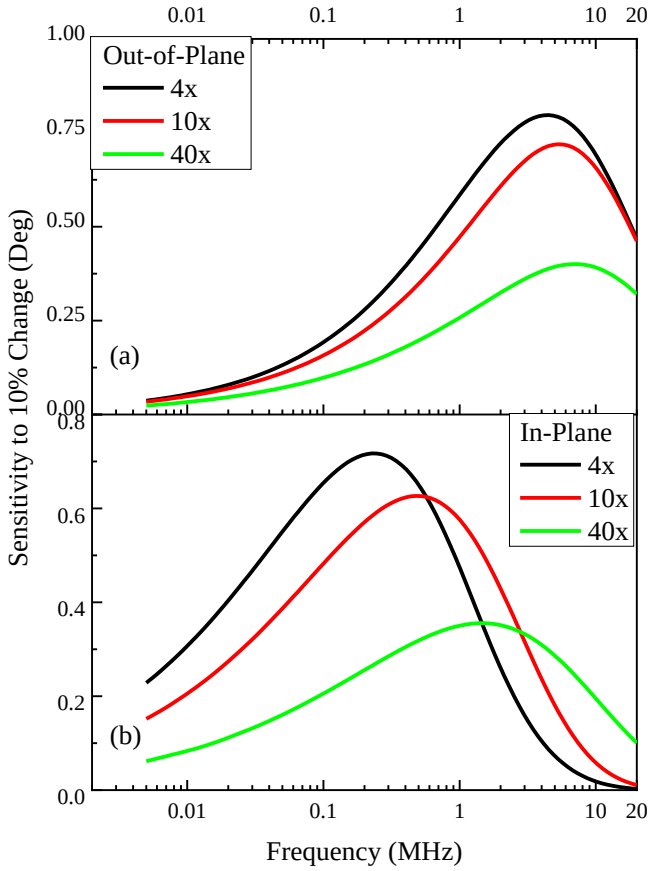

Figure 5-2. Phase Sensitivity to 10% change of thermal conductivity components at different spot sizes with 4x, 10x and 40x objectives. In each case we use the thermal conductivity values that were determined through the measurements: (a) for k_z values of 1.71, 1.53 and 1.13 W/mK and (b) for k_r values of 145, 74.3 and 56.8 W/mK.

5.3 Results and Discussions

The samples were measured for three different heater spot sizes. Using the largest spot size, the Thermal Boundary Conductance (TBC) of the Al/WS_2 interface was extracted as well as k_r and k_z.

The Al/WS_2 TBC was measured to be 13.29 ± 0.47 MW/m^2K and then kept constant for measurements using smaller spot sizes. In-plane thermal conductivities of 145 ± 4.25, 74.3 ± 1.75 and 56.8 ± 3.25 W/mK, and out-of-plane thermal conductivities of 1.71 ± 0.03, 1.53 ± 0.03 and 1.13 ± 0.06 W/mK were obtained for 4x, 10x and 40x objectives.

The k_z measured with the 4x objective (1.71 ± 0.03 W/mK) is close to the measurement reported by Pisoni and coworkers [149]. Furthermore, the trend of thermal conductivity reduction with decreasing spot size observed in this work (Figure 5-3) is in good qualitative agreement with the thermal conductivity accumulation function calculated by Lindroth and Erhart [150]. By comparing the laser spot size to phonon MFP reported by first-principle calculations [150], the reduction of thermal conductivity can be interpreted under the assumption that MFP and heater size can be directly compared. Here, we make a simplified assumption that the heater size is directly compared with the MFP of phonons. Lindroth and Erhart calculated that phonons with MFP of ~ 1 μm, 5 μm and 10 μm are responsible for ~10%, ~95% and ~100% of k_r of bulk WS_2 at room temperature, while phonons with MFP of ~ 1 μm and 10 μm carry ~60% and ~90% of the bulk k_z [150]. Therefore by decreasing the heater size, phonons will travel ballistically outside of the measurement volume and will not contribute to the thermal conductivity and a reduced thermal conductivity is observed.

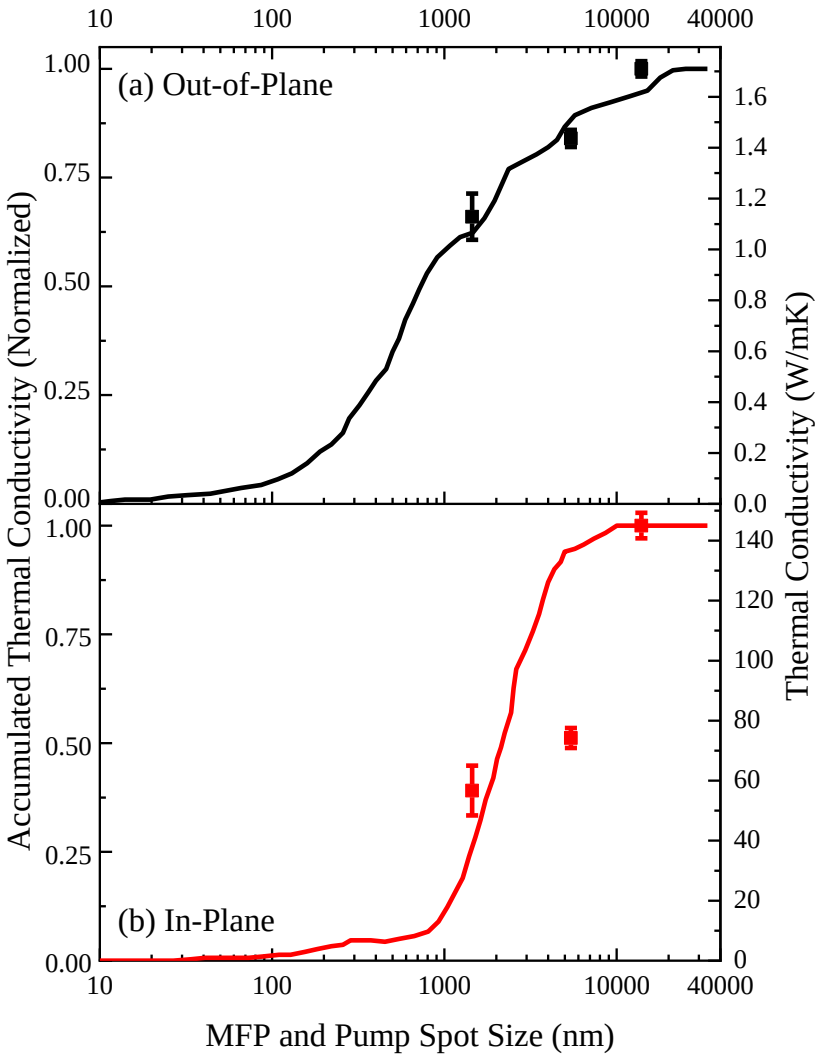

Figure 5-3. Accumulated thermal conductivity of WS_2 crystal (solid lines) as a function of MFP adapted from Ref. [150], and thermal conductivity measured in this work as a function of pump spot size (squares) in (a) out-of-plane direction, and (b) in-plane direction.

5.4 Conclusion

In conclusion, the effects of heater spot size on in-plane and out-of-plane components of thermal conductivity of bulk WS_2 was investigated. A strong spot size dependent non-diffusive transport was observed at room temperature at the micrometer scale, which highlights that care must be

taken in interpreting thermal conductivity data obtained with small heater sizes as is often the case for thermoreflectance and Raman thermometry techniques.

Chapter 6: Summary and Conclusion

6.1 Summary

In this dissertation, heat transport within bulk and nanoscale materials as well as across interfaces was investigated. By establishing a FDTR setup, we were able to validate the functionality of our system to obtain typical thermal properties (section 3.1). We showed that by utilizing a small spot size (~ 1 μm), reliable high frequency thermoreflectance measurements can be performed. The sensitivity of the measurements to anisotropic heat transfer was increased by introducing an offset between pump and probe beams. We showed that beam-offset FDTR is capable of measuring in-plane and out-of-plane components of thermal conductivity as well as TBC of different structures, such as Al-coated graphite (section 3.2). Furthermore, by employing Kerr effect, the sensitivity was further increased (section 3.3). Since frequency of the heating source is an important parameter in controlling and studying the mean free path spectrum of thermal conductivity, we implemented two different variations of BB-FDTR presented by Regner and co-workers [16] without the need to use expensive electro-optic modulators to achieve high frequency measurements (section 3.4).

The techniques implemented were then used to measure non-diffusive heat transport in metallic Pt/Co multilayers (chapter 4). In the case of the metallic Pt/Co multilayers, we showed a deviation from the electronic diffusive heat transport theories for the first time, to the best of our knowledge. However, more work needs to be done to address the origin of this deviation. Finally, a strong non-diffusive heat transport in WS_2 crystal was revealed at room temperature as a function of heater

spot size (chapter 5). The data measured in this work can further be used to study MFP-dependent thermal conductivity of WS_2 crystal.

In both non-diffusive studies mentioned in this work, thermal transport across interfaces was assumed to be diffusive. However, it should be noted that interfaces can be selective to some carriers. When the materials near an interface are thin and carriers are not equilibrated, the TBC can be affected too, as the impinging flux is not representative of that of the bulk material. Therefore, non-diffusive treatment of these interfaces can be investigated as well.

6.2 Future Work

In chapter 3, several variations of FDTR were presented. These methods can potentially be extended to measure thermal conductivity maps of different structures [78]. In addition, the effectiveness of these methods can be explored for fast measurements of different materials, to be used as a quality check in an industrial environment [153].

In chapter 4, traces of non-diffusive transport across metallic Pt/Co multilayers were observed. However, more work needs to be done in order to confirm whether the non-diffusive transport exists in these metallic multilayers when the interface density increases. Furthermore, the mechanism of the non-diffusive transport can be explored to understand how much electrons and phonons are responsible in the observed non-diffusive transport. In addition, investigation of other metallic multilayer systems could be beneficial to better understanding the mechanism of heat transport in metallic multilayers when the period thickness is much smaller than the electronic mean free path. While a particle-picture can sufficiently describe heat transport in low interface density superlattices (incoherent regime), the wave nature of heat carriers might affect heat

transport high interface densities (coherent regime) depending on the coherence length of the carriers and period thickness. For instance, a minimum in thermal conductivity of superlattices observed at the crossover of coherent and incoherent regimes as a function of interface density has been attributed to wave nature and coherence of phonons [154]. While we did not observe such a crossover in thermal conductivity of the Pt/Co multilayers investigated in this work, this topic can be investigated specially at cryogenic temperatures.

Improving the efficiency and lifetime of different devices in fields such as nano-electronics and energy conversion is directly related to engineering the existing systems of materials and exploring properties of newly discovered materials. For instance, van der Waals (vdW) heterostructures (HTs), which are made of layers of different materials vertically stacked together by van der Waals forces, have attracted a lot of attention in the recent years as they show different properties compared to the materials forming them [152, 155]. Due to the large number of currently available 2D crystals, a large number of different variations of vdW HTs with different properties can potentially be made [156]. These systems can be studied to find and engineer thermal properties which do not exist naturally in other materials [152] using suitable metrology techniques (such as the techniques presented in chapter 3).

Bibliography

[1] J. Fourier, "Théorie analytique de la chaleur" Paris 1822, English translation "The Analytical Theory of Heat," ed: Dover Publications, Mineola, New York, 2003.

[2] R. P. Feynman, "There's plenty of room at the bottom," *California Institute of Technology, Engineering and Science magazine,* 1960.

[3] T. Amundsen and T. Olsen, "Sizde-dependent thermal conductivity in aluminium films," *Philosophical Magazine,* vol. 11, no. 111, pp. 561-574, 1965.

[4] V. Abrosimov, B. Egorov, N. Lidorenko, and I. Rubashov, "INVESTIGATION OF THE THERMAL CONDUCTIVITY OF THIN METALLIC FILMS," *SOV PHYS SOLID STATE,* vol. 11, no. 2, pp. 427-428, 1969.

[5] K. Chopra and P. Nath, "Thermal conductivity of ultrathin metal films in multilayer structures," *Journal of Applied Physics,* vol. 45, no. 4, pp. 1923-1925, 1974.

[6] C. Tien, B. Armaly, and P. Jagannathan, "Thermal conductivity of thin metallic films and wires at cryogenic temperatures," *Thermal Conductivity,* pp. 13-19, 1969.

[7] N. Savvides and H. Goldsmid, "Boundary scattering of phonons in silicon crystals at room temperature," *Physics Letters A,* vol. 41, no. 3, pp. 193-194, 1972.

[8] B. Yang and G. Chen, "Experimental studies on thermal conductivity of thin films and superlattices," in *Thermal Conductivity*: Springer, 2004, pp. 167-186.

[9] M. M. Waldrop, "The chips are down for Moore's law," *Nature News,* vol. 530, no. 7589, p. 144, 2016.

[10] E. Pop, "Energy dissipation and transport in nanoscale devices," *Nano Research,* vol. 3, no. 3, pp. 147-169, 2010.

[11] J. Yang, "Theory of thermal conductivity," in *Thermal Conductivity*: Springer, 2004, pp. 1-20.

[12] A. Sood *et al.*, "Quasi-ballistic thermal transport across MoS2 thin films," *Nano letters,* vol. 19, no. 4, pp. 2434-2442, 2019.

[13] Y. Hu, L. Zeng, A. J. Minnich, M. S. Dresselhaus, and G. Chen, "Spectral mapping of thermal conductivity through nanoscale ballistic transport," *Nature nanotechnology,* vol. 10, no. 8, p. 701, 2015.

[14] K. T. Regner, D. P. Sellan, Z. Su, C. H. Amon, A. J. McGaughey, and J. A. Malen, "Broadband phonon mean free path contributions to thermal conductivity measured using frequency domain thermoreflectance," *Nature communications,* vol. 4, p. 1640, 2013.

[15] P. E. Hopkins, "Thermal transport across solid interfaces with nanoscale imperfections: Effects of roughness, disorder, dislocations, and bonding on thermal boundary conductance," *ISRN Mechanical Engineering,* vol. 2013, 2013.

[16] K. Regner, S. Majumdar, and J. A. Malen, "Instrumentation of broadband frequency domain thermoreflectance for measuring thermal conductivity accumulation functions," *Review of Scientific Instruments,* vol. 84, no. 6, p. 064901, 2013.

[17] A. J. Schmidt, "Optical characterization of thermal transport from the nanoscale to the macroscale," Massachusetts Institute of Technology, 2008.

[18] K. Regner, L. Wei, and J. Malen, "Interpretation of thermoreflectance measurements with a two-temperature model including non-surface heat deposition," *Journal of Applied Physics,* vol. 118, no. 23, p. 235101, 2015.

[19] Y. Takeda, J. Lu, and N. Kishimoto, "Nonlinear response of metal nanoparticle embedded in insulators by 60-keV negative ion implantation," in *Smart Materials II*, 2002, vol. 4934, pp. 46-51: International Society for Optics and Photonics.

[20] A. Majumdar and P. Reddy, "Role of electron-phonon coupling in thermal conductance of metal-nonmetal interfaces," *Applied Physics Letters,* vol. 84, no. 23, pp. 4768-4770, 2004.

[21] A. A. Balandin, "Thermal properties of graphene and nanostructured carbon materials," *Nature materials,* vol. 10, no. 8, pp. 569-581, 2011.

[22] G. Chen, *Nanoscale energy transport and conversion: a parallel treatment of electrons, molecules, phonons, and photons*. Oxford University Press, 2005.

[23] C. Monachon, L. Weber, and C. Dames, "Thermal boundary conductance: A materials science perspective," *Annual Review of Materials Research,* vol. 46, pp. 433-463, 2016.

[24] T. M. Tritt, *Thermal conductivity: theory, properties, and applications*. Springer Science & Business Media, 2005.

[25] E. S. Toberer, L. L. Baranowski, and C. Dames, "Advances in thermal conductivity," *Annual Review of Materials Research,* vol. 42, pp. 179-209, 2012.

[26] D. Zhao, X. Qian, X. Gu, S. A. Jajja, and R. Yang, "Measurement techniques for thermal conductivity and interfacial thermal conductance of bulk and thin film materials," *Journal of Electronic Packaging,* vol. 138, no. 4, 2016.

[27] L. Carlos and F. Palacio, *Thermometry at the Nanoscale: Techniques and Selected Applications* (no. 38). Royal Society of Chemistry, 2015.

[28] P. E. Hopkins and J. C. Duda, *Introduction to nanoscale thermal conduction*. INTECH Open Access Publisher, 2011.

[29] K. T. Regner, J. P. Freedman, and J. A. Malen, "Advances in studying phonon mean free path dependent contributions to thermal conductivity," *Nanoscale and Microscale Thermophysical Engineering,* vol. 19, no. 3, pp. 183-205, 2015.

[30] D. G. Cahill *et al.*, "Nanoscale thermal transport. II. 2003–2012," *Applied physics reviews,* vol. 1, no. 1, p. 011305, 2014.

[31] F. Yang and C. Dames, "Heating-frequency-dependent thermal conductivity: An analytical solution from diffusive to ballistic regime and its relevance to phonon scattering measurements," *Physical Review B,* vol. 91, no. 16, p. 165311, 2015.

[32] A. Minnich, "Advances in the measurement and computation of thermal phonon transport properties," *Journal of Physics: Condensed Matter,* vol. 27, no. 5, p. 053202, 2015.

[33] Y. K. Koh and D. G. Cahill, "Frequency dependence of the thermal conductivity of semiconductor alloys," *Physical Review B,* vol. 76, no. 7, p. 075207, 2007.

[34] P. E. Hopkins, "Interfacial Electron and Phonon Scattering Processes in High-Powered Nanoscale Applications," Sandia National Laboratories (United States). Funding organisation: US …2011.

[35] Z. Tong, S. Li, X. Ruan, and H. Bao, "Comprehensive first-principles analysis of phonon thermal conductivity and electron-phonon coupling in different metals," *Physical Review B,* vol. 100, no. 14, p. 144306, 2019.

[36] Y. Wang, Z. Lu, and X. Ruan, "First principles calculation of lattice thermal conductivity of metals considering phonon-phonon and phonon-electron scattering," *Journal of applied Physics,* vol. 119, no. 22, p. 225109, 2016.

[37] A. Minnich, "Exploring the extremes of heat conduction in anisotropic materials," *Nanoscale and Microscale Thermophysical Engineering,* vol. 20, no. 1, pp. 1-21, 2016.

[38] J. P. Feser and D. G. Cahill, "Probing anisotropic heat transport using time-domain thermoreflectance with offset laser spots," *Review of Scientific Instruments*, vol. 83, no. 10, p. 104901, 2012.

[39] A. J. Schmidt, X. Chen, and G. Chen, "Pulse accumulation, radial heat conduction, and anisotropic thermal conductivity in pump-probe transient thermoreflectance," *Review of Scientific Instruments*, vol. 79, no. 11, p. 114902, 2008.

[40] R. Sun and M. A. White, "Ceramics and glasses," in *Thermal Conductivity*: Springer, 2004, pp. 239-254.

[41] Y. S. Ju, "Phonon heat transport in silicon nanostructures," *Applied Physics Letters*, vol. 87, no. 15, p. 153106, 2005.

[42] J. Yang *et al.*, "Thermal conductance imaging of graphene contacts," *Journal of Applied Physics*, vol. 116, no. 2, p. 023515, 2014.

[43] D. A. Dalton, W.-P. Hsieh, G. T. Hohensee, D. G. Cahill, and A. F. Goncharov, "Effect of mass disorder on the lattice thermal conductivity of MgO periclase under pressure," *Scientific reports*, vol. 3, p. 2400, 2013.

[44] S. Ghosh *et al.*, "Dimensional crossover of thermal transport in few-layer graphene," *Nature materials*, vol. 9, no. 7, pp. 555-558, 2010.

[45] P. Kapitza, "The study of heat transfer in helium II," *J. Phys.(USSR)*, vol. 4, no. 1-6, pp. 181-210, 1941.

[46] D. G. Cahill *et al.*, "Nanoscale thermal transport," *Journal of Applied Physics*, vol. 93, no. 2, pp. 793-818, 2003.

[47] C. Monachon, G. Schusteritsch, E. Kaxiras, and L. Weber, "Qualitative link between work of adhesion and thermal conductance of metal/diamond interfaces," *Journal of Applied Physics*, vol. 115, no. 12, p. 123509, 2014.

[48] C. Monachon, L. Weber, and C. Dames, "Thermal Boundary Conductance: A Materials Science Perspective," *Annual Review of Materials Research*, no. 0, 2016.

[49] K. C. Collins, "Experimental investigations of solid-solid thermal interface conductance," Massachusetts Institute of Technology, 2010.

[50] J. H. Taphouse and B. A. Cola, "Nanostructured Thermal Interfaces," *Annual Review of Heat Transfer*, vol. 18.

[51] I. Khalatnikov, "Teploobmen Mezhdu Tverdym Telom I Geliem-Ii," *Zhurnal Eksperimentalnoi I Teoreticheskoi Fiziki*, vol. 22, no. 6, pp. 687-704, 1952.

[52] G. Chen, "Nanoscale energy transport and conversion," 2005.

[53] A. J. Schmidt, K. C. Collins, A. J. Minnich, and G. Chen, "Thermal conductance and phonon transmissivity of metal–graphite interfaces," *Journal of Applied Physics*, vol. 107, no. 10, p. 104907, 2010.

[54] E. T. Swartz and R. O. Pohl, "Thermal boundary resistance," *Reviews of modern physics*, vol. 61, no. 3, p. 605, 1989.

[55] E. Swartz and R. Pohl, "Thermal resistance at interfaces," *Applied Physics Letters*, vol. 51, no. 26, pp. 2200-2202, 1987.

[56] P. Reddy, K. Castelino, and A. Majumdar, "Diffuse mismatch model of thermal boundary conductance using exact phonon dispersion," *Applied Physics Letters*, vol. 87, no. 21, p. 211908, 2005.

[57] M. D. Losego, M. E. Grady, N. R. Sottos, D. G. Cahill, and P. V. Braun, "Effects of chemical bonding on heat transport across interfaces," *Nature materials,* vol. 11, no. 6, pp. 502-506, 2012.

[58] P. E. Hopkins, "Multiple phonon processes contributing to inelastic scattering during thermal boundary conductance at solid interfaces," *Journal of Applied Physics,* vol. 106, no. 1, p. 013528, 2009.

[59] B. C. Gundrum, D. G. Cahill, and R. S. Averback, "Thermal conductance of metal-metal interfaces," *Physical Review B,* vol. 72, no. 24, p. 245426, 2005.

[60] R. Wilson and D. G. Cahill, "Experimental validation of the interfacial form of the Wiedemann-Franz law," *Physical review letters,* vol. 108, no. 25, p. 255901, 2012.

[61] R. Cheaito *et al.*, "Thermal flux limited electron Kapitza conductance in copper-niobium multilayers," *Applied Physics Letters,* vol. 106, no. 9, p. 093114, 2015.

[62] H.-K. Lyeo and D. G. Cahill, "Thermal conductance of interfaces between highly dissimilar materials," *Physical Review B,* vol. 73, no. 14, p. 144301, 2006.

[63] R. M. Costescu, M. A. Wall, and D. G. Cahill, "Thermal conductance of epitaxial interfaces," *Physical Review B,* vol. 67, no. 5, p. 054302, 2003.

[64] J. Duda *et al.*, "Influence of interfacial properties on thermal transport at gold: silicon contacts," *Applied Physics Letters,* vol. 102, no. 8, p. 081902, 2013.

[65] A. Giri *et al.*, "Mechanisms of nonequilibrium electron-phonon coupling and thermal conductance at interfaces," *Journal of Applied Physics,* vol. 117, no. 10, p. 105105, 2015.

[66] M. Jeong *et al.*, "Enhancement of Thermal Conductance at Metal-Dielectric Interfaces Using Subnanometer Metal Adhesion Layers," *Physical Review Applied,* vol. 5, no. 1, p. 014009, 2016.

[67] D. G. Cahill, H. E. Fischer, T. Klitsner, E. Swartz, and R. Pohl, "Thermal conductivity of thin films: measurements and understanding," *Journal of Vacuum Science & Technology A,* vol. 7, no. 3, pp. 1259-1266, 1989.

[68] D. G. Cahill, "Thermal conductivity measurement from 30 to 750 K: the 3ω method," *Review of scientific instruments,* vol. 61, no. 2, pp. 802-808, 1990.

[69] Y. K. Koh *et al.*, "Comparison of the 3w method and time-domain thermoreflectance for measurements of the cross-plane thermal conductivity of epitaxial semiconductors," *Journal of Applied Physics,* vol. 105, no. 5, p. 54303, 2009.

[70] C. Dames, "Measuring the thermal conductivity of thin films: 3 omega and related electrothermal methods," *Annual Review of Heat Transfer,* vol. 16, no. 16, 2013.

[71] J. P. Feser, J. Liu, and D. G. Cahill, "Pump-probe measurements of the thermal conductivity tensor for materials lacking in-plane symmetry," *Review of Scientific Instruments,* vol. 85, no. 10, p. 104903, 2014.

[72] S. M. Oommen and S. Pisana, "Role of the electron-phonon coupling in tuning the thermal boundary conductance at metal-dielectric interfaces by inserting ultrathin metal interlayers," *arXiv preprint arXiv:1910.05893,* 2019.

[73] B. Sun and Y. K. Koh, "Understanding and eliminating artifact signals from diffusely scattered pump beam in measurements of rough samples by time-domain thermoreflectance (TDTR)," *Review of Scientific Instruments,* vol. 87, no. 6, p. 064901, 2016.

[74] A. J. Schmidt, "Pump-probe thermoreflectance," *Annual Review of Heat Transfer,* vol. 16, no. 1, 2013.

[75] A. J. Schmidt, R. Cheaito, and M. Chiesa, "A frequency-domain thermoreflectance method for the characterization of thermal properties," *Review of scientific instruments,* vol. 80, no. 9, p. 094901, 2009.

[76] A. J. Schmidt, R. Cheaito, and M. Chiesa, "Characterization of thin metal films via frequency-domain thermoreflectance," *Journal of Applied Physics,* vol. 107, no. 2, p. 024908, 2010.

[77] J. Liu, J. Zhu, M. Tian, X. Gu, A. Schmidt, and R. Yang, "Simultaneous measurement of thermal conductivity and heat capacity of bulk and thin film materials using frequency-dependent transient thermoreflectance method," *Review of Scientific Instruments,* vol. 84, no. 3, p. 034902, 2013.

[78] J. Yang, C. Maragliano, and A. J. Schmidt, "Thermal property microscopy with frequency domain thermoreflectance," *Review of Scientific Instruments,* vol. 84, no. 10, p. 104904, 2013.

[79] M. Shahzadeh, M. Rahman, O. Hellwig, and S. Pisana, "High-frequency measurements of thermophysical properties of thin films using a modified broad-band frequency domain thermoreflectance approach," *Review of Scientific Instruments,* vol. 89, no. 8, p. 084905, 2018.

[80] M. Rahman, M. Shahzadeh, P. Braeuninger-Weimer, S. Hofmann, O. Hellwig, and S. Pisana, "Measuring the thermal properties of anisotropic materials using Beam-Offset Frequency Domain Thermoreflectance," *Journal of Applied Physics,* vol. 123, no. 24, p. 245110, 2018.

[81] R. Wilson, B. A. Apgar, L. W. Martin, and D. G. Cahill, "Thermoreflectance of metal transducers for optical pump-probe studies of thermal properties," *Optics express,* vol. 20, no. 27, pp. 28829-28838, 2012.

[82] X. Qian, Z. Ding, J. Shin, A. J. Schmidt, and G. Chen, "Accurate measurement of in-plane thermal conductivity of layered materials without metal film transducer using frequency domain thermoreflectance," *Review of Scientific Instruments,* vol. 91, no. 6, p. 064903, 2020.

[83] D. G. Cahill, "Analysis of heat flow in layered structures for time-domain thermoreflectance," *Review of scientific instruments,* vol. 75, no. 12, pp. 5119-5122, 2004.

[84] J. Yang, E. Ziade, and A. J. Schmidt, "Uncertainty analysis of thermoreflectance measurements," *Review of Scientific Instruments,* vol. 87, no. 1, p. 014901, 2016.

[85] E. Dechaumphai *et al.,* "Ultralow thermal conductivity of multilayers with highly dissimilar debye temperatures," *Nano letters,* vol. 14, no. 5, pp. 2448-2455, 2014.

[86] Z. Li *et al.,* "Phonon dominated heat conduction normal to Mo/Si multilayers with period below 10 nm," *Nano letters,* vol. 12, no. 6, pp. 3121-3126, 2012.

[87] D. Rodin and S. K. Yee, "Simultaneous measurement of in-plane and through-plane thermal conductivity using beam-offset frequency domain thermoreflectance," *Review of Scientific Instruments,* vol. 88, no. 1, p. 014902, 2017.

[88] G. Fugallo, A. Cepellotti, L. Paulatto, M. Lazzeri, N. Marzari, and F. Mauri, "Thermal conductivity of graphene and graphite: collective excitations and mean free paths," *Nano letters,* vol. 14, no. 11, pp. 6109-6114, 2014.

[89] J. Liu, G.-M. Choi, and D. G. Cahill, "Measurement of the anisotropic thermal conductivity of molybdenum disulfide by the time-resolved magneto-optic Kerr effect," *Journal of Applied Physics,* vol. 116, no. 23, p. 233107, 2014.

[90] M. Rahman, M. Shahzadeh, and S. Pisana, "Simultaneous measurement of anisotropic thermal conductivity and thermal boundary conductance of 2-dimensional materials," *Journal of Applied Physics,* vol. 126, no. 20, p. 205103, 2019.

[91] D. Saha *et al.*, "Enhancing Thermal Interface Conductance to Graphene Using Ni–Pd Alloy Contacts," *ACS Applied Materials & Interfaces,* vol. 12, no. 30, pp. 34317-34322, 2020.

[92] P. A. V. Guzman *et al.*, "Cross plane thermal conductance of graphene-metal interfaces," in *Fourteenth Intersociety Conference on Thermal and Thermomechanical Phenomena in Electronic Systems (ITherm),* 2014, pp. 1385-1389: IEEE.

[93] J. P. Freedman, J. H. Leach, E. A. Preble, Z. Sitar, R. F. Davis, and J. A. Malen, "Universal phonon mean free path spectra in crystalline semiconductors at high temperature," *Scientific reports,* vol. 3, 2013.

[94] K. Regner, A. J. McGaughey, and J. A. Malen, "Analytical interpretation of nondiffusive phonon transport in thermoreflectance thermal conductivity measurements," *Physical Review B,* vol. 90, no. 6, p. 064302, 2014.

[95] P. E. Hopkins, J. R. Serrano, L. M. Phinney, S. P. Kearney, T. W. Grasser, and C. T. Harris, "Criteria for cross-plane dominated thermal transport in multilayer thin film systems during modulated laser heating," *Journal of Heat Transfer,* vol. 132, no. 8, p. 081302, 2010.

[96] C. Zhang *et al.*, "Heat conduction across metal and nonmetal interface containing imbedded graphene layers," *Carbon,* vol. 64, pp. 61-66, 2013.

[97] J. A. Malen, K. Baheti, T. Tong, Y. Zhao, J. A. Hudgings, and A. Majumdar, "Optical measurement of thermal conductivity using fiber aligned frequency domain thermoreflectance," *Journal of Heat Transfer,* vol. 133, no. 8, p. 081601, 2011.

[98] A. J. Minnich *et al.*, "Thermal conductivity spectroscopy technique to measure phonon mean free paths," *Physical review letters,* vol. 107, no. 9, p. 095901, 2011.

[99] A. Giri, S. H. Wee, S. Jain, O. Hellwig, and P. E. Hopkins, "Influence of chemical ordering on the thermal conductivity and electronic relaxation in FePt thin films in heat assisted magnetic recording applications," *Scientific reports,* vol. 6, p. 32077, 2016.

[100] R. Wilson and D. G. Cahill, "Anisotropic failure of Fourier theory in time-domain thermoreflectance experiments," *Nature communications,* vol. 5, p. 5075, 2014.

[101] C. Hua, X. Chen, N. K. Ravichandran, and A. J. Minnich, "Experimental metrology to obtain thermal phonon transmission coefficients at solid interfaces," *Physical Review B,* vol. 95, no. 20, p. 205423, 2017.

[102] R. Zeller and R. Pohl, "Thermal conductivity and specific heat of noncrystalline solids," *Physical Review B,* vol. 4, no. 6, p. 2029, 1971.

[103] C. Hua and A. J. Minnich, "Heat dissipation in the quasiballistic regime studied using the Boltzmann equation in the spatial frequency domain," *Physical Review B,* vol. 97, no. 1, p. 014307, 2018.

[104] R. Wilson and D. G. Cahill, "Limits to Fourier theory in high thermal conductivity single crystals," *Applied Physics Letters,* vol. 107, no. 20, p. 203112, 2015.

[105] P. Giannozzi *et al.*, "QUANTUM ESPRESSO: a modular and open-source software project for quantum simulations of materials," *Journal of physics: Condensed matter,* vol. 21, no. 39, p. 395502, 2009.

[106] A. Jain *et al.*, "Commentary: The Materials Project: A materials genome approach to accelerating materials innovation," *Apl Materials,* vol. 1, no. 1, p. 011002, 2013.

[107] A. Togo, F. Oba, and I. Tanaka, "First-principles calculations of the ferroelastic transition between rutile-type and CaCl 2-type SiO 2 at high pressures," *Physical Review B,* vol. 78, no. 13, p. 134106, 2008.

[108] Available: https://bitbucket.org/sousaw/thirdorder.git

[109] J. Carrete *et al.*, "almaBTE: A solver of the space–time dependent Boltzmann transport equation for phonons in structured materials," *Computer Physics Communications,* vol. 220, pp. 351-362, 2017.

[110] K. Esfarjani, G. Chen, and H. T. Stokes, "Heat transport in silicon from first-principles calculations," *Physical Review B,* vol. 84, no. 8, p. 085204, 2011.

[111] G. T. Hohensee *et al.*, "Pump-probe thermoreflectance measurements of critical interfaces for thermal management of HAMR heads," *MRS Advances,* vol. 2, no. 58-59, pp. 3627-3636, 2017.

[112] K.-F. Huang, D.-S. Wang, H.-H. Lin, and C.-H. Lai, "Engineering spin-orbit torque in Co/Pt multilayers with perpendicular magnetic anisotropy," *Applied Physics Letters,* vol. 107, no. 23, p. 232407, 2015.

[113] G.-M. Choi, C.-H. Moon, B.-C. Min, K.-J. Lee, and D. G. Cahill, "Thermal spin-transfer torque driven by the spin-dependent Seebeck effect in metallic spin-valves," *Nature physics,* vol. 11, no. 7, pp. 576-581, 2015.

[114] J. Kimling, R. Wilson, K. Rott, J. Kimling, G. Reiss, and D. G. Cahill, "Spin-dependent thermal transport perpendicular to the planes of Co/Cu multilayers," *Physical Review B,* vol. 91, no. 14, p. 144405, 2015.

[115] J. Kimling and D. G. Cahill, "Spin diffusion induced by pulsed-laser heating and the role of spin heat accumulation," *Physical Review B,* vol. 95, no. 1, p. 014402, 2017.

[116] Q. Zhou, P. Huang, M. Liu, F. Wang, K. Xu, and T. Lu, "Grain and interface boundaries governed strengthening mechanisms in metallic multilayers," *Journal of Alloys and Compounds,* vol. 698, pp. 906-912, 2017.

[117] J. Snel *et al.*, "Deformation mechanism map of Cu/Nb nanoscale metallic multilayers as a function of temperature and layer thickness," *Jom,* vol. 69, no. 11, pp. 2214-2226, 2017.

[118] S. Zheng *et al.*, "High-strength and thermally stable bulk nanolayered composites due to twin-induced interfaces," *Nature communications,* vol. 4, no. 1, pp. 1-8, 2013.

[119] Y.-C. Lau *et al.*, "Giant perpendicular magnetic anisotropy in Ir/Co/Pt multilayers," *Physical Review Materials,* vol. 3, no. 10, p. 104419, 2019.

[120] H. Jang, J. Kimling, and D. G. Cahill, "Nonequilibrium heat transport in Pt and Ru probed by an ultrathin Co thermometer," *Physical Review B,* vol. 101, no. 6, p. 064304, 2020.

[121] G.-M. Choi, R. Wilson, and D. G. Cahill, "Indirect heating of Pt by short-pulse laser irradiation of Au in a nanoscale Pt/Au bilayer," *Physical Review B,* vol. 89, no. 6, p. 064307, 2014.

[122] !!! INVALID CITATION !!! [54, 59-61].

[123] D. Gall, "Electron mean free path in elemental metals," *Journal of Applied Physics,* vol. 119, no. 8, p. 085101, 2016.

[124] J. A. Johnson *et al.*, "Direct measurement of room-temperature nondiffusive thermal transport over micron distances in a silicon membrane," *Physical review letters,* vol. 110, no. 2, p. 025901, 2013.

[125] M. Simkin and G. Mahan, "Minimum thermal conductivity of superlattices," *Physical Review Letters,* vol. 84, no. 5, p. 927, 2000.

[126] B. A. Gurney, V. S. Speriosu, J.-P. Nozieres, H. Lefakis, D. R. Wilhoit, and O. U. Need, "Direct measurement of spin-dependent conduction-electron mean free paths in ferromagnetic metals," *Physical review letters,* vol. 71, no. 24, p. 4023, 1993.

[127] B. Böhm *et al.*, "Antiferromagnetic domain wall control via surface spin flop in fully tunable synthetic antiferromagnets with perpendicular magnetic anisotropy," *Physical Review B,* vol. 100, no. 14, p. 140411, 2019.

[128] J. Kimling, A. Philippi-Kobs, J. Jacobsohn, H. P. Oepen, and D. G. Cahill, "Thermal conductance of interfaces with amorphous SiO 2 measured by time-resolved magneto-optic Kerr-effect thermometry," *Physical Review B,* vol. 95, no. 18, p. 184305, 2017.

[129] E. A. Scott *et al.*, "Thermal resistance and heat capacity in hafnium zirconium oxide (Hf1–xZrxO2) dielectrics and ferroelectric thin films," *Applied Physics Letters,* vol. 113, no. 19, p. 192901, 2018.

[130] S. Mei and I. Knezevic, "Thermal conductivity of III-V semiconductor superlattices," *Journal of Applied Physics,* vol. 118, no. 17, p. 175101, 2015.

[131] B. Yang and G. Chen, "Partially coherent phonon heat conduction in superlattices," *Physical Review B,* vol. 67, no. 19, p. 195311, 2003.

[132] A. Sharma, J. Romero, N. Theodoropoulou, R. Loloee, W. Pratt Jr, and J. Bass, "Specific resistance and scattering asymmetry of Py/Pd, Fe/V, Fe/Nb, and Co/Pt interfaces," *Journal of Applied Physics,* vol. 102, no. 11, p. 113916, 2007.

[133] D. Dye, J. B. Ketterson, and G. Crabtree, "The Fermi surface of platinum," *Journal of Low Temperature Physics,* vol. 30, no. 5-6, pp. 813-838, 1978.

[134] D. Petrovykh *et al.*, "Spin-dependent band structure, Fermi surface, and carrier lifetime of permalloy," *Applied Physics Letters,* vol. 73, no. 23, pp. 3459-3461, 1998.

[135] R. Acharyya *et al.*, "Specific resistance of Pd/Ir interfaces," *Applied Physics Letters,* vol. 94, no. 2, p. 022112, 2009.

[136] L. Zeng *et al.*, "Measuring phonon mean free path distributions by probing quasiballistic phonon transport in grating nanostructures," *Scientific reports,* vol. 5, p. 17131, 2015.

[137] J. Cuffe *et al.*, "Reconstructing phonon mean-free-path contributions to thermal conductivity using nanoscale membranes," *Physical Review B,* vol. 91, no. 24, p. 245423, 2015.

[138] N. Peimyoo, J. Shang, W. Yang, Y. Wang, C. Cong, and T. Yu, "Thermal conductivity determination of suspended mono-and bilayer WS 2 by Raman spectroscopy," *Nano Research,* vol. 8, no. 4, pp. 1210-1221, 2015.

[139] R. Yan *et al.*, "Thermal conductivity of monolayer molybdenum disulfide obtained from temperature-dependent Raman spectroscopy," *ACS nano,* vol. 8, no. 1, pp. 986-993, 2014.

[140] X. Zhang *et al.*, "Measurement of lateral and interfacial thermal conductivity of single-and bilayer MoS2 and MoSe2 using refined optothermal Raman technique," *ACS applied materials & interfaces,* vol. 7, no. 46, pp. 25923-25929, 2015.

[141] H. Zhou *et al.*, "High thermal conductivity of suspended few-layer hexagonal boron nitride sheets," *Nano Research,* vol. 7, no. 8, pp. 1232-1240, 2014.

[142] A. A. Balandin *et al.*, "Superior thermal conductivity of single-layer graphene," *Nano letters,* vol. 8, no. 3, pp. 902-907, 2008.

[143] H. Malekpour and A. A. Balandin, "Raman-based technique for measuring thermal conductivity of graphene and related materials," *Journal of Raman Spectroscopy,* vol. 49, no. 1, pp. 106-120, 2018.

[144] G. Zhu *et al.*, "Tuning thermal conductivity in molybdenum disulfide by electrochemical intercalation," *Nature communications,* vol. 7, no. 1, pp. 1-9, 2016.

[145] S. Manzeli, D. Ovchinnikov, D. Pasquier, O. V. Yazyev, and A. Kis, "2D transition metal dichalcogenides," *Nature Reviews Materials,* vol. 2, no. 8, p. 17033, 2017.

[146] D. L. Duong, S. J. Yun, and Y. H. Lee, "van der Waals layered materials: opportunities and challenges," *ACS nano,* vol. 11, no. 12, pp. 11803-11830, 2017.

[147] W. Choi, N. Choudhary, G. H. Han, J. Park, D. Akinwande, and Y. H. Lee, "Recent development of two-dimensional transition metal dichalcogenides and their applications," *Materials Today,* vol. 20, no. 3, pp. 116-130, 2017.

[148] S. Das, J. A. Robinson, M. Dubey, H. Terrones, and M. Terrones, "Beyond graphene: progress in novel two-dimensional materials and van der Waals solids," *Annual Review of Materials Research,* vol. 45, pp. 1-27, 2015.

[149] A. Pisoni *et al.*, "Anisotropic transport properties of tungsten disulfide," *Scripta Materialia,* vol. 114, pp. 48-50, 2016.

[150] D. O. Lindroth and P. Erhart, "Thermal transport in van der Waals solids from first-principles calculations," *Physical Review B,* vol. 94, no. 11, p. 115205, 2016.

[151] P. Jiang, X. Qian, X. Gu, and R. Yang, "Probing Anisotropic Thermal Conductivity of Transition Metal Dichalcogenides MX2 (M= Mo, W and X= S, Se) using Time-Domain Thermoreflectance," *Advanced Materials,* vol. 29, no. 36, p. 1701068, 2017.

[152] R. Guo, Y.-D. Jho, and A. J. Minnich, "Coherent control of thermal phonon transport in van der Waals superlattices," *Nanoscale,* vol. 10, no. 30, pp. 14432-14440, 2018.

[153] M. S. Rahman, M. Shahzadeh, M. Rahman, S. Pisana, and G. Grau, "High-speed contactless sintering characterization for printed electronics by frequency-domain thermoreflectance," *Flexible and Printed Electronics,* vol. 5, no. 3, p. 035006, 2020.

[154] J. Ravichandran *et al.*, "Crossover from incoherent to coherent phonon scattering in epitaxial oxide superlattices," *Nature materials,* vol. 13, no. 2, pp. 168-172, 2014.

[155] F. Wang *et al.*, "2D library beyond graphene and transition metal dichalcogenides: a focus on photodetection," *Chemical Society Reviews,* vol. 47, no. 16, pp. 6296-6341, 2018.

[156] K. Novoselov, o. A. Mishchenko, o. A. Carvalho, and A. C. Neto, "2D materials and van der Waals heterostructures," *Science,* vol. 353, no. 6298, 2016.